Liquid Crystals Towards Terahertz: Characterisation and Tunable Waveguide Phase Shifters for Millimetre-Wave and Terahertz Beamsteering Antennas

Vom Fachbereich Elektrotechnik und Informationstechnik
der Technischen Universität Darmstadt zur Erlangung des
akademischen Grades eines Doktor-Ingenieurs
(Dr.-Ing.) genehmigte

Dissertation

von

Dipl.-Ing.
Christian Joachim Michael Weickhmann

geboren am 14. Januar 1985 in Bad Homburg v. d. H.

Referent:	Prof. Dr.-Ing. Rolf Jakoby
Korreferent:	Prof. Dr.-Ing. Arne Jacob
Tag der Einreichung:	01.11.2016
Tag der mündlichen Prüfung:	14.03.2017

D17
Darmstädter Dissertation
2017

Erklärungen gemäß §§ 8 und 9 der Promotionsordnung der Technischen Universität Darmstadt (PromO)

Erklärung gemäß §8 Abs. 1 PromO

Hiermit erkläre ich, dass ich bisher keinen Promotionsversuch unternommen habe.

Erklärung gemäß §9 Abs. 1 PromO

Hiermit erkläre ich, dass ich die vorliegende Dissertationsschrift selbstständig und ausschließlich unter Verwendung der im Quellenverzeichnis (Bibliography) angegebenen Hilfsmitteln angefertigt habe.

Erklärung gemäß §9 Abs. 2 PromO

Die im Rahmen dieser Dissertation erstellten Prüfungsarbeiten sind, sofern sie in die Arbeit Eingang gefunden haben, als solche gekennzeichnet und im Quellenverzeichnis (Bibliography) aufgeführt.

Darmstadt, den _____ _____

Abstract

This thesis treats methods of characterisation of the anisotropic complex permittivity tensor of Liquid Crystals (LCs) from the microwave range up to the terahertz range, and the use thereof in a tunable waveguide phase shifter for a Ka band phased array antenna for space application.

An overview of the relevant properties of LCs is presented and relevant concepts are introduced. The characterisation is carried out using two methods: a resonant cavity technique at 30 and 60 GHz, and transmission measurements at frequencies from 100 GHz to 8 THz.

A numerical method based on the Finite Element Method (FEM) is developed in order to extract permittivity and loss angle from the measurement of resonance frequencies of a given cavity containing a small amount of LC in a quartz tube. The method can be used on any geometry exhibiting cylindrical symmetry and extends earlier approaches significantly. The software library used to this end is FEniCS, which provides high performance and a great degree of flexibility. Separation of the anisotropic properties is obtained by magnetically biasing the setup. The data obtained for commercial and non-commercial microwave-optimised LCs provided by Merck KGaA, Darmstadt (Merck) are presented.

Transmissivity data is presented for several LC mixtures obtained by Time-Domain Spectroscopy (TDS) and Fourier Transform Interferometry (FTIR) comparing material loss angles over a large frequency range. The measurement method is described and the obtained data is shown.

This thesis furthermore presents the design, implementation and verification of a waveguide phase shifter using LC as functional material and light-weight construction techniques, namely the Light-weight Intersatellite Antenna – Electronical Steering (LISA_{ES}). The phase shifter developed within the frame of this thesis functions in the Ka band, covers two bands at 23 GHz and at 27 GHz. The biasing of this otherwise fully passive device is implemented by embedding an all-electric biasing network into the waveguide structure. The fully integrated phase shifter exhibits a maximum differential phase shift of 540°, a figure of merit of up to 120 °/dB, and an overall weight of less than 19 g per device. Its transient performance is assessed and switching times of less than 45 s in the fast direction and 210 s in the slow direction are verified. It can be shown that all performance criteria derived from the project's specifications can be met using LC technology. Furthermore, it is the first time, such a high figure of merit is reported for a highly integrated, light-weight microwave phase shifter.

In conclusion, an outlook on future technologies based on LC waveguide phase shifters at mm-wave frequencies for extremely large datarates is discussed. First experiments show the potential of LC technology in waveguide topology at 250 GHz, where the dimensions are challenging for fabrication but favourable for switching speed.

Zusammenfassung

Die vorliegende Arbeit behandelt Methoden zur Charakterisierung des anisotropen, komplexen Permittivitätstensors von Flüssigkristall (engl. *liquid crystal*, LC) vom Mikrowellen- bis in den Terahertzbereich und die Verwendung von LCs in steuerbaren Hohlleiterphasenschiebern für eine Ka-Band Gruppenantenne zum Raumfahrteinsatz.

Es wird ein Überblick über die relevanten Eigenschaften von LCs und ihre wesentlichen Steuerkonzepte gegeben. Die Charakterisierung wird mithilfe von zwei Methoden durchgeführt: der Resonatormethode bei 30 und 60 GHz sowie der Transmissionsmethode bei Frequenzen zwischen 100 GHz und 8 THz.

Um Permittivität und Verlustwinkel aus den Messungen kleiner LC-Volumina in Quarz-Röhrchen in einer Resonatorkavität zu extrahieren, wird eine numerische Methode basierend auf der Finiten Elemente Methode (FEM) entwickelt. Diese funktioniert mit beliebigen zylindersymmetrischen Geometrien und erweitert vorherige Ansätze maßgeblich. Die dafür genutzte Bibliothek ist FEniCS, welche hohe Leistung und einen hohen Grad an Freiheit gewährt. Die Zuordnung der anisotropen Materialeigenschaften wird durch magnetische Ausrichtung der Probe gewährleistet. Es werden Daten für kommerzielle wie nicht-kommerzielle LC-Mischungen präsentiert, die von Merck KGaA, Darmstadt bereitgestellt wurden. Mit Hilfe der Zeitbereichsspektroskopie (engl. *time-domain spectroscopy*, TDS) sowie der Fouriertransformationsinterferometrie (engl. *Fourier transform interferometry*, FTIR) werden LC-Mischungen vermessen und ihre Verlustwinkel über einen großen Frequenzbereich hinweg verglichen.

Weiterhin werden der Entwurf, die Umsetzung und die Verifikation eines LC-Hohlleiterphasenschiebers in Leichtbauweise im Rahmen von $\mathrm{LISA}_{\mathrm{ES}}$ (Leichte Inter-Satelliten Antenne, Elektronische Steuerung) dargestellt. Der hier entwickelte Phasenschieber arbeitet im Ka-Band und deckt insbesondere die Bänder um 23 GHz und 27 GHz ab. Die Ausrichtung des LC wird in dem sonst komplett passiven Bauteil durch eine komplett elektrische Elektrodenanordnung mit integriertem Spannungsteiler innerhalb des Hohlleiters realisiert. Der voll integrierte Phasenschieber weist einen maximalen differentiellen Phasenhub von 540°, eine Güte (FoM) von bis zu 120 °/dB und ein Gesamtgewicht von nur 19 g auf. Seine Schaltzeiten liegen bei 45 s in der schnellen Richtung und 210 s in der langsamen Richtung. Es wird gezeigt, dass alle Performance-Kriterien, die im Projekt definiert wurden, mit Hilfe der hier vorgestellten LC-Technologie erfüllt werden können. Darüber hinaus wird zum ersten Mal eine Phasenschiebergüte dieser Größe bei einem hochintegrierten Phasenschieber in Leichtbauweise präsentiert.

Schließlich wird ein Ausblick auf künftige Technologien auf Basis von LC-Hohlleiterphasenschiebern im mm-Wellenbereich für extrem hohe Datenraten gegeben. Erste durchgeführte Experimente zeigen das Potential dieser Technik im Bereich von 250 GHz, in dem die Abmessungen zwar eine Herausforderung für die Fertigung darstellen, jedoch im Bezug auf Schaltzeiten große Chancen bieten.

List of Symbols

χ	Susceptibility, the relative amount to which a medium is polarised by an external electric field
$\vec{D}$	Electric displacement field
$\vec{E}$	Electric field
ε	Permittivity, the quantity relating electric field and electric displacement field
$\varepsilon_{r,\parallel}$	Parallel permittivity, component of the canonic relative permittivity tensor
$\varepsilon_{r,\perp}$	Perpendicular permittivity, component of the canonic relative permittivity tensor
$\tilde{\varepsilon}$	Canonic Permittivity, the result of the eigendecomposition of an anisotropic permittivity tensor
η	Material figure of merit, measuring the the ratio of material tunability over maximum loss angle, $\eta = \tau / \max \tan \delta$
$\mathcal{F}$	Gibbs free energy, thermodynamic potential ("useful work") at constant pressure and temperature
f	Gibbs free energy density, thermodynamic potential ("useful work") per unit volume at constant pressure and temperature
$\mathcal{F}_{\text{bend}}$	Gibbs free potential energy available in bend deformations of the director field
$\mathcal{F}_{\text{el}}$	Gibbs free potential energy available due to the presence of an electric field
$\mathcal{F}_{\text{mag}}$	Gibbs free potential energy available due to the presence of a magnetic field
$\mathcal{F}_{\text{splay}}$	Gibbs free potential energy available in splay deformations of the director field
$\mathcal{F}_{\text{twist}}$	Gibbs free potential energy available in twist deformations of the director field
FoM	Figure of Merit, a phase shifter's performance measured by the ratio of maximum achievable phase shift $\Delta\Phi_{\text{max}}$ over maximum insertion loss IL_{max}
γ	Dynamic viscosity, relation between the dynamic shear stress and the lateral velocity change
h_{cav}	Cavity height
$\mathbf{I}$	Identity matrix
IL	Insertion Loss, the magnitude of transmission loss $\lvert S_{12} \rvert, \lvert S_{21} \rvert$ through a two-port block in dB given in positive numbers

$\mathfrak{I}$	Imaginary part of a complex number
μ	Permeability, the quantity relating magnetic fields $\vec{B}$ and $\vec{H}$
$\vec{n}$	Normal vector with respect to a surface element
$\vec{n}_{\mathrm{LC}}$	Director, a vector of unit length pointing in the direction of local orientation (quasi optical axis) of an LC bulk
$\vec{P}$	The electrical polarisation field induced by an external electric field
Q	Quality factor
r_{cav}	Cavity radius
$\mathfrak{R}$	Real part of a complex number
r_{ext}	Cavity filling hole radius
ρ	Electric charge density in $\mathrm{C/m^3}$
$r_{\mathrm{q,inner}}$	Quartz tube inner radius
S	Order parametre, a statistical measure for order in LC
σ	Electric conductivity in S/m, usually scalar – may be a tensor. Inverse of resistivity $1/\varrho$
$\tan\delta_{\parallel}$	Parallel loss tangent, along the optical axis
$\tan\delta_{\perp}$	Perpendicular loss tangent, orthogonal to the optical axis
τ	Material tunablity, measuring the relative permittivity difference between along and orthogonal to the optical axis, i. e. the material's birefringence
T_c	Clearing point, the temperature at which transition from a liquid crystalline meso-phase to isotropic phase takes place
T_m	Melting point, the temperature at which the material melts, i. e. transition from a crystalline solid into liquid crystalline meso-phase
τ_{90}^{10}	Off-on time, from 90 % to 10 % of the maximum absolute phase shift of a phase shifter device
τ_{10}^{90}	On-off time, from 10 % to 90 % of the maximum absolute phase shift of a phase shifter device
τ_{sw}	Asymptotic switching time, from 0 % to 100 % of the maximum absolute phase shift of a phase shifter device

Contents

1. Motivation

The field of wireless communications is driven by the ever growing demand for high data rate, more subscribers; in other words: bandwidth. But recently ever more so by coverage and the temporal persistence of data links for example for real-time communication.

While, historically, satellite links have been either point-to-point or broadcast links (Figures 1.1a and 1.1b), recent applications increasingly require bidirectional use of satellite links (Figure 1.1c). In terrestrial applications this is the standard case and can be implemented using static, low-gain antennas, due to the comparatively short distances. Space diversity is realised because base stations are scattered over the surface of the earth. In satellite communications this is different. Satellites are expensive and although their number is tremendous and increasing, satellite ground services as well as inter-satellite links are point-to-point or point-to-multipoint links and will remain as such for a long time.

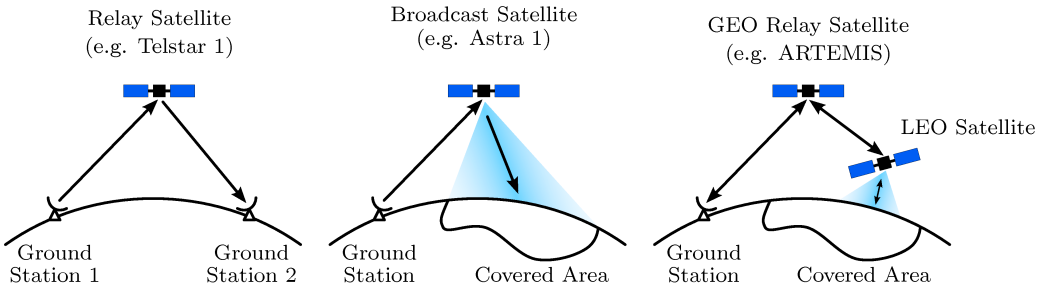

(a) Point-to-point (b) Broadcast (c) Bidirectional point-to-point

Figure 1.1.: Evolution of space links

In parallel, the growing number of orbiting satellites (in or out of service) has created demand for in-orbit repair or disposal systems [YDN06; Rek+07]. The dynamics of such systems are investigated at Technische Universität München (TUM). In conjunction with longstanding investigations by Deutsches Zentrum für Luft- und Raumfahrt, German Aerospace Center (DLR) the idea of a ground-operated in-orbit servicing module is investigated [Lan+06; Sto+09; Hir+05]. In contrast to classical service and programming, which is autonomous or simulated on ground and where only a set of control commands are sent to the space craft, this new kind of mission requires high bandwidth because a video signal has to be transmitted to the operator, who creates the control and steering commands in real time [Rei+10].

The obvious consequence is high bandwidth, the less obvious consequence is the need to create a persistent link. In a point-to-point configuration, this is only possible when the module is in sight of a ground station. While this is often the case above land, this is hard to realise over the poles, or e.g. the Pacific Ocean. Geostationary relay satellites offer a solution to this problem: located 36 000 km above ground, only a few would be sufficient to be visible from all possible low earth orbit (LEO) locations at any time as well as from at least one ground station [Rei+10]. Only as little as three handovers would be necessary in order to keep up a persistent connection.

The downside is that both the LEO and the geostationary orbit (GEO) satellite need to steer their antenna to establish the link. Mechanical steering poses one large issue: the transmission of angular momentum between antenna and hosting craft induces a movement of the space craft whenever the antenna is moved. Therefore, each movement has to be countered by a craft manœuvre to keep the craft from gathering momentum and ultimately from spinning.

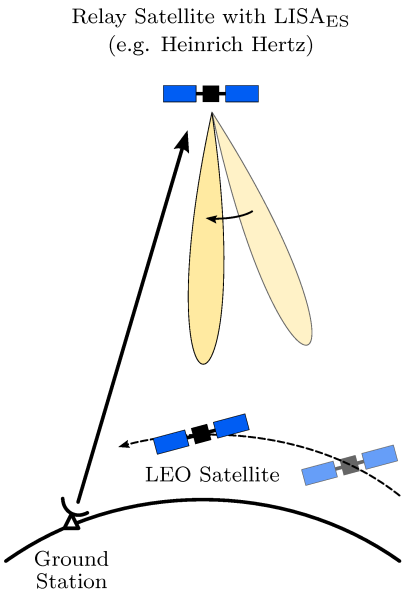

Figure 1.2.: The link schema proposed in LISA$_{ES}$

In the LEO case, this is often accepted due to the low orbit, the consequently lower cost of placing the craft in the orbit, and the need for manœuvres for debris avoidance and to compensate for atmospheric drag. However, moveable parts are always avoided if alternative technologies are available. While for LEO missions it would therefore be *beneficial* to use non-mechanical steering, for GEO satellites it is almost *inevitable*: the cost of placing the craft in orbit is significantly higher, great effort is undertaken to replace chemical propulsion by electric propulsion in order to reduce weight and disposal of a tumbling GEO satellite is much harder than in LEO scenarios.

Driven by these considerations, the Light-weight Intersatellite Antenna – Electronical Steering (LISA$_{ES}$) project tries to provide a low-loss, low-weight, and high-gain antenna for GEO-LEO links (Figure 1.2). The functional material of choice is Liquid Crystal (LC), for it offers proven low dissipation and high tunability [Wei+13a].

It should be noted that similar considerations hold for the case of on-the-move satellite tracking by ground terminals. The main difference here would be power handling. A satellite antenna must manage hundreds of Watts while a ground terminal should not exceed tens of Watts [RD15; Vat+99]. Furthermore the geometrical requirements differ greatly. Therefore, the topologies will inevitably be different with a preference for low-loss hollow waveguide structures in space and compact, flat planar topologies in the ground segment.

In terrestrial systems, the situation is slightly different: Persistence of links is widely established. But with an increasing number of devices, an increasing number of access points using far more frequency bands and in general higher frequencies, aspects like space diversity, selectivity, and high-gain links grow important.

One example is a 5$^{\text{th}}$ generation mobile networks (5G) or Wireless LAN (WiFi) access point operating in the 60 GHz band [Guo+07; VFC13]. Complex environments like buildings or adjacent rooms require a large number of access points. Beam forming eases the constraints on frequency-reuse in such networks. Two physically close WiFi access points could serve the same frequency band, in a library for example, with one covering one half and the other covering the other half of the room (Figure 1.3a). It is impossible to change each access point with respect to its installed location. On the other hand, it would be possible to reshape the illuminated area using adaptive antenna technologies (Figure 1.3b). This is currently done using digital beamforming and MIMO approaches. Low-loss tunable antenna arrays could supplement these techniques and potentially improve the service quality.

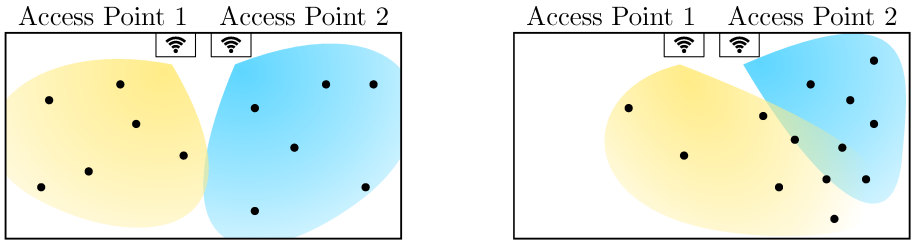

(a) Even subscriber distribution

(b) Odd subscriber distribution

Figure 1.3.: Balancing scenario for potential future WiFi access points in a dynamic in-door pico-cell setup

There are several technologies to achieve this functionality in the higher frequency ranges, but LC in particular provides the crucial characteristics: low dissipation, low power requirements, and established planar technologies.

This leads to the investigation of the dielectric properties of LC towards higher frequencies, even exceeding the 100 GHz range. Although not concludingly treated in this thesis, a phased array antenna at 250 GHz should show interesting properties and bring up new fields where passive LC technology is advantageous compared to other technologies like semiconductors or MEMS. This lower THz range is interesting for short-range data links, close-range radar ranging and sensing. It therefore provides the motivation to investigate LCs at THz frequencies and to look at waveguide technologies exploiting their unique properties.

Outline of the Thesis Chapter 2 focusses on the fundamentals of LCs from an application perspective. All properties necessary for the understanding and design of LC microwave and mm-wave devices are introduced.

Chapter 3 lays out two characterisation methods in two frequency bands. The highly accurate resonant cavity method including a numerical parameter extraction method (Section 3.2) will be used for measurements at 30 GHz. Furthermore, measurements at 60 GHz will be discussed (Section 3.3). The less accurate wideband transmission method, on the other hand (Section 3.4), will be used for measurements in the terahertz

range covering almost two decades from 100 GHz to 8 THz.

In Chapter 4, the application of LC in an inter-satellite link is discussed. The LISA_{ES} phase shifter design is presented and discussed based on device measurement results obtained from prototypes. Fabrication as well as performance is discussed in context with the application. The phase shifters are benchmarked not only in the frequency domain but also in terms of their transient performance as electrically steerable phase shifters.

Chapter 5 provides a conclusive view on the results of this work as well as an outlook towards future antenna systems for high-throughput transcievers studied by example at 250 GHz.

At last, many of the mathematical analyses have been placed in the Mathematical Appendix A as they are in essence not new and serve as a comprehensive mathematical toolbox for the technical methods in this thesis.

2. Fundamentals of Liquid Crystals for Microwave to Terahertz Application

Today, LC are available as high performance materials that are widely used in the display industry eversince the beginning of the 21st century. While other solutions are becoming more and more relevant to display industry, the unique properties still make LCs a material second to none for many optical or quasi-optical applications – such as the use as tunable dielectric in Radio Frequency (RF) devices. The definition of an RF device in this work stretches over a large part of the microwave range up into the terahertz range and will be losely defined as the range from 10 GHz to 10 THz. The uniqueness of modern LC mixtures lies in their almost dispersion-free properties over the whole aforementioned range.

The physics of LCs is complex and was only well described almost a century after botanist and chemist Friedrich Reinitzer's first description of an anomaly at the melting point of Cholesterol derivates [Rei88]. To understand the physics of the devices developed and described within the frame of this thesis, a microscopic understanding of the material systems is not important. However, the macroscopic behaviour based on statistical physics and works from various scientists (most notably perhaps Pierre-Gilles deGennes who recieved a Nobel Prize in Physics for his work on soft matter in 1991 and in particular LC [dP95]) will be briefly reviewed in this chapter, enabling the reader to understand key features of the presented devices.

2.1. Definition of a Liquid Crystal

The term Liquid Crystal describes its nature to be materials or mixtures thereof that exhibit at least one meso-phase[1] between crystalline and liquid. It combines certain properties of both classical phases, hence the name. Quasi-crystalline properties are:

1. Long-range order, in that for each meso-phase the compounds align in a specific way that exhibits certain symmetries.

2. Dielectric (and magnetic) anisotropy, in that – as a consequence of the long range order – birefringence can be observed at various frequencies.

These properties will be described in the following sections in order to establish the framework for modeling LC devices.

[1] Meso-phase (from greek *μέσος*, "middle"), as opposed to a classical phase.

2.2. Anisotropic Properties and Electromagnetic Field Interaction

General The interaction of any polarisable, i.e. dielectric material can be described using its polarisation $\vec{P}$

$$\vec{P} = \chi \varepsilon_0 \vec{E} \tag{2.1}$$

The susceptibility χ can generally be a tensor, i.e. an electric field $\vec{E}$ in only one direction may polarise the medium in other directions. The resulting electric displacement $\vec{D}$ is the sum of polarisation field and electric field

$$\vec{D} = \vec{P} + \vec{E} = (\chi + 1)\, \varepsilon_0 \vec{E} = \varepsilon \vec{E}. \tag{2.2}$$

The relating quantity is called the permittivity ε, which can be expressed as the product of the permittivity in vacuum ε_0 and a relative permittivity ε_r. Both the relative permittivity and in consequence the permittivity can be a tensor.

When an anisotropic material is considered, the relative permittivity takes the general form

$$\varepsilon_r = \begin{pmatrix} \varepsilon_{r,11} & \varepsilon_{r,12} & \varepsilon_{r,13} \\ \varepsilon_{r,21} & \varepsilon_{r,22} & \varepsilon_{r,23} \\ \varepsilon_{r,31} & \varepsilon_{r,32} & \varepsilon_{r,33} \end{pmatrix}. \tag{2.3}$$

This second order tensor posesses up to three eigenvalues and eigenvectors and can be rewritten in an eigendecomposition of the form

$$\varepsilon_r = R \cdot \tilde{\varepsilon}_r \cdot R^{-1}, \tag{2.4}$$

where R is a square matrix of eigenvectors, R^{-1} its inverse and the canonic permittivity has the form

$$\tilde{\varepsilon}_r = \begin{pmatrix} \varepsilon_{r,1} & 0 & 0 \\ 0 & \varepsilon_{r,2} & 0 \\ 0 & 0 & \varepsilon_{r,3} \end{pmatrix}, \tag{2.5}$$

with $\varepsilon_{r,\{1,2,3\}}$ being the respective eigenvalues. The eigenvectors correspond to the dielectric or optical axes of the anisotropic medium. If two eigenvalues of the tensor have the same value, there is a degree of freedom around the single eigenvector, i.e. the only remaining optical axis. If all eigenvalues are equal the material is isotropic and the tensor collapses to $\varepsilon_r \cdot \mathbf{I}$, with $\mathbf{I}$ being the identity matrix.

The Fresnel ellipsoid is very useful to visualise the relation between the permittivities $\varepsilon_{1,2,3}$ and the eigenvectors or optical axes. Let

$$\left(\frac{r_1}{\varepsilon_{r,1}}\right)^2 + \left(\frac{r_2}{\varepsilon_{r,2}}\right)^2 + \left(\frac{r_3}{\varepsilon_{r,3}}\right)^2 = 1 \tag{2.6}$$

be the ellipsoid's equation. Then the ellipsoid looks as shown in Figure 2.1 with respect to a reference composed by its eigenvectors.

Its configuration with respect to absolute coordinates would for example be obtained

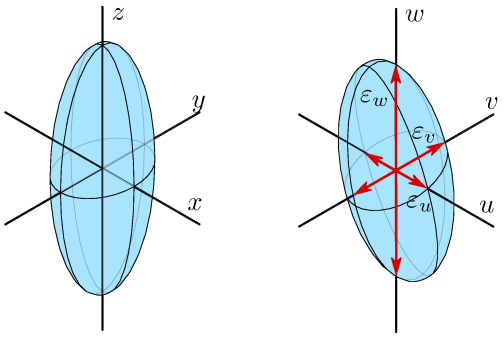

Figure 2.1.: Fresnel ellipsoid for a uniaxial dielectric. The left ellipsoid produces a tensor of only diagonal elements different from zero. The right ellipsoid is identical except for a different orientation.

by a rotation. Figure 2.1 shows this rotation. In the case of an isotropic material, the ellipsoid becomes but a sphere. This model and the optical axis have great importance for the following considerations.

Anisotropy in Liquid Crystals LC mixtures are constituted of molecules that exhibit anisotropic electronic and magnetic properties. The LC's unique properties, however, are a product of the close-by interaction of its constituents in the bulk. It is pointed out that the energy needed to orient a single molecule is orders of magnitude higher than the energy needed to orient a bulk [dP95].

Let an LC mixture be considered in its isotropic phase. All molecules are subjected to thermal agitation and thus far enough from their neighbours to experience their dipole field as quasi-isotropic. While being anisotropic on their molecular level, the liquid behaves like an isotropic material as all possible orientations exist with the same probability.

We can define two quantities:

- A factor S, ranging from 0 to 1, which will be called order parameter and
- an average vector[2] $\vec{n}_{\mathrm{LC}}$ which represents the local orientation of the LC bulk and defines the optical axis in a uniaxial birefringent crystal.

Definition 1 *Let $\vec{n}_{LC}$ be the local, effective optical axis of a small volume of LC. It will be referred to as the director of the LC.*

Each molecule can be considered cylinder-like, as shown in Figure 2.2. Its orientation is given by a vector $\vec{a}$. In the isotropic phase, all molecules are randomly distributed and the director $\vec{n}_{\mathrm{LC}}$ is undefined. In the nematic phase, the order is stronger, i.e. it

[2]The typical notation for this vector in literature is $\vec{n}$. However, since $\vec{n}$ is used as normal vector it will be denoted as $\vec{n}_{\mathrm{LC}}$.

is more likely to find a vector $\vec{a}$ which is aligned almost parallel to $\vec{n}_{\mathrm{LC}}$. A distribution $f(\theta)$, with θ being the angle between any $\vec{a}$ and the director $\vec{n}_{\mathrm{LC}}$, is larger around $\theta = 0$ than toward $\theta = \pi/2$. Since the molecules behave like induced dipoles, they do have a second order symmetry, i.e. it does not matter whether $\vec{a}$ or $-\vec{a}$ is considered.

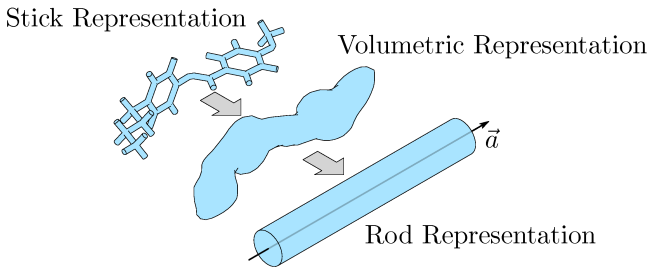

Figure 2.2.: The exemplary LC molecule N-(4-Methoxybenzylidene)-4-butylaniline (MBBA), approximate volumetric and rod representation. The latter accounts for the molecule's occupied volume in a very approximate manner and its overall dipole moment along $\vec{a}$

It is undesireable to use the function $f(\theta)$ directly, as the effect of the individual molecules' orientation provides more information than is actually needed: the dielectric nature of the material is modeled by effective dipoles anyway. It is therefore more convenient to use a scalar.

The scalar order parameter is introduced as follows.

Definition 2 *Let S be the weighted average of the angle θ over all molecules in a small volume of LC, where θ is the angle of an individual molecule with respect to the director $\vec{n}_{LC}$. It is defined as*

$$S = \int f(\theta) \frac{1}{2} \left(3\cos^2\theta - 1\right) \, d\Omega \tag{2.7}$$

Because the distribution $f(\theta)$ is actually a function of temperature, so is the order parameter.

Note, that when S goes to 0, the director becomes arbitrary (see Figure 2.3). Starting from the isotropic state, the molecules are randomly distributed, $S = 0$. All optical axes are equivalent and the Fresnel ellipsoid is a sphere.

Lowering the tempererature causes the thermal motion to decrease. The molecules interact more closely and their dipole moment plays a more important role now. This is shown in Figure 2.3. At the *clearing point* T_c, S changes rapidly, and from this point on (lower temperature) it increases continuously (see Figure 2.4). The director $\vec{n}_{\mathrm{LC}}$ is now well defined and birefringence can be observed.

Yet, in order to observe birefringence, the material must be biased by an external field. Otherwise domains of common orientation form and the material is macroscopically isotropic but a strong scatterer at most frequencies due to the domain walls.

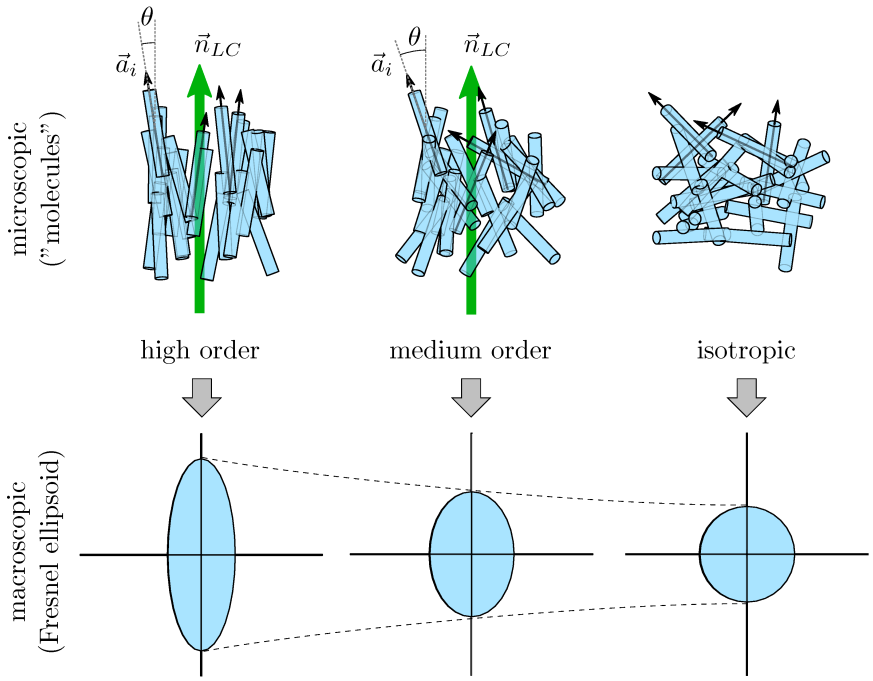

Figure 2.3.: Influence of temperature on anisotropy. Order is mainly governed by temperature. A bias field does not increase local order. Note that the local director $\vec{n}_{\mathrm{LC}}$ vanishes in the isotropic case.

When the temperature reaches the *melting point* T_m, crystallisation starts. This process is strongly dependent on the presence of crystallisation seeds or centres (i.e. impurities), composition (certain compounds may have a higher melting point than others as it can be observed in alloys' phase diagrams) or even local orientation (as domain walls may serve as crystallisation centres). At this point, strictly speaking, $S \to 1$ on the microscopic scale. The material should now be crystalline and perfectly birefringent. In reality however, this behaviour is rare due to the aforementioned reasons: most LC mixtures become polycrystalline and therefore may even become macroscopically isotropic below T_m. This is shown in Figure 2.4.

In order for the nematic LC to function as a tunable dielectric, it has to be used at a temperature $T_m < T < T_c$. The order parameter however changes continuously within this temperature range which influences the intensity of anisotropy. Rather than trying to measure S, for the scope of this work, only the canonic electrical permittivities are going to be measured since they provide all relevant data for the design.

For a given director field $\vec{n}_{\mathrm{LC}}(\vec{x})$, the permittivity tensor can be determined according to [Mül+08]

$$\varepsilon_r(\vec{x}) = \varepsilon_{r,\perp}\mathbf{I} + (\varepsilon_{r,\parallel} - \varepsilon_{r,\perp}) \cdot (\vec{n}_{\mathrm{LC}} \otimes \vec{n}_{\mathrm{LC}}) \,, \tag{2.8}$$

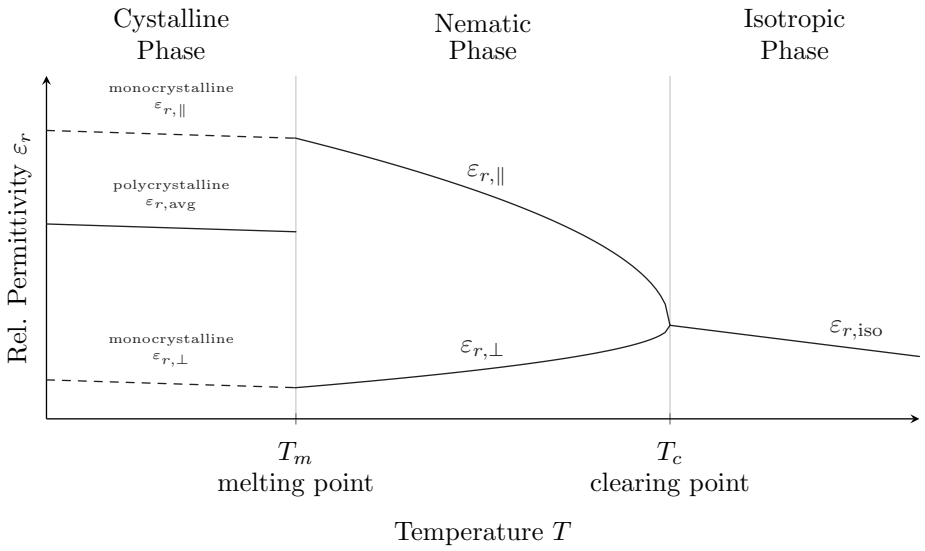

Figure 2.4.: Schematic plot of permittivity versus temperature. The crystalline phase theoretically exhibits anisotropy. However, in practice, a polycrystalline phase is obtained which exhibits some intermediate, averaged permittivity. The permittivities in the nematic phase are temperature dependent, with $\Delta\varepsilon$ decreasing with increasing temperature. At the clearing point T_c, the material becomes isotropic. Generally, permittivities may exhibit a trend with temperature – exemplified here with a negative slope.

where $\varepsilon_r(\vec{x})$ is a tensor function in space, $\mathbf{I}$ is the identity matrix and $\otimes$ denotes the outer product: $\vec{a} \otimes \vec{b} = \vec{a} \cdot \vec{b}^T$.

Measurement of both the complex relative permittivity along the optical axis $\varepsilon_{r,\parallel}$ and the complex relative permittivity perpendicular to the optical axis $\varepsilon_{r,\perp}$ is carried out with various means throughout this work. It is often not carried out over temperature, as it is difficult to design measurement systems that are able to do so.

In addition to $\varepsilon_{r,\parallel}$ and $\varepsilon_{r,\perp}$, the loss angles for the two orientations are to be measured as well. They are defined as

$$\tan\delta_\parallel = -\frac{\Im\,\varepsilon_{r,\parallel}}{\Re\,\varepsilon_{r,\parallel}} \quad \text{and} \quad \tan\delta_\perp = -\frac{\Im\,\varepsilon_{r,\perp}}{\Re\,\varepsilon_{r,\perp}}. \tag{2.9}$$

For simplicity, $\varepsilon_{r,\parallel}$ and $\varepsilon_{r,\perp}$ will, unless otherwise specified, refer to their real parts and the imaginary part will be only indirectly used in the form of $\tan\delta_\parallel$ and $\tan\delta_\perp$ which are purely real.

For technical reasons, performance comparison and certain design rules, the following definitions are introduced:

Definition 3 *The material tunability τ is defined as the relative permittivity difference between parallel with and orthogonal to the optical axis, i.e. the material's birefringence,*

$$\tau = \frac{\left|\varepsilon_{r,\parallel} - \varepsilon_{r,\perp}\right|}{\max\left(\varepsilon_{r,\parallel}, \varepsilon_{r,\perp}\right)}. \tag{2.10}$$

In the case that $\varepsilon_{r,\parallel} > \varepsilon_{r,\perp}$, this reduces to

$$\tau = \frac{\varepsilon_{r,\parallel} - \varepsilon_{r,\perp}}{\varepsilon_{r,\parallel}}. \tag{2.11}$$

It is typically given in per cent (%).

Definition 4 *The material tuning efficiency or the material figure of merit η is defined as the ratio of material tunability over maximum loss angle*

$$\eta = \frac{\tau}{\max\left(\tan\delta_{\parallel}, \tan\delta_{\perp}\right)}. \tag{2.12}$$

τ is given in decimal values and has no unit.

Frequency Dependency It should be noted that the dielectric properties are functions of frequency. Permittivity is, as defined at the beginning of this chapter, the result of charges attached to matter being polarised by an electric field. This mechanism is causal and non-instantaneous, i.e. it involves a certain effective mass of the charge and a potential field that keeps the charge close to the matter in question. In other words, a mass-spring model like the Debye model for dielectric relaxation is used to describe these interactions.

Charge has several possibilities to move. It can move as permanent charge or as permanent dipoles, causing displacement of the matter. It can also move and form induced dipoles (polarisation). The nature of these dipoles and their interaction with the matter defines the characteristic time dependence, or frequency at which the mechanism goes into resonance with the electric field. This process is called relaxation and its characteristic frequency is called relaxation frequency.

A dielectric can exhibit several such processes – and as such frequencies – resulting in a rather complex frequency dependence of the permittivity (function). Each of these relaxations comes with a peak in caloric losses and a drop in the real part of permittivity.

Very generally and simplified, the permittivity of dielectrics follows a series of Debye relaxations

$$\varepsilon = \varepsilon_{\infty} + \sum_i \frac{\Delta\varepsilon_i}{1 + j\omega/\omega_i}, \tag{2.13}$$

which is a first order model and the dominant model in LCs.

Other relaxation mechanisms may be more accurately represented by other relaxation models. But as a general rule, they add to the overall permittivity.

The relaxations generally are not the same for $\varepsilon_{r,\parallel}$ and $\varepsilon_{r,\perp}$ because orientation plays an important role for polarisation. Consequently, the permittivities at a certain RF frequency are not equivalent to the permittivities, say, close to DC (direct current). They are much higher at low frequencies.

However, LC mixtures are designed to exhibit strong anisotropy in the DC region. The electric energy stored in the LC is therefore dependent of the orientation of the director with respect to the electric (DC) field. As the system tends to minimise its Gibbs free energy, this DC anisotropy can be used to orient the directors and dynamically switch their orientation.

2.3. Dynamic Aspects

In the previous sections, mainly static or quasi-static properties have been discussed. This section will briefly discuss the dynamic properties of LC.

Like other liquids, LC exhibits shear stress, i.e. a stress ($\mathrm{d}F/\mathrm{d}A$) which is proportional to the local change in velocity ($\mathrm{d}v/\mathrm{d}r$). The resulting dynamic viscosity[3] is defined by

$$\frac{\mathrm{d}F}{\mathrm{d}A} = \gamma \frac{\mathrm{d}\dot{r}_x}{\mathrm{d}r_{y,z}}. \tag{2.14}$$

Therefore, any flow will be inhibited by a counterforce. Additionally, unlike liquids but similar to solids, LC exhibits shear forces due to internal deformation of the director field $\vec{n}_{\mathrm{LC}}(\vec{r})$.

The molecular interaction does not only cause anisotropic reaction to electromagnetic stimulus. It induces torques on neighbouring molecules, hence inducing mechanical stress and strain. This is a peculiar property of LC. As a result, the continuum stores free energy based on its director field deformation which consists of the following relevant terms:

- electric potential energy,
- magnetic potential energy, as well as
- splay,
- twist and
- bend deformation (i.e. potential) energy.

The last three describe the potential energy stored in a perturbed director field due to distortions of the kinds shown in Figure 2.5.

This problem has been extensively studied and all the relevant aspects for this work can be found in [Gäb15]. Furthermore, there is a software package designed to

[3] Many sources referenced in this work use the symbol γ for viscosity, probably due to the habit of de Gennes and Prost. However, according to many other sources, η and sometimes μ are preferred. Since in this work, η is used for material FoM and μ is commonly referred to as magnetic permeability, instead γ is used in coherence with previous practice.

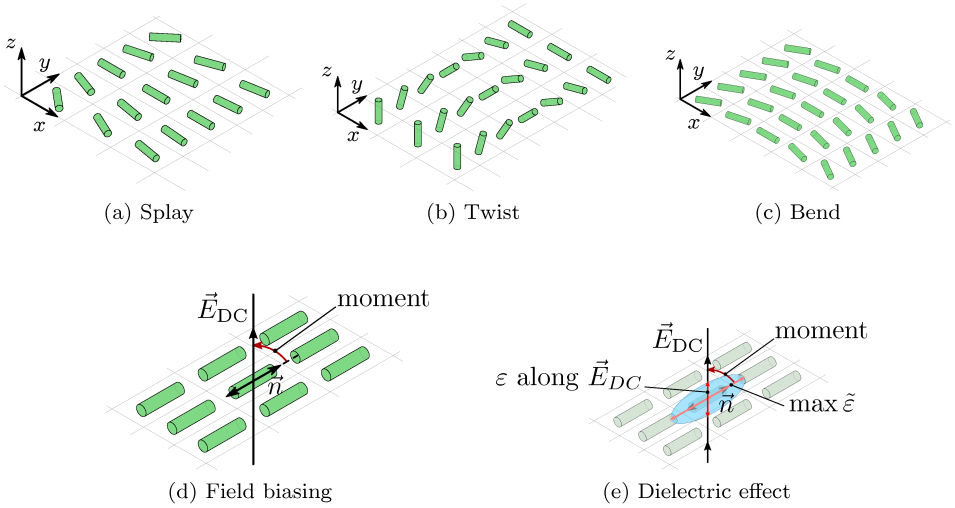

(a) Splay (b) Twist (c) Bend

(d) Field biasing (e) Dielectric effect

Figure 2.5.: Visualisation of the five ways of storing potential energy in a director field: (a) diverging configurations store energy $\mathcal{F}_{\mathrm{splay}}$ towards the defect (towards top left of the figure), (b) torsion- or twist-like configurations (out-of-plane bends) stores energy $\mathcal{F}_{\mathrm{twist}}$ due to the nematic nature and (c) a bend orthogonal to the director field store energy $\mathcal{F}_{\mathrm{bend}}$. Furthermore, (d)+(e) an external biasing field $\vec{E}_{\mathrm{DC}}$ or $\vec{H}$ *or both* store energy ($\mathcal{F}_{\mathrm{el}} + \mathcal{F}_{\mathrm{mag}}$). N.b. that field biasing works in a similar way for magnetic biasing due to the anisotropic nature of the permeability.

simulate the evolution of the director field in microwave structures for 2D and 2.5D problems which covers all topologies discussed in this thesis and has been used for design and verification purposes. In the following, however, the basic concepts of director dynamics will be introduced as they are important for understanding certain choices made throughout the following chapters.

We start by formulating the free energy with all relevant terms:

$$\int_V f \,\mathrm{d}V = \mathcal{F} = \mathcal{F}_{\mathrm{splay}} + \mathcal{F}_{\mathrm{twist}} + \mathcal{F}_{\mathrm{bend}} + \mathcal{F}_{\mathrm{el}} + \mathcal{F}_{\mathrm{mag}} \tag{2.15}$$

The energy density f stored in a unit volume of nematic liquid is a function of the deformation of its director field $\vec{n}_{\mathrm{LC}}(\vec{r})$.

$$\mathcal{F}_{\mathrm{def.}} = \underbrace{\int_V \frac{K_1}{2} \left(\operatorname{div} \vec{n}_{\mathrm{LC}}\right)^2 \,\mathrm{d}V}_{=\mathcal{F}_{\mathrm{splay}}} + \underbrace{\int_V \frac{K_2}{2} \left(\vec{n}_{\mathrm{LC}} \cdot \operatorname{curl} \vec{n}_{\mathrm{LC}}\right)^2 \,\mathrm{d}V}_{=\mathcal{F}_{\mathrm{twist}}} + \underbrace{\int_V \frac{K_3}{2} \left(\vec{n}_{\mathrm{LC}} \times \operatorname{curl} \vec{n}_{\mathrm{LC}}\right)^2 \,\mathrm{d}V}_{=\mathcal{F}_{\mathrm{bend}}}, \tag{2.16}$$

where K_1 corresponds to conformations of splay, K_2 to those of twist and K_3 to those of bend. The constants are positive and of unit Energy per unit length which is N in SI units [dP95]. Another common notation is K_{ij} where K_2 would, for example, correspond to K_{22}.

The electric and magnetic energy densities [Mül06] are given by

$$\mathcal{F}_{\text{bias}} = \underbrace{\int_V \varepsilon_\perp \left|\vec{E}\right|^2 + \left(\varepsilon_\parallel - \varepsilon_\perp\right) \cdot \left(\vec{n} \cdot \vec{E}\right)^2 \, \mathrm{d}V}_{=\mathcal{F}_{\text{el}}} + \underbrace{\int_V \varepsilon_\perp \left|\vec{H}\right|^2 + \left(\mu_\parallel - \mu_\perp\right) \cdot \left(\vec{n} \cdot \vec{H}\right)^2 \, \mathrm{d}V}_{=\mathcal{F}_{\text{mag}}} . \tag{2.17}$$

When the order of magnitude and the properties of the K_i are considered, two remarks will be of interest for this work:

- The order of magnitude for all K_i is 1×10^{-11} N.
- The values of K_i are strongly temperature dependent. They are roughly proportional to the square order parameter [dP95; GM73; Gru73].

This leads to the definition of switching speed and provides a relation with geometry and applied voltage or field strength. The temporal evolution is highly non-linear and tends to become asymptotic in most cases. Therefore a common definition from electronics and the field of LC displays is applied:

Definition 5 *The relevant off-on switching time τ_{90}^{10} is defined as the time between 10 % and 90 % of the maximum absolute phase shift of the phase shifter device. The relevant on-off switching time τ_{10}^{90} is defined as the time between 90 % and 10 % of the maximum absolute phase shift.*

The asymptotic switching time on the other hand can be derived from director dynamics calculations (cf. [YW06], Chapter 5.3 in particular).

Definition 6 *The asymptotic switching time τ_{sw} is defined as the total time it takes for an LC device to go from on to off state.*

Typically, two switching directions result in a slow and a fast direction. Where relevant, these are indicated with an index $\tau_{\text{sw}}^{\text{fast}}$ or τ_{sw},$^{\text{slow}}$ respectively. The equation given in [YW06], Eq. 5.82, for the switching time as a function of electric field and rotational viscosity in a parallel plate capacitor geometry (Figure 2.6) shows that the switch-on time is

$$\tau_{\text{sw}}^{\text{on}} = \frac{\gamma_{\text{r}}}{K_{22}} \left(\frac{h}{\pi}\right)^2 \frac{1}{\left(E/E_{\text{C}}\right)^2 - 1} \tag{2.18}$$

where h is the height of the cell.

It should be noted though, that this implies the presence of an electric field *and* of a counterforce, typically implemented by surface anchoring, which will not be considered in this work. It is therefore important to discuss alternative biasing schemes.

2.4. Biasing Schemes

2.4.1. Classical Biasing: Anchoring vs. Electric Field

The classical approach exploits the fact that most LC devices up to now have been planar structures. In these, the effect of surfaces on the bulk is comparatively large.

Biasing in these structures is achieved by placing two electrodes at a small distance and treat their surfaces in a way such that there is a preferred orientation for the nematic LC in contact. With no voltage applied, the mechanical properties treated previously force a near homogeneous orientation of the hole bulk (see Figure 2.6a).

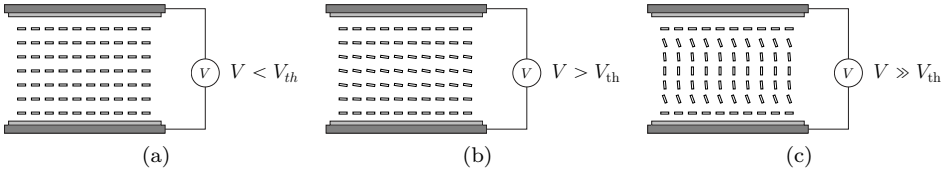

Figure 2.6.: Biasing of anchored LC: (a) fully homogeneous orientation enforced by the surface conditions. (b) Onset of reorientation by applied electric field. (c) Saturation state where surface effect is almost fully eclipsed by electric field effect.

Applying a voltage larger than the threshold voltage V_{th} starts the reorientation process. The directors experience a torque, turning them towards the electric field lines (Figure 2.6b). The threshold field

$$V_{\mathrm{th}} = \pi \sqrt{\frac{K_{ii}}{\varepsilon_0 \Delta\varepsilon_{\mathrm{DC}}}} \tag{2.19}$$

with elastic constant K_{ii} (with $i = 3$ for the bend geometry shown here), and low-frequency anisotropy $\Delta\varepsilon_{\mathrm{DC}}$ [YW06]. Below this threshold, the "decrease of the electric energy cannot compensate for the increase in elastic energy" [YW06]. Above the threshold however, reorientation occurs.

The time it takes to relax from fully tilted to fully surface aligned (relaxed) state is defined by

$$\tau_{\mathrm{off}} = \frac{\gamma_r}{K_{22}} \left(\frac{h}{\pi} \right)^2 . \tag{2.20}$$

The opposite direction depends on the applied electric field and is defined by

$$\tau_{\mathrm{on}} = \frac{\tau_{\mathrm{off}}}{(E/E_{\mathrm{th}})^2 - 1}. \tag{2.21}$$

It should be noted that, although the expression is derived from a twist geometry, the order of magnitude for the on and off times is comparable also for splay and bend

geometry. Table 2.1 shows the switching times for two Merck LCs and compares them to generic display LCs.

Looking at the switching times, an LC layer thickness of approximately 10 µm and a biasing voltage above 30 V seems a reasonable combination for microwave devices. It can therefore be concluded that the above mentioned geometry is well suited for many planar topologies where dielectric layers are thin and signal lines can be electrically biased. However, for several reasons this is not the case in hollow waveguides.

2.4.2. All-electric Biasing

Hollow waveguides require a different biasing strategy. Anchoring is impractical for two reasons:

- Below 1 THz, the waveguide height is far above 100 µm, which results in extremely large switch-off times (cf. Table 2.1, note the square dependency of switch-off time with cell height), and
- while τ_{on} depends on the applied electric field, τ_{off} does not, hence the switching times diverge for larger cell heights.

The solution is to use all-electric biasing which is schematically described in Figure 2.7.

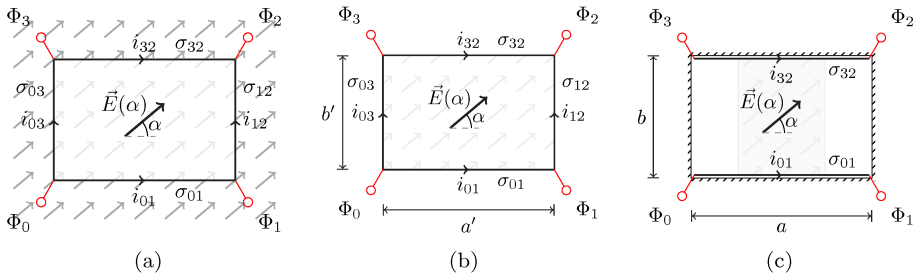

Figure 2.7.: All-electric biasing: (a) a homogeneous electric field $\vec{E}(\alpha)$ induces currents on a rectangular tube's surfaces. (b) Inversely, applying potentials Φ_n accordingly, a homogeneous electric field is created. (c) Simplified, RF-friendly structure creates an electric field which can be considered homogeneous in the waveguide's centre while being significantly deformed toward the left and right the edges in particular.

A volume—or in the case of long, quasi-twodimensional geometries, an area—is enclosed by a set of electrodes, i.e. conductive lines. The desired electric field configuration in the area enclosed by these electrodes is obtained by imprinting a current which results in a specified voltage drop or potential distribution along the lines. In theory, using this method, many field configurations can be obtained. If the shape of

		GT5-28004		**GT3-23001**		**generic display LC**	
h/µm	V_{bias}/V	τ_{on}/s	τ_{off}/s	τ_{on}/s	τ_{off}/s	τ_{on}/s	τ_{off}/s
100	10	7.26	253	2.52	101	143×10^{-3}	10.1
100	30	787×10^{-3}	253	274×10^{-3}	101	15.7×10^{-3}	10.1
100	100	70.6×10^{-3}	253	24.6×10^{-3}	101	1.41×10^{-3}	10.1
10	10	72.6×10^{-3}	2.53	25.2×10^{-3}	1.01	1.43×10^{-3}	101×10^{-3}
10	30	7.87×10^{-3}	2.53	2.74×10^{-3}	1.01	157×10^{-6}	101×10^{-3}
10	100	706×10^{-6}	2.53	246×10^{-6}	1.01	14.1×10^{-6}	101×10^{-3}
1	10	726×10^{-6}	25.3×10^{-3}	252×10^{-6}	10.1×10^{-3}	14.3×10^{-6}	1.01×10^{-3}
1	30	78.7×10^{-6}	25.3×10^{-3}	27.4×10^{-6}	10.1×10^{-3}	1.57×10^{-6}	1.01×10^{-3}
1	100	7.06×10^{-6}	25.3×10^{-3}	2.46×10^{-6}	10.1×10^{-3}	141×10^{-9}	1.01×10^{-3}
		$V_{\mathrm{th}} \approx 1.67\,\mathrm{V}$		$V_{\mathrm{th}} \approx 1.56\,\mathrm{V}$		$V_{\mathrm{th}} \approx 1.18\,\mathrm{V}$	
		$K_{ii} \approx 10 \times 10^{-12}\,\mathrm{N}$		$K_i \approx 10 \times 10^{-12}\,\mathrm{N}$		$K_i \approx 10 \times 10^{-12}\,\mathrm{N}$	
		$\gamma_r \approx 2.5 \times 10^3\,\mathrm{mPas}$		$\gamma_r \approx 1.0 \times 10^3\,\mathrm{mPas}$		$\gamma_r \approx 100\,\mathrm{mPas}$	
		$\Delta\varepsilon_{\mathrm{DC}} \approx 4.0$		$\Delta\varepsilon_{\mathrm{DC}} \approx 4.6$		$\Delta\varepsilon_{\mathrm{DC}} \approx 8.0$	

Table 2.1.: Comparison of two LCs (Merck Licristal® GT3-23001 and GT5-28004) used throughout this work with generic display LC (typical values from [YW06]). Note the large differences in switching time both between on and off for a given LC as well as over the parameter change and the LCs.

the enclosing electrodes is not constrained (for example by conditions for the guiding of RF waves), virtually any smooth electric field configuration can be obtained.

The downside of this approach (imprinted current) is the Ohmic power dissipation. An alternative approach consists in the segmentation of the electrodes, thereby obtaining a stepped potential distribution, which can be generated from a low number of voltage sources by means of a resistive voltage divider network. At the limit, this approach is the same as the one discussed before and will be used in Chapter 4.

Table 2.2 lists all LC mixtures used for devices in this thesis. The 19 GHz data is courtesy Merck KGaA, Darmstadt (Merck), the 30 GHz data is extracted using the method described in Chapter 3.

	Material	$\varepsilon_{r,\perp}$	$\tan\delta_\perp$	$\varepsilon_{r,\parallel}$	$\tan\delta_\parallel$	**Viscosity**
19 GHz	GT3-23001	2.46	14.3×10^{-3}	3.28	3.8×10^{-3}	average high
	GT5-26001	2.39	7.0×10^{-3}	3.27	2.2×10^{-3}	average high
	GT5-28004	2.40	4.3×10^{-3}	3.32	1.4×10^{-3}	very high
	TUD-566	2.41	6.0×10^{-3}	3.34	2.7×10^{-3}	average high
30 GHz	GT3-23001	2.57	51.1×10^{-3}	3.22	34.9×10^{-3}	average high
	GT5-26001	2.51	24.1×10^{-3}	3.27	34.1×10^{-3}	average high
	GT5-28004	data not available				very high
	TUD-566	data not available				average high

Table 2.2.: List of LC mixtures used in this work and their dielectric properties. 19 GHz data is provided courtesy Merck, 30 GHz data is extracted using the method in Chapter 3. Viscosity of LC mixtures for microwave and mm-wave applications is generally high.

2.5. Conclusion

The static as well as the dynamic behaviour of LCs have been presented in this chapter. Benchmark figures for the development of LC mixtures, modeling of RF devices and their analysis have been defined. LCs are a complex but well understood material. The explanations have been reduced to what is necessary for the frequency range considered in this work.

Using the expressions for the permittivity tensor and in particular the notion of the permittivity eigenvalues along a given axis, it is possible to reduce the design procedure for LC devices to the two extreme cases “parallel” and “perpendicular”. Furthermore, for flat structures, the switching time can be estimated using equations presented in this section. Unfortunately, the switching time of bulk structures discussed in this thesis is subject to numerical calculations or experimental results. At last, the methodology of all-electric biasing introduces new degrees of freedom for the design of compact RF devices, central to the design of phase shifters in this work.

3. Characterisation of Liquid Crystals from Millimetre Wave to Terahertz

This chapter treats the field of LC characterisation over a wide frequency range. Previously, characterisation methods have covered mainly the microwave range up to the Ka-band [Gäb+08a; Kar+10; Gäb+10; Gäb15]. Two approaches were pursued: wideband measurements (e.g. [Kar+10; Mül+08]) and resonant measurements with rectangular cavities [Gäb+08a; Gäb+10], or a cylindrical cavity [Gäb15]. It soon turned out to become more and more complicated to implement resonant measurement setups beyond 30 GHz. W-band wideband measurements were presented, but no resonant cavities in this range [Mül+08].

An important reason for this is the crippling effect increasing frequencies have on the quality factor of the resonators. Most resonant methods employ the modes TM_{010} and TE_{111}. They are generally easy to design, the modes are well separated in frequency and can be excited easily. Higher order modes, however, may offer a significantly higher quality factor than TM_{010} and TE_{111}.

Cylindrical shapes are preferred for the characterisation of LC in particular: they exhibit exactly one symmetry axis, just as bi-refringent materials do, and they are easy to fabricate in a very precise manner using drills or on a metalworking lathe.

3.1. Introduction

LCs, as discussed in Chapter 2, are anisotropic materials. So, throughout this chapter, only pairs of modes are considered where one exhibits ideally a purely axial and the other a purely transversal electric field. Finding such a pair becomes more challenging for higher order modes, since the mode spectrum naturally grows denser. This can be observed in Figure 3.1 which depicts a mode chart for the lowest 11 modes of a cylindrical cavity of varying aspect ratios.

For low frequencies, i. e. for large cavities, characterisation of a material under test (MUT), where it is introduced into the cavity as a perturbation, leaves the mode chart largely intact. This holds for all types of cavities, not only cylindrical cavities. In particular the loci of the modes' resonant frequencies for a given aspect ratio are only minorly influenced.

This changes with increasing frequency, as the cavities shrink while the sample's dimensions usually have some sort of lower boundary (e.g. machineability, fragility, etc.).

Another aspect is that the MUT in this case is a liquid. It has therefore to be introduced into the cavity held by a container. Currently, this is a tube of low-tan δ

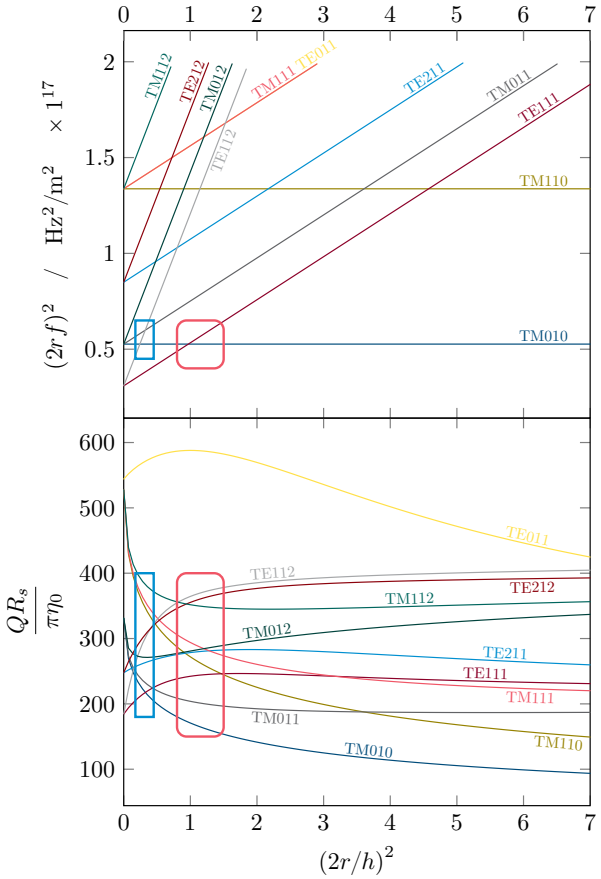

Figure 3.1.: Depiction of resonance modes over varying aspect ratio (r is radius, h is height) and corresponding Q factor. The rounded box (red) marks the aspect ratio, and the frequency and Q factor range used in classical resonators. Gäbler [Gäb15] uses a different approach, marked by the blue rectangle (sharp corners).

quartz. But in order to keep mechanical handling practical its size cannot be reduced infinitely and the tube has to remain robust. Therefore, the ratio of "filling" to cavity volume becomes less and less favourable and the above mentioned effect more and more pronounced.

Approximations like the cavity perturbation method (CPM) and the assumption that the device is a cylindrical cavity rather than an axially perforated cylinder become less accurate or even break. In order to replace the CPM, Kalesinskas and Konstantinov [KK99] as well as later Gäbler et al. [Gäb+10] discussed a method which inverts the eigenvalue problem of the cavity in such a way, that it solves for

the permittivity of the perturber: the eigen-permittivity ansatz.

Even higher frequencies make resonant cavities altogether unfavourable. The use of metals as a material is generally avoided in the THz range. Dielectric (multilayer) resonators using the Fabry-Pérot effect could be used instead. If for example a distributed feedback (DFB) grating is to be used as a mirror, the dielectric layer thicknesses necessary to realise such a grating for THz frequencies are very hard to realise (only some tens of micrometers depending on the refractive index of the material) and no such device is known to the author to be reported. The layers would, on one hand, be too thick for methods available in thin-film technology (e.g. chemical vapour deposition, CVD). On the other hand, they would be too thin to be obtained for example by laminating alternating layers of plastic sheets.

The structure of this chapter can therefore be summarised as follows: the first section of this chapter treats the derivation of the resonator Helmholtz equations in Finite Element Method (FEM) using the FEniCS Project (FEniCS) [LMW12], the extraction of the resonance frequency for a given geometry and material distribution (called *direct* method), and of the potential extraction of material parameters using the eigen-permittivity ansatz (called *inverse* method). This will allow using higher-order modes as a basis to increase the Q factor.

The second section applies the method to higher-order modes and discusses its limitations and fabrication issues.

The third section, inspired by work of Vieweg [Vie11; VSK11; Vie+12], takes a look at two methods of LC characterisation in the Terahertz range: from 100 GHz to 2.5 THz using Time-Domain Spectroscopy (TDS) and from 2 THz to 8 THz using Fourier Transform Interferometry spectroscopy.

3.2. Perturbed Resonators for Material Characterisation Using Finite Element Method in FEniCS

One way of characterising materials is using the detuning of a resonator to determine the permittivity (or permeability) of a small, geometrically well-defined perturber. This takes advantage of the fact that in resonance, the interaction of material and Radio Frequency (RF) field is dramatically enhanced. The Q factor of the cavity is a gauge of the number of round-trips the wave takes in the resonator before it fades. For small perturbations the detuning effect has little to no effect on the field shape. Therefore historically, the initial ansatz was to solve for the unloaded field using Helmholtz' equation and account for the shift in frequency, which corresponds to the shift of the eigenvalues of said equation, by introducing the perturbation term: the integral over the volume of the perturber.

The frequency shift $\Delta\omega$ is given by

$$\Delta\omega = \frac{\omega}{\omega_0} - 1 \approx \frac{\int\limits_{\Omega_p} \left(\Delta\varepsilon \left| \vec{E}_0 \right|^2 + \Delta\mu \left| \vec{H}_0 \right|^2 \right) \mathrm{d}V}{\int\limits_{\Omega_0} \left(\varepsilon \left| \vec{E}_0 \right|^2 + \mu \left| \vec{H}_0 \right|^2 \right) \mathrm{d}V}, \tag{3.1}$$

where ω and ω_0 are the perturbed and unperturbed resonance frequencies, respectively, Ω_0 is the volume of the cavity, Ω_p the volume of the perturber, $\Delta\varepsilon$ and $\Delta\mu$ the change in permittivity and permeability, respectively, and $\vec{E}_0$ and $\vec{H}_0$ the unperturbed fields [Poz11, based on eq. 6.100]. This approach uses the fact that for small perturbers the general shape of the fields is preserved.

With the rise of numeric capabilities of computers, the method was not bound to the perturbation approximation anymore. A first approach using the method of moments was proposed by Kalesinskas and Konstantinov [KK99]. Ten years later Gäbler et al. proposed a similar approach, first using a perturbation approach [Gäb+09a]. Later, the method was extended to using fields obtained by an FDFD-based eigenvalue problem [Gäb+10].

The method is applicable whenever the problem has the form of an eigenvalue problem (EVP). In the specific example, the eigenvalue in question is the propagation constant β of an arbitrarily shaped waveguide. An implication of this was the use in the Helmholtz equation of a resonator. To this end, Gäbler applied the method to the TE_{111} and TM_{010} modes of 12 and 19 GHz cylindrical cavity resonators, though it was not published until 2015, [Gäb15, Sec. 4.3, pp. 70ff].

It is extremely useful for problems that can be described in a simple numerical or even analytical fashion. However, it proved to be very inflexible in terms of more complex geometries. In order to model the influence of the filling hole, where the quartz tube is inserted, a series field expansion was necessary that would account for the downshift in resonance frequency due to the filling hole [Gäb15, Sec. 4.1.2, pp. 47ff]. This seemed like an unattractive "tweak" to an otherwise effective and elegant approach. Moreover, no standardised interface or description was available to describe the geometry and more complex cross-sections with variations along both axes (r and z) were not implementable.

This sparked the idea of generalising the problem and discretise the domain in both axes r and z. This was facilitated by versatile software packages like FEniCS [LMW12] and SLEPc [HRV05]. Based on these, the FEM is used for the analysis of more complex resonator geometries.

The first issue is complexity. As previous work has shown, characterisation of uniaxial materials like LC (or isotropic materials for that matter) is best carried out using high-Q cylindrical cavities. The complexity of their numerical desciption is highly reduced by incorporating the symmetry into the ansatz and henceforth solve in axisymmetric coordinates, thus reducing the 3D problem into a quasi-2D problem. The derivation is briefly shown in the following section. Some details which are important

for the technical implementation but less so for the general understanding are explained in the Mathematical Appendix A.1.

3.2.1. Derivation of the Direct Problem

Monochromatic (harmonic) electric fields obey the electromagnetic wave equation (the Helmholtz equation in vectorial form)

$$\vec{\nabla}^2 \vec{E} + k^2 \vec{E} = 0, \tag{3.2}$$

with $\vec{\nabla}^2$ being the element-wise Laplace operator ∇^2, $\vec{E}$ the harmonic electric field and k the wave number of the resonant mode.

The cylindrical coordinate system along r, ϕ and z is chosen as only axisymmetric geometries are considered here. Hence, the fields within the cavity are described using their real-valued electric field components

$$\vec{E}_{\{r,z\}}(r, \varphi, z) = \vec{E}_{\{r,z\}}(r, z) \cdot \sin(m \cdot \varphi) \tag{3.3}$$

$$\vec{E}_{\varphi}(r, \varphi, z) = \vec{E}_{\varphi}(r, z) \cdot \cos(m \cdot \varphi) \tag{3.4}$$

with m being the mode-number in φ-direction. These currently have to be real-valued ansatz functions since FEniCS in version 1.6.0 and its interface to SLEPc only support real numbers. However, a more general approach would be to model the fields as complex-valued.

By gauging $\vec{E}$ to be divergence free and steps laid out in Appendix A.1, the wave equations in cylindrical coordinates can be expressed as

$$\nabla^2(E_r \sin m\varphi) - \frac{1}{r^2}(E_r \sin m\varphi) - \frac{2}{r^2}\partial_\varphi(E_\varphi \cos m\varphi) \quad + k^2(E_r \sin m\varphi) = 0, \tag{3.5}$$

$$\nabla^2(E_\varphi \cos m\varphi) - \frac{1}{r^2}(E_\varphi \cos m\varphi) + \frac{2}{r^2}\partial_\varphi(E_r \sin m\varphi) \quad + k^2(E_\varphi \cos m\varphi) = 0, \tag{3.6}$$

$$\nabla^2(E_z \sin m\varphi) \quad + k^2(E_r \sin m\varphi) = 0, \tag{3.7}$$

where the $\sin m\varphi$ and $\cos m\varphi$ dependencies stem self-consistently from the system of equations. A special case poses $m = 0$, where $E_{\{r,z\}}$ and E_φ decouple. In this case, the TE modes are fully described by the E_φ component,

$$\nabla^2 E_\varphi + \frac{1}{r^2} E_\varphi + k^2 E_\varphi = 0, \tag{3.8}$$

and the TM modes by the $E_{\{r,z\}}$ components,

$$\nabla^2 E_z + \nabla^2 E_r - \left(\frac{1}{r^2} - 2k^2\right) E_r = 0. \tag{3.9}$$

The FEM formulation requires the differential equation to be expressed in its weak form, using the trial field $\vec{\mathcal{E}}$. Nelson [Nel93] suggests substituting $\tilde{\vec{E}}_\varphi = r \cdot \vec{E}_\varphi$ and

$\tilde{\vec{\mathcal{E}}}_\varphi = r \cdot \vec{\mathcal{E}}_\varphi$. After applying vector identities, integration and application of φ symmetry as detailed in the appendix, the expressions to be treated are

$$\iint_\Omega \left(\nabla_{rz} \times \vec{E}_{rz}\right) \left(\nabla_{rz} \times \vec{\mathcal{E}}_{rz}\right) r \,\mathrm{d}r \,\mathrm{d}z = k_0^2 \iint_\Omega \varepsilon_r(x)\, \vec{E}_{rz} \vec{\mathcal{E}}_{rz}\, r \,\mathrm{d}r \,\mathrm{d}z \tag{3.10}$$

$$\iint_\Omega \frac{1}{r} \left(m\vec{E}_{rz} - \nabla_{rz} \cdot \tilde{\vec{E}}_\varphi\right) \frac{1}{r} \left(m\vec{\mathcal{E}}_{rz} - \nabla_{rz} \cdot \tilde{\vec{\mathcal{E}}}_\varphi\right) r \,\mathrm{d}r \,\mathrm{d}z = k_0^2 \iint_\Omega \frac{1}{r^2} \varepsilon_r(x)\, \tilde{\vec{E}}_\varphi \tilde{\vec{\mathcal{E}}}_\varphi\, r \,\mathrm{d}r \,\mathrm{d}z \tag{3.11}$$

A full discussion of the properties of the problem and its derivation with respect to cylindrical symmetry is given in [Nel93].

The right-hand side (r.h.s.) terms of (3.10) and (3.11) can be expressed in terms of a spatial distribution of relative permittivity-values $\varepsilon_r(r, z)$, granted that the material distribution obeys cylindrical symmetry. The system now has a form similar to an EVP. $\vec{E}_{\{rz,\varphi\}}$ and $\vec{\mathcal{E}}_{\{rz,\varphi\}}$ are approximated in terms of their finite basis functions or finite elements, where

$$\vec{E}_\varphi,\, \vec{E}_{rz} = \sum_i \alpha_i w_i(x) \quad \text{and} \tag{3.12}$$

$$\vec{\mathcal{E}}_\varphi,\, \vec{\mathcal{E}}_{rz} = \sum_i \beta_j w_j(x). \tag{3.13}$$

Each integral is assembled by FEniCS and yields an *operator* (matrix) and a *vector* (the trial field) such that

$$\int_\Omega \vec{E} \cdot \vec{\mathcal{E}} \,\mathrm{d}x = \int_\Omega \sum_i \alpha_i w_i(x) \cdot \sum_i \beta_j w_j(x) \,\mathrm{d}x \tag{3.14}$$

$$= \sum_i \sum_j \underbrace{\alpha_i}_{\substack{\text{coefficient}\\ \text{vector}}} \underbrace{\cdot \beta_j \int_\Omega w_j(x) \cdot w_j(x) \,\mathrm{d}x}_{\substack{\text{Operator}\\ \text{sparse matrix } M}} \tag{3.15}$$

$$= M \cdot \vec{x} \tag{3.16}$$

All integrals basically assume the shape of matrix operators on vectors, where the exact shape of the operator depends on the operator in the analytic equation. Applied to (3.10) for example this yields

$$\underbrace{\iint_\Omega \left(\nabla_{rz} \times \vec{E}_{rz}\right) \left(\nabla_{rz} \times \vec{\mathcal{E}}_{rz}\right) r \,\mathrm{d}r \,\mathrm{d}z}_{\mathbf{A}\cdot\vec{x}} \underbrace{- k_0^2 \iint_\Omega \varepsilon_r(x)\, \vec{E}_{rz} \vec{\mathcal{E}}_{rz}\, r \,\mathrm{d}r \,\mathrm{d}z}_{\mathbf{B}\cdot\vec{x}} = 0, \tag{3.17}$$

where k_0^2 corresponds to the eigenvalue of the equation.

This discretised Helmholtz equation therefore assumes the form of a generalised EVP:

$$\mathbf{A}\vec{x} - \lambda\mathbf{B}\vec{x} = 0. \tag{3.18}$$

The discretisation and creation of the matices $\mathbf{A}$ and $\mathbf{B}$ is entirely left for FEniCS to do. This makes reformulations easier, since they only take place in the analytic description.

With (3.10) and (3.11) the *direct* problem, i.e. the Helmholtz equation in cylindrical coordinates is fully defined.

3.2.2. Derivation of the Inverse Problem (Eigen-permittivity)

If $\varepsilon_r(r, z)$ is piecewise constant on a number of subdomains, the r.h.s. integral splits into a sum of integrals of the respective subdomains. This is the most common case where no continuous change in permittivity is allowed. If all r.h.s. integrals but the one corresponding to the MUT are moved to the left-hand side (l.h.s.), the problem can be reformulated to make the permittivity $\varepsilon_{r,\mathrm{MUT}}$ the eigenvalue. Thus, (3.10) and (3.11) become

$$\iint_\Omega \left(\nabla_{rz} \times \vec{E}_{rz}\right)\left(\nabla_{rz} \times \vec{\mathcal{E}}_{rz}\right) r\,\mathrm{d}r\,\mathrm{d}z - \sum_{\Omega_n \backslash \Omega_{\mathrm{MUT}}} \varepsilon_{r,n} \iint_\Omega k_0^2 \vec{E}_{rz}\vec{\mathcal{E}}_{rz}\, r\,\mathrm{d}r\,\mathrm{d}z = \varepsilon_{r,\mathrm{MUT}} \iint_\Omega k_0^2 \vec{E}_{rz}\vec{\mathcal{E}}_{rz}\, r\,\mathrm{d}r\,\mathrm{d}z, \tag{3.19a}$$

$$\iint_\Omega \frac{1}{r}\left(m\vec{E}_{rz} - \nabla_{rz}\cdot\tilde{\vec{E}}_\varphi\right)\frac{1}{r}\left(m\vec{\mathcal{E}}_{rz} - \nabla_{rz}\cdot\tilde{\vec{\mathcal{E}}}_\varphi\right) r\,\mathrm{d}r\,\mathrm{d}z - \sum_{\Omega_n \backslash \Omega_{\mathrm{MUT}}} \varepsilon_{r,n} \iint_\Omega \frac{k_0^2}{r^2}\tilde{\vec{E}}_\varphi\tilde{\vec{\mathcal{E}}}_\varphi\, r\,\mathrm{d}r\,\mathrm{d}z = \varepsilon_{r,\mathrm{MUT}} \iint_\Omega \frac{k_0^2}{r^2}\tilde{\vec{E}}_\varphi\tilde{\vec{\mathcal{E}}}_\varphi\, r\,\mathrm{d}r\,\mathrm{d}z, \tag{3.19b}$$

where $\Omega_n \backslash \Omega_{\mathrm{MUT}}$ indicates the whole domain except the MUT. Translated into a resonator problem, the MUT could for example be the central domain, enclosed by the quartz tube of known ε_r and the remaining cavity, where $\varepsilon_r = 1$.

In both cases, the problem is a generalised eigenvalue problem. However, in the eigen-permittivity case the generated matrices are usually not well conditioned and the spectrum of eigenvalues is not *per se* as "clean" as in the eigenfrequency case. This results in a number of results around $\varepsilon_r \approx 1$ and below that value. No systematic investigation was carried out though.

3.2.3. Numerical Analysis and Resonator Design at 30 GHz

The resonator which is the show case for this study is shown in Figure 3.2. It operates at 30 GHz which is also the upper edge of the frequency band of the $\mathrm{LISA_{ES}}$ phase shifter described in the following Chapter 4. It is a cylindrical cavity with an axi-centric

quartz tube filled with LC or any other MUT. The respective nominal dimensions of the resonator are indicated in Table 3.1. The cavity is weakly coupled to an incoming and outgoing waveguide by irises, which will be subject of discussion concerning the problem's symmetry later.

Computational precision, power and memory demand are assessed based on the simple cylindrical cavity shown in Figure 3.3a. The resonance frequencies of the lowest 14 modes are calculated analytically using [Col66, Ch. 6, p. 290]. Then, the FEniCS model and CST Studio Suite (CST) 2015 are used to calculate the resonance frequency numerically with increasing mesh refinement. Analytical and numerical results using the finest mesh in each case agree well as Figure 3.4 illustrates. The relative error is plotted versus the number of meshcells in Figure 3.5. In the same figure, solver time is plotted versus the number of meshcells. Finally, the computational precision, i.e. relative error, is plotted against solvertime in Figure 3.6.

Parameter	h_{cyl}	r_{cyl}	r_{sample}	r_{quartz}	r_{ext}	h_{ext}
Nominal Value (mm)	13.84	3.81	0.25	0.375	0.4	4.0

Table 3.1.: Geometric parameters of the 30 GHz resonator

As expected, the cost of computing a solution is significantly lower when the cylindrical symmetry of the problem is exploited. Both the model size, that is the number of mesh cells (Fig. 3.5) or memory, and the solver time (Figure 3.6) are significantly lower. It should be noted that this is intrinsic to the fact that CST calculates based on a full 3D model of the resonator. The number of mesh cells is therefore obviously larger, as is the number of edges (i. e. interconnects of the mesh). Both effects make the matrices of the problem to be solved both larger and less sparse. The FEniCS model is at this stage not capable of calculating TE_{0xx} modes. However, the experimental data, in particular the mode spectrum in Figure 3.4, shows that it detects all modes obtained analytically [Col66, Sec. 7.55]. Thus, especially for automated optimisation, this approach is intriguing and FEniCS proves to be a useful complement to the full-3D suite CST.

Depending on the application and therefore maximum allowable solver time, a maximum error can be estimated from Figure 3.6. If, for example, the intended application is a measurement setup where the result is expected within seconds, depending on the modes considered, a relative error of less than 1×10^{-4} can be safely attained. While TE modes still show some potential for improvement, relative errors of less than 1×10^{-6} can be attained if only TM modes are of interest.

Before proceeding to the inversion of the problem and determining the MUT's permittivity, the influence of two imperfections that have been neglected until now shall be discussed. Both the filling hole in the top and bottom wall of the resonator as well as the coupling irises deviate from the ideal cylindrical cavity and call for a solution.

The filling holes exhibit cylindrical symmetry as they are located in the axial centres of the top and bottom wall. They are therefore treated by extending the geometrical domain of the FEM problem. The influence on the resonance frequency is assessed by

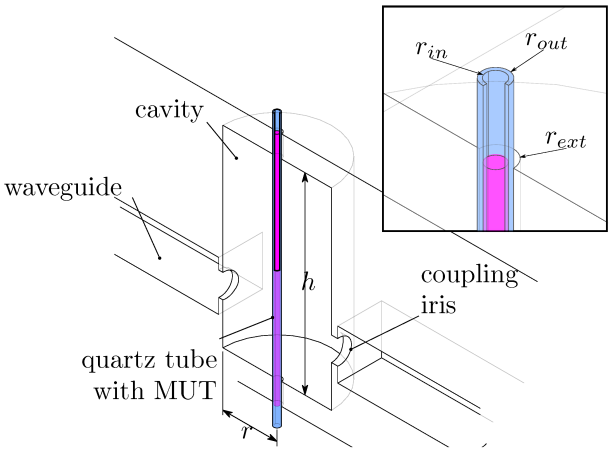

Figure 3.2.: Overview of the 30 GHz resonator geometry

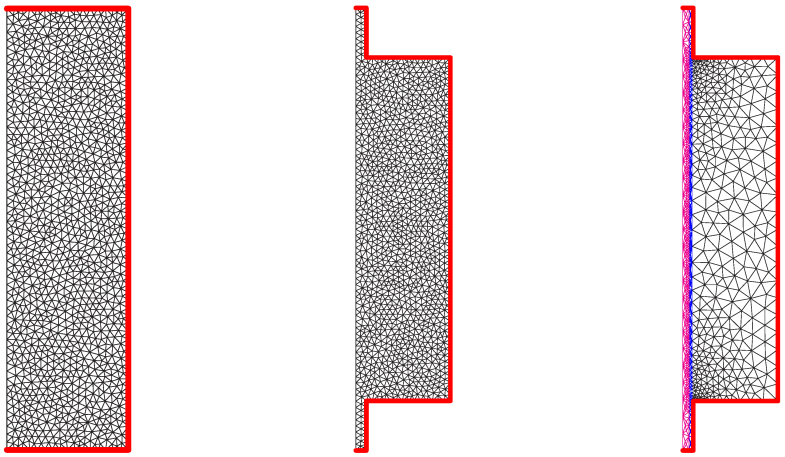

(a) Simple cylinder for analytic comparison

(b) Empty model with filling holes (top and bottom extensions)

(c) Model with domains for tube and MUT

Figure 3.3.: Model versions used throughout the numerical analysis of the FEniCS code. The mesh resolution is variable to best depict the domains, in particular in (c).

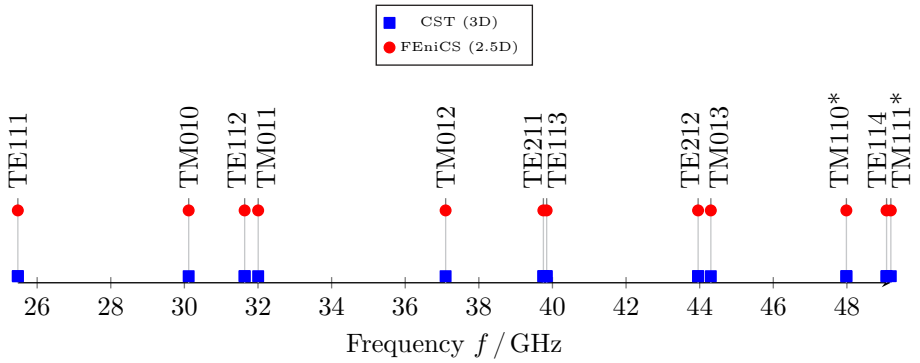

Figure 3.4.: Overview of the eigenfrequency spectrum: resonance frequency is determined analytically (grey lines), using CST (blue squares) and the FEniCS model (red dots). $*$) Degenerate modes.

comparing the 2D FEniCS calculation with a high-resolution CST model. No notable difference was found.

At last, the influence of the coupling irises is approached. The issue is discussed in [Gao92] where analytical expressions for the detuning due to elliptical irises in the wall of a cavity are presented. As the 2.5D FEniCS approach is unable to model this kind of perturbation the results will be compared to results from a high-resolution CST model. As stated in [Gäb15], the detuning is supposedly negligible, as it naturally does not influence the shape of the field in the centre of the cavity. However, it so happens that the irises have significant influence on the results in the 30 GHz resonator discussed here.

The ansatz of Gao [Gao92] is to determine the change in stored energy within the cavity assuming it is adiabatic, i. e. no energy is spilled from the cavity due to the perturbation. As these are coupling holes, this is not exactly true. It can be shown however, that for small irises (weak coupling regime) the spill is negligible. This is sufficiently close approximation for small irises in a weak coupling regime, i. e. for an iris significantly smaller than the wavelength.

Then, the frequency change due to the perturbation by an iris in the wall is described by

$$\omega^2 = \omega_0^2 \left(1 + 2\frac{\Delta W_{\mathrm{el}} - \Delta W_{\mathrm{mag}}}{W_{\mathrm{total}}}\right), \tag{3.20}$$

where W_{total} is the total energy stored in the cavity, ΔW_{el} and ΔW_{mag} are the changes in stored electric and magnetic energy respectively due to the perturbation (and hence

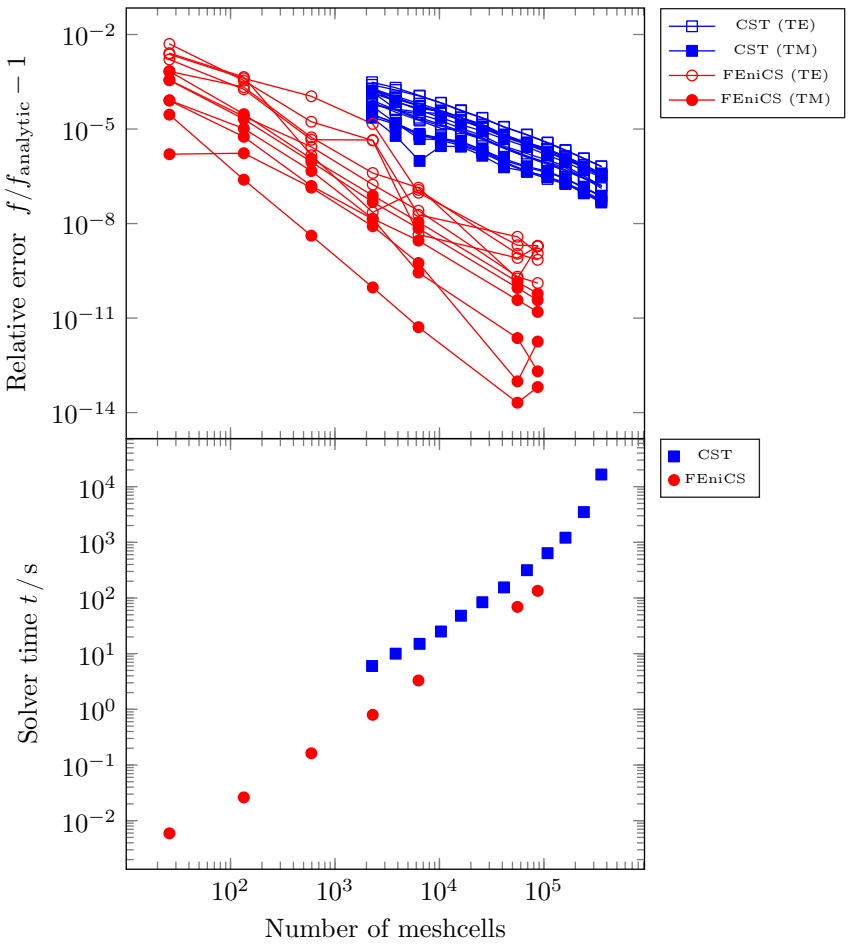

Figure 3.5.: Overview of model performance: error vs. mesh size. The resonance frequency is determined analytically as f_{analytic} and numerically as f using a CST 3D and a FEniCS 2D model of a cylindrical cavity.

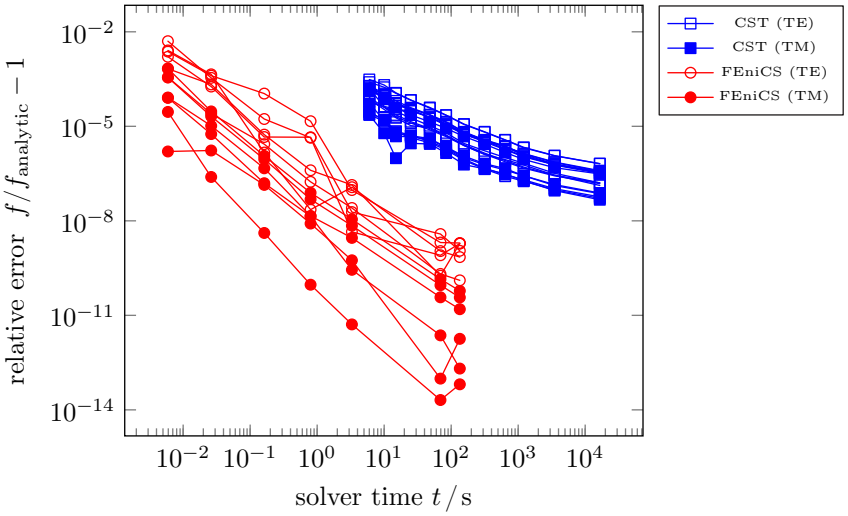

Figure 3.6.: Computational precision versus solver time: when plotted over solver time the advantage of the 2D model over the full 3D model becomes even more apparent.

per perturber). They are defined by

$$\Delta W_{\text{el}} = -\frac{\varepsilon_0}{12} r_{\text{iris}}^3 \left(\frac{|E_0|}{2}\right)^2 \tag{3.21}$$

$$\Delta W_{\text{mag}} = -\frac{\mu_0}{6} r_{\text{iris}}^3 \left[\left(\frac{|H_1|}{2}\right)^2 + \left(\frac{|H_2|}{2}\right)^2\right], \tag{3.22}$$

with normal electric field component $\vec{E}_n = \vec{n} \cdot (\vec{n} \cdot \vec{E})$, where $E_0 = \vec{E}_n \cdot \vec{n}$, tangential magnetic field components $\vec{H}_{1,2}$ corresponding to $\vec{H}_t = -\vec{n} \times \vec{n} \times \vec{H}$ (usually $H_1 = \vec{H}_t \cdot \vec{u}_r$ and $H_2 = \vec{H}_t \cdot \vec{u}_z$), and iris radius r_{iris} [Gao92; Bet44]. For analytic field and energy expressions in cylindrical cavities consult the Mathematical Appendix (cf. (A.55), (A.56), (A.60) or (A.61) respectively), numerical results can be extracted directly from FEniCS.

Using (3.20) the frequency shifts can be calculated. Given TE_{112} for example, the influence of the irises on the mode differ if the electric field is oriented *along* a line from iris to iris or perpendicularly to said line.

With a correction for the irises available, measured results (ω_{res}) can first be corrected (ω'_{res}) and then be used to determine $\varepsilon_{r,\text{MUT}}$ either by means of inverting the direct problem (3.19) or by optimisation of the direct problem.

The inversion of the problem cannot be calculated directly in CST. However, it is easily implemented in FEniCS. As discussed earlier, the eigenvalues of the reformulated

problem (3.19) now correspond to the permittivity of the MUT. The reformulation, on the other hand, degrades the numerical properties of the problem.

3.2.4. Measurement Method and Results

Based on the above considerations, a series of measurements have been carried out. As three components come into play (the bare resonator, the quartz tube and the MUT), three steps are necessary to determine a set of values which are only a priori known by their nominal value. These are listed in Figure 3.7.

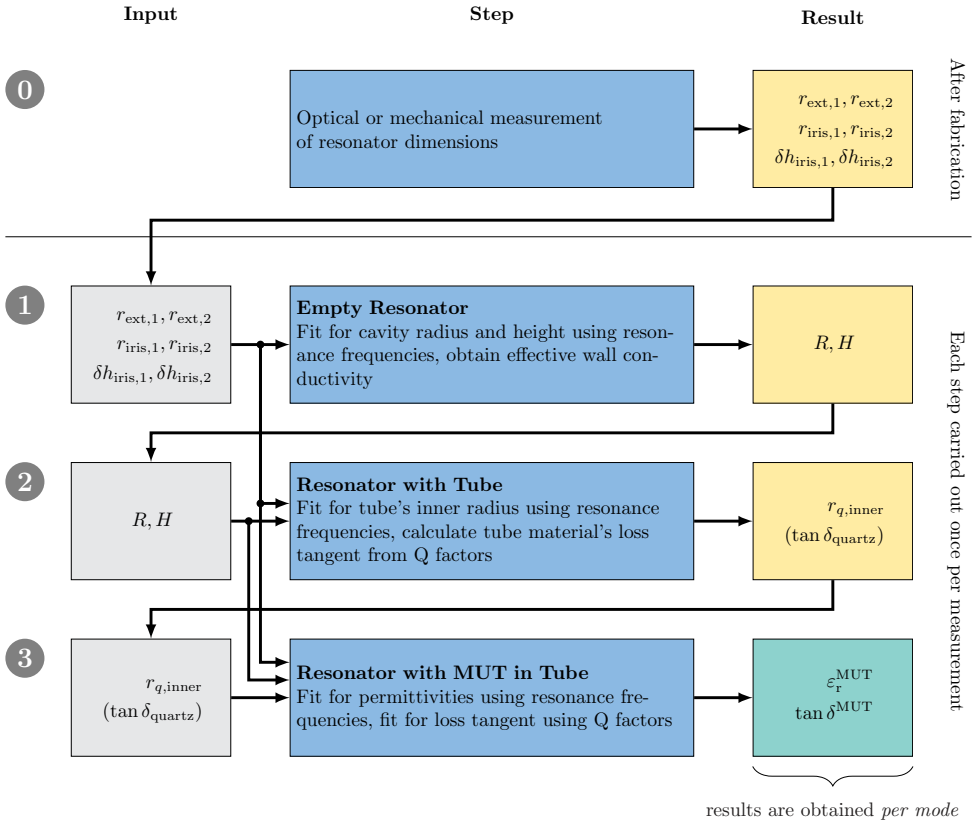

Figure 3.7.: Flow chart of measurement steps and extracted parameters of the characterisation method. In steps 2 and 3 instead of a tube, other carriers like sheets can be used, depending on the geometry file used.

At first, the measurement of the empty resonator is carried out. The band that is swept contains both main resonances and an extra resonance: TM_{010}, TE_{112} and TM_{012}. It may contain further resonances that get shifted beyond the band edge once

the quartz tube is inserted. For these i resonance peaks, once identified by their mode order Tx_{nml}, f_{res} and Q_{res} are determined. Depending on the problem certain modes provide information about specific dimensions: TM_{010} for example is an excellent gauge for the cavity radius. Using the measurement of the empty cavity, radius r_{cav} and height h_{cav} can be determined.

With these parameters set, the second step is to determine the inner radius $r_{\mathrm{q,inner}}$ of the quartz tube. The outer diameter of the tube is determined using a precision micrometer screw gauge or similar devices. There is no obvious way to obtain the inner radius directly from the solution of an EVP. The way proposed here is an iterative optimisation using consecutive solutions of the direct problem with varying $r_{\mathrm{q,inner}}$ in the model.

The third and last step uses a mesh based on the parameters obtained in the previous steps and calculates $\varepsilon_{r,\parallel}$ and $\varepsilon_{r,\perp}$ using the respective resonance modes. It should be noted that $\varepsilon_{r,\parallel}$ and $\varepsilon_{r,\perp}$ are only approximately independent. This is further discussed in Section 3.3.

Based on the resulting $\varepsilon_{r,\parallel}$, $\varepsilon_{r,\perp}$, the Q factors extracted from the measurements and the field solutions obtained in the simulation, $\tan\delta_{\parallel,\perp}$ can be determined directly using the expression (A.54) given in the Mathematical Appendix.

To this end, a resonator has been built according to the analysis results above. It is equipped with a socket to fit into the setup by Gäbler [Gäb15]. Several practical details like a screwhole for attaching temperature sensors are included in the design. Furthermore, it is made from Copper for high Q factor and thermal conductivity. The design is shown in Figure 3.8 with an S-parameter spectrum of the empty resonator.

The flexibility of the method employing FEniCS lies in its ability to change the sample geometry in a very straight-forward way. To demonstrate this, a number of LC mixtures but beyond that also adhesive sheets used in the $\mathrm{LISA}_{\mathrm{ES}}$ project (cf. Chapter 4) have been characterised by a mere change of the geometry file.

The flowchart in Figure 3.7 describes the methodology. In order to account for larger irises, an *effective offset* δh_{iris} is introduced and adaptively determined. A higher-order extension of the theory of Gao [Gao92] can overcome this obviously heuristic solution.

As all measurements include bare quartz tube measurements, the accuracy of the method in terms of permittivity and loss tangent can be studied as outlined in Table 3.2. The permittivity is found to be isotropic at 3.7 for the relevant modes TM_{010} and TE_{112} with a relative standard deviation of $\sigma \approx 1\,\%$, i.e. 3.7 ± 0.037 over 7 samples.

Mode	$\mathbf{TM}_{010}$		$\mathbf{TE}_{112}$		$\mathbf{TM}_{012}$	
f_0	29.0 GHz		31.2 GHz		36.2 GHz	
Result	$\boldsymbol{\varepsilon_r}$	$\boldsymbol{\tan\delta}$	$\boldsymbol{\varepsilon_r}$	$\boldsymbol{\tan\delta}$	$\boldsymbol{\varepsilon_r}$	$\boldsymbol{\tan\delta}$
Average	3.65	2.11×10^{-3}	3.68	12.45×10^{-3}	3.66	0.13×10^{-3}
Std. Dev. (%)	0.70	4.17	0.95	3.36	0.67	14.74

Table 3.2.: Average relative permittivity and loss tangent for a collection of quartz tubes with well-known inner and outer radii

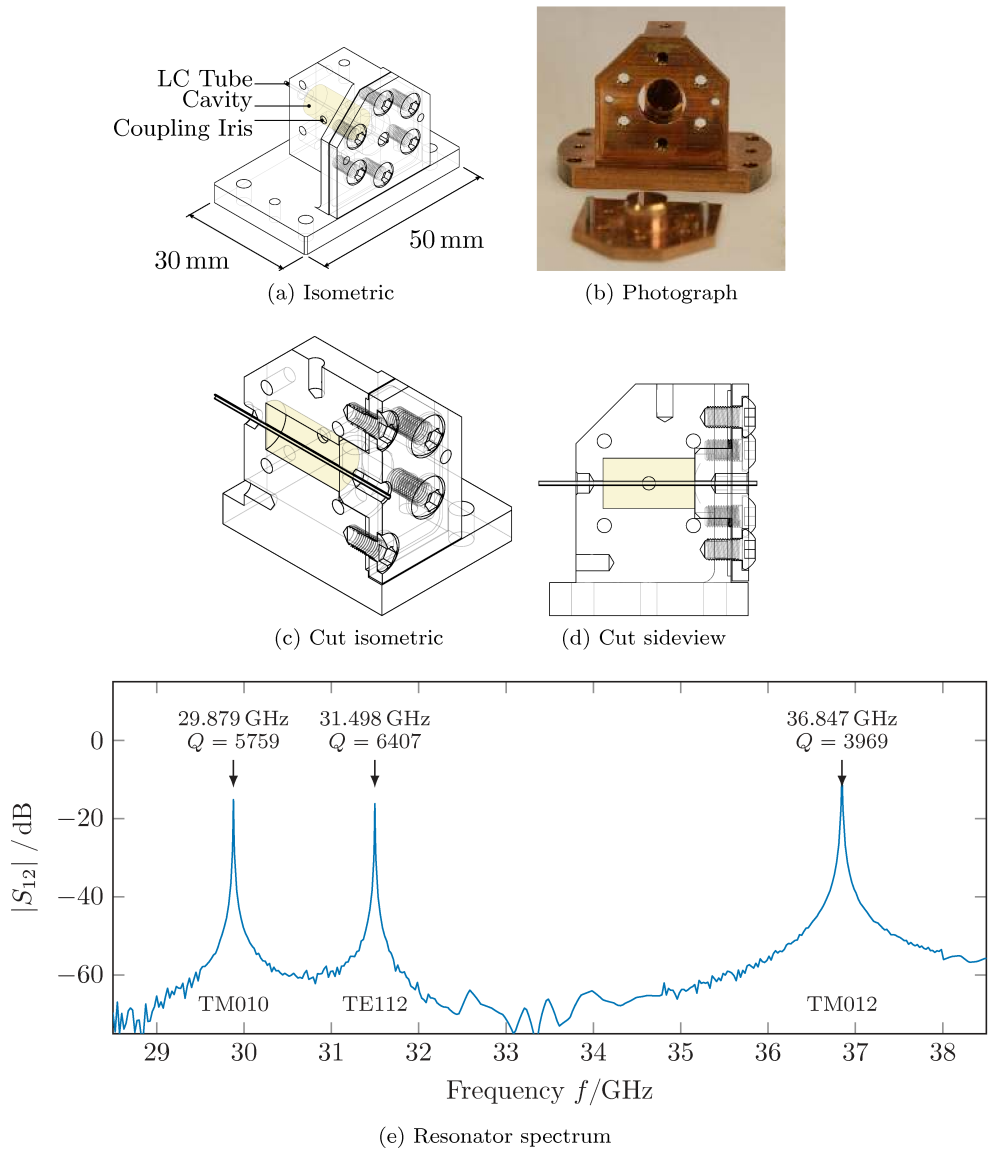

(a) Isometric (b) Photograph

(c) Cut isometric (d) Cut sideview

(e) Resonator spectrum

Figure 3.8.: Technical drawings and photograph of the 30 GHz resonator used for the laboratory study of the numerical parameter extraction approach and empty measurement results with unloaded Q factor. TM_{010} and TE_{112} are used for parameter extraction. TM_{011} is not excited.

A further study of several samples of Zeiss® Harz Kleber 56 shows that larger

loss tangents are accurately determined. Table 3.3 lists the isotropic permittivity between 2.96 and 2.99 with relative standard deviation of $< 0.95\,\%$ and loss tangent at $9.3 \times 10^{-2} \pm 1.1\,\%$.

Mode	$\mathbf{TM}_{010}$		$\mathbf{TE}_{112}$		$\mathbf{TM}_{012}$	
f_0	29.0 GHz		31.2 GHz		36.2 GHz	
Result	$\boldsymbol{\varepsilon_r}$	$\boldsymbol{\tan\delta}$	$\boldsymbol{\varepsilon_r}$	$\boldsymbol{\tan\delta}$	$\boldsymbol{\varepsilon_r}$	$\boldsymbol{\tan\delta}$
Average	2.96	93.85×10^{-3}	2.99	93.67×10^{-3}	2.95	89.32×10^{-3}
Std. Dev. (%)	0.62	1.10	0.95	0.49	0.55	0.95

Table 3.3.: Average relative permittivity and loss tangent for a collection of samples of Zeiss Glue 56 in quartz tubes with well-known inner and outer radii

At last, geometric flexibility is demonstrated in measuring two materials coming in sheet form: silicone coating and adhesive tape used in $\mathrm{LISA}_{\mathrm{ES}}$. While the adhesive tape is applied to the lid of the resonator directly (i.e. no carrier substrate), the silicone coating, being a sprayable thin fluid, is applied to a carrier sheet.

Mode	$\mathbf{TM}_{010}$		$\mathbf{TE}_{112}$		$\mathbf{TM}_{012}$	
f_0	29.0 GHz		31.2 GHz		36.2 GHz	
Result	$\boldsymbol{\varepsilon_r}$	$\boldsymbol{\tan\delta}$	$\boldsymbol{\varepsilon_r}$	$\boldsymbol{\tan\delta}$	$\boldsymbol{\varepsilon_r}$	$\boldsymbol{\tan\delta}$
Average	0.00	1×10^{-4}	0.00	1×10^{-4}	0.00	1×10^{-4}
Std. Dev. (%)	1.00	1.00	1.00	1.00	1.00	1.00

Table 3.4.: Average relative permittivity and loss tangent for a collection of samples of silicone coating and adhesive tape in sheet form

Having checked that the method actually confirms isotropy for allegedly isotropic materials, a number of Merck LCs are characterised and presented in Table 3.5. Where available, earlier 12 or 19 GHz results are included. The names of experimental mixtures are obfuscated.

3.2.5. Discussion

The method presented in this section returns the relative permittivities and loss angles for LCs reliably and with high precision. However, one issue lies with the calculation time: as the EVP is re-built from scratch by the just-in-time compiler in FEniCS, a large amount of time is currently simply wasted. This can be improved by tweaking of the program package.

Also, the number of evaluations of the EVP could be further reduced (currently between 8 and 20 iterations) by computing the slope $\mathrm{d}k_0^2(r_i)/\,\mathrm{d}r_i$ from previous solutions to adapt stepsize and thus converge faster (Newton's algorithm). It would also

Mode	**TM_{010}**		**TE_{112}**		**TM_{012}**	
f_0	29.0 GHz		31.2 GHz		36.2 GHz	
Material	$\varepsilon_{r,\parallel}$	$\tan\delta_\parallel$	$\varepsilon_{r,\perp}$	$\tan\delta_\perp$	$\varepsilon_{r,\parallel}$	$\tan\delta_\parallel$
GT3-23001	3.22	34.95×10^{-3}	2.57	51.06×10^{-3}	3.25	11.86×10^{-3}
GT5-26001	3.27	34.14×10^{-3}	2.51	24.15×10^{-3}	3.30	8.21×10^{-3}
K15	2.97	39.32×10^{-3}	2.85	100.54×10^{-3}	2.96	36.74×10^{-3}
BL035	3.13	80.06×10^{-3}	2.83	68.87×10^{-3}	3.18	23.97×10^{-3}
BL111	3.18	24.51×10^{-3}	2.78	78.10×10^{-3}	3.21	23.77×10^{-3}

Table 3.5.: Parallel (TM) and perpendicular (TE) relative permittivities and loss tangents for a collection of samples of Merck LC in quartz tubes with well-known inner and outer radii

be worthwhile to generalise this by determining an adjoint, e.g. using the package `dolfin-adjoint`.

For higher frequencies it becomes increasingly difficult to determine the above mentioned three parameters independently. Furthermore, a fourth parameter r_{ext} comes into play. As resonator size decreases with increasing frequency, the quartz tube will remain the same size for smaller tubes are both hard to obtain and to handle. It is therefore proposed to use both measurements (Step 1 and Step 2) with at least two in-band resonance modes and an optimising scheme which fits the mode frequencies to the set of parameters $(r_{\text{cav}}, h_{\text{cav}}, r_{\text{q,inner}}, r_{\text{ext}})$. This scheme may take advantage of the fast solving times achieved by expoiting the cylindrical symmetry of the problem. Here, the aforementioned adjoint approach could provide a handy solution.

3.3. The 60 GHz Resonator

In order to design for instance planar 60 GHz antennas, the LC properties need to be known precisely rather than being extrapolated from measurements at e.g. 19 GHz or 30 GHz. To this end, the necessary steps in adapting resonant characterisation of LCs are discussed in this section.

The Q factor of the 30 GHz resonator had already reached a point, where in order for $\tan\delta$ to be determined reliably, the higher-order mode TE_{112} had to be used. For 60 GHz this issue aggravates and higher-order modes need to be used by default to obtain a sufficient Q factor. This is tackled by systematically using higher order modes in order to increase the Q factor.

Using mode TE_{121} instead of TE_{111} can more than triple the Q factor for a large range of aspect ratios $r_{\text{cav}}/h_{\text{cav}}$; see Figure 3.9. Even compared with the TE_{112} used in the 30 GHz resonator this is more than double the Q factor. The same holds for the change from TM_{010} to TM_{020}, which almost doubles the Q factor. However, in terms of resonance frequencies, higher order modes are usually hardly separated from

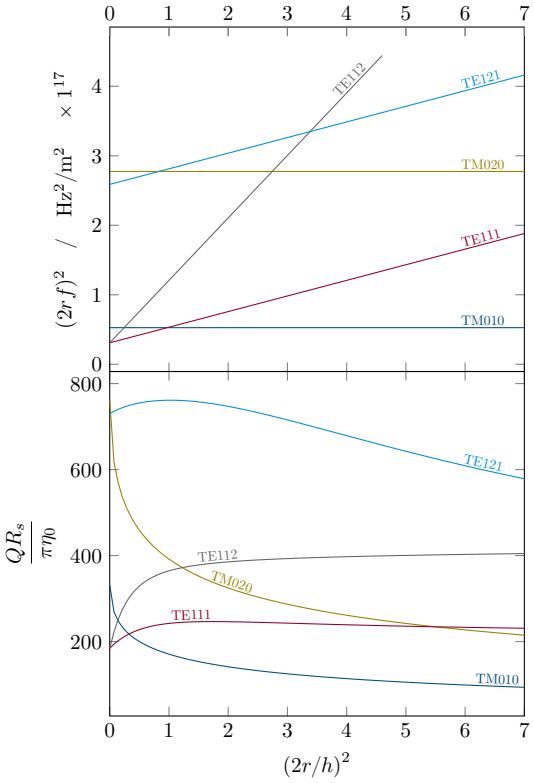

Figure 3.9.: Potential gain in Q factor by switching to higher modes

each other. This issue is clearly visible in Figure 3.1: either the *pillbox* design is chosen (large $r_{\mathrm{cav}}/h_{\mathrm{cav}}$, which provides only mediocre Q factors) or a long *rod*-shaped resonator is chosen which tends to exhibit degenerate pairs of TE/TM modes and is thus hardly suited to characterise anisotropic materials.

To circumvent this problem, new degrees of freedom can be introduced into the design process. In [Sch15] it was shown that by inserting a hollow dielectric cylinder or *tuner* with inner radius $r_{\mathrm{t,in}}$ and outer radius $r_{\mathrm{t,out}}$ into a resonator of aspect ratio $r_{\mathrm{cav}}/h_{\mathrm{cav}} \approx 1.6$, the location of the TE_{111} mode can be shifted towards lower frequencies while those of the adjacent TM modes are largely unaffected.

Parameter	h_{cyl}	r_{cyl}	$r_{\mathrm{t,in}}$	$r_{\mathrm{t,out}}$	r_{sample}	r_{quartz}	r_{ext}
Nominal Value (mm)	2.12	3.65	0.95	2.75	0.25	0.375	0.4

Table 3.6.: Geometric parameters of the 60 GHz resonator as defined in Figure 3.2. Additionally, $r_{\mathrm{t,in}}$ and $r_{\mathrm{t,out}}$ are the tuner's inner and outer radii, respectively.

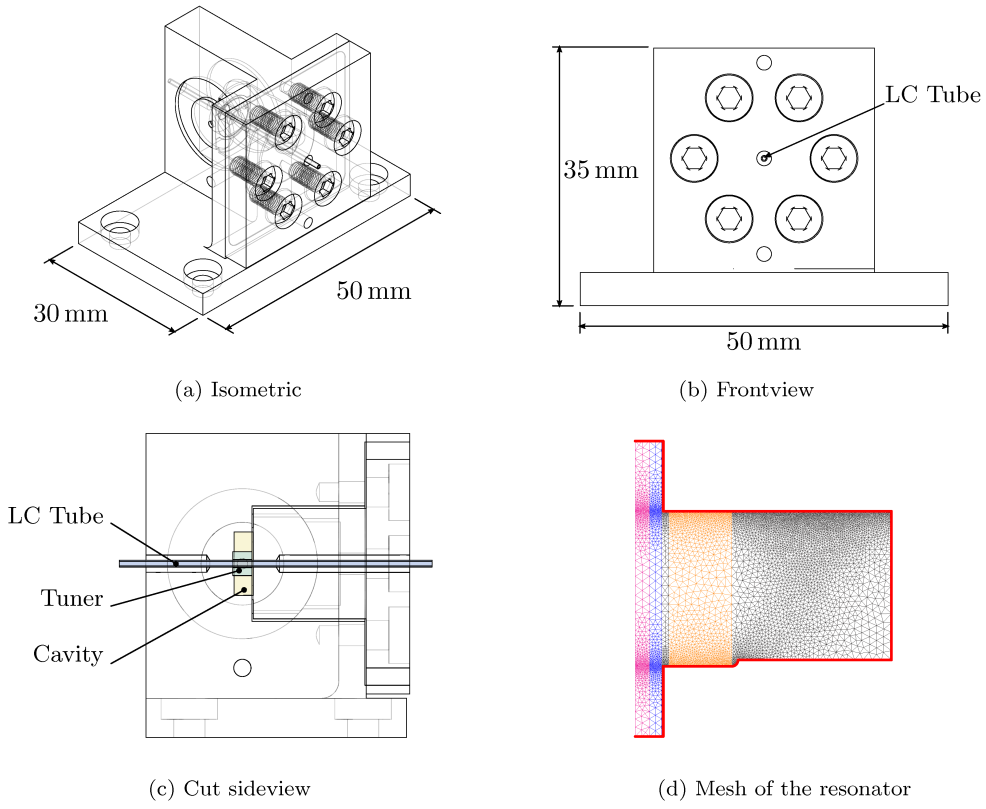

(a) Isometric

(b) Frontview

(c) Cut sideview

(d) Mesh of the resonator

Figure 3.10.: Geometry of the fabricated 60 GHz resonator

Figure 3.10 describes the geometry chosen for the 60 GHz resonator which was implemented. The nominal geometrical dimensions are listed in Table 3.6.

Looking at the field of the TE_{111} obtained numerically in Figure 3.11, one can clearly see that the field in the innermost domain, where the MUT is located, is fairly homogeneously oriented in radial direction (for example Figure 3.11(a)). This even holds for the TE_{121}, where homogeneity is fairly poor at the lid and bottom of the cavity. Nevertheless, the MUT is filled with almost perfectly aligned field. The same holds true for TM modes (Figure 3.12).

However, this is not always the case: the smaller the resonator becomes, the more deformed the field may actually be. This, in turn, makes it difficult to determine $\varepsilon_{r,\parallel}$ and $\varepsilon_{r,\perp}$ independently. Fortunately, this can be solved. The FEM formulation in (3.10) and (3.11) can be modified into a tensor-like form. Then, the permittivity extraction shown in Figure 3.7 is run as a combined problem including two resonance frequencies as inputs obtaining $\left(\varepsilon_{r,\parallel}, \varepsilon_{r,\perp}\right)$ as output in the last measurement step.

Another observation that is visible in the plot of the φ-component of the magnetic field in Figures 3.13 and 3.14 is that the Q factor of TE_{121} will be much higher than

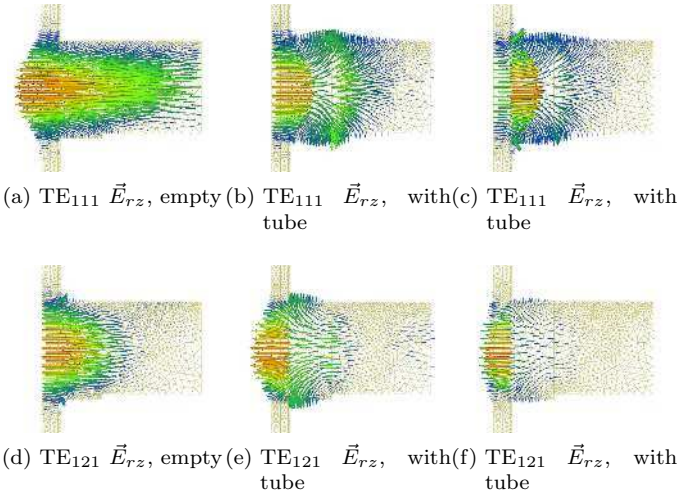

(a) TE_{111} $\vec{E}_{rz}$, empty (b) TE_{111} $\vec{E}_{rz}$, with tube (c) TE_{111} $\vec{E}_{rz}$, with tube

(d) TE_{121} $\vec{E}_{rz}$, empty (e) TE_{121} $\vec{E}_{rz}$, with tube (f) TE_{121} $\vec{E}_{rz}$, with tube

Figure 3.11.: Quiver plots of the rz-components of the electric field in TE_{111} and TE_{121}.

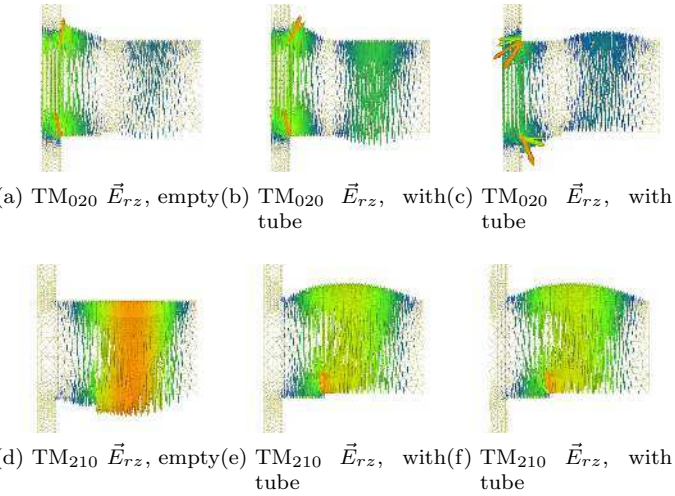

(a) TM_{020} $\vec{E}_{rz}$, empty (b) TM_{020} $\vec{E}_{rz}$, with tube (c) TM_{020} $\vec{E}_{rz}$, with tube

(d) TM_{210} $\vec{E}_{rz}$, empty (e) TM_{210} $\vec{E}_{rz}$, with tube (f) TM_{210} $\vec{E}_{rz}$, with tube

Figure 3.12.: Quiver plots of the rz-components of the electric field in TM_{020} and TM_{210}. The distribution shows why TM_{020} reacts to a MUT while TM_{210} remains mostly unchanged. Colour indicates relative field intensity.

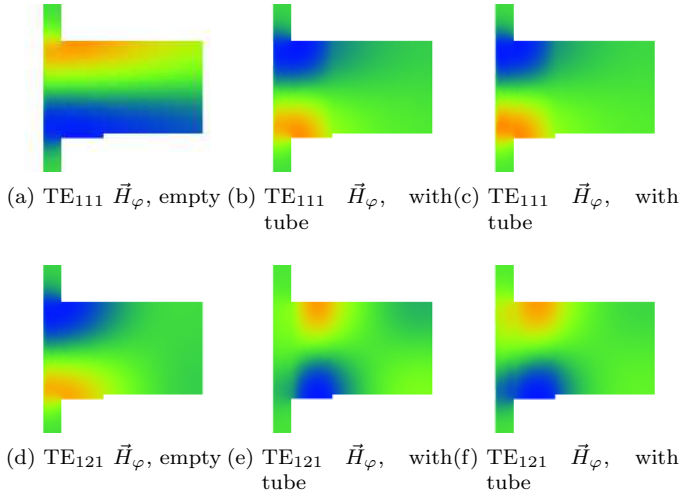

(a) TE_{111} $\vec{H}_\varphi$, empty (b) TE_{111} $\vec{H}_\varphi$, with tube (c) TE_{111} $\vec{H}_\varphi$, with tube

(d) TE_{121} $\vec{H}_\varphi$, empty (e) TE_{121} $\vec{H}_\varphi$, with tube (f) TE_{121} $\vec{H}_\varphi$, with tube

Figure 3.13.: Plots of the φ-components of the magnetic field in TE_{111} and TE_{121}. The prevalence of green ($H_\varphi = 0$) on a large part of the boundary in TE_{121} makes it obvious why the Q factor is so much higher.

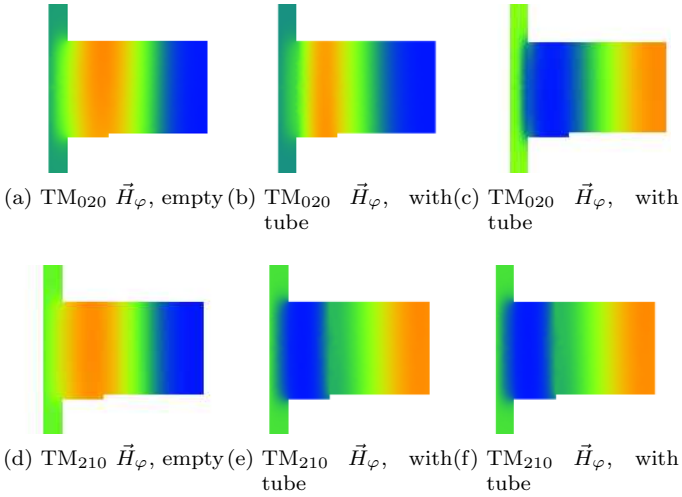

(a) TM_{020} $\vec{H}_\varphi$, empty (b) TM_{020} $\vec{H}_\varphi$, with tube (c) TM_{020} $\vec{H}_\varphi$, with tube

(d) TM_{210} $\vec{H}_\varphi$, empty (e) TM_{210} $\vec{H}_\varphi$, with tube (f) TM_{210} $\vec{H}_\varphi$, with tube

Figure 3.14.: Plots of the φ-components of the magnetic field in TM_{020} and TM_{210}. The Q factors of both modes are comparable.

that of TE_{111}. The green areas indicate low H_φ which is tangential to the boundary. In parts of the boundary adjacent to green areas the induced current will therefore be very low.

As the field distribution changes by inserting a tube (compare rows of subfigures of Figures 3.13 and 3.14) it is clear why the cavity perturbation method will not hold under these conditions. Furthermore, the Q factor may actually increase by inserting a sample—even if the sample is lossy.

Unlike predicted in a CST full-wave time-domain simulation, the coupling of TE_{111} was very weak compared to the TM_{020}. Several attempts were made to overcome this. First, the angle under which the feed waveguides were attached was sweeped and it was found that both modes should show equilibrium at about 60°. However, still at this setting, it was impossible to excite TE_{111} with the 1 mm iris.

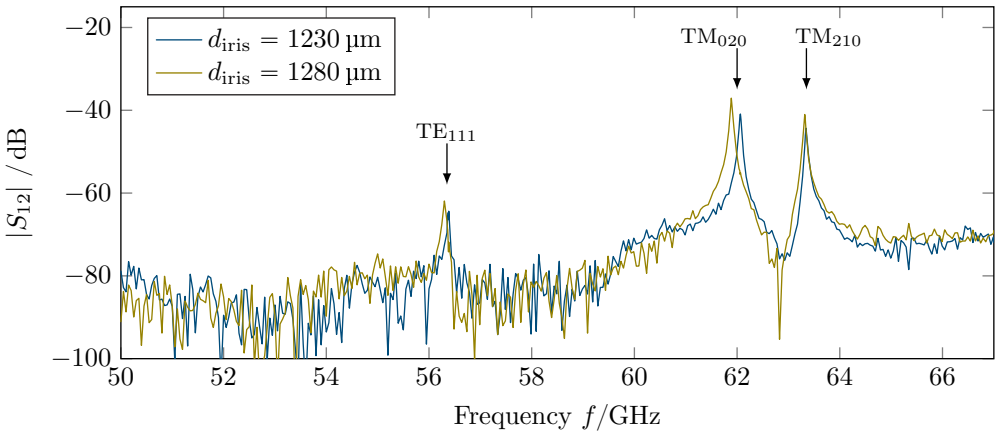

Figure 3.15.: Resonator spectrum in the upper V-band. TE_{111}, TM_{020} and TM_{210} are shown for a resonator with inserted tuner at two different iris diameters. As the coupling of TE_{111} increases, TM_{020} shifts further left, as a result of the larger iris. Measurement data courtesy S. Schmidt

Enlarging the coupling iris, as shown in Figure 3.15, would help in that it coupled the mode strongly enough to get into the dynamic range of the measurements. However, it did detune the TM_{020} significantly and it is safe to say that the iris was large enough to invalidate the assumption of weak coupling and the assumption made by Bethe ($k_0 r_{\text{iris}} \ll 1$, [Bet44]). The product rather is $k_0 r_{\text{iris}} \approx 0.75$ at 60 GHz and with an iris of 1.28 mm in diameter.

Another aspect was that Gao's expressions actually worked great for the TM modes and by just assuming two offset half-magnitude dipoles worked well for the TE_{112}. In the case of the 60 GHz resonator however, an extended approach would have to be derived as the influence of the irises is large. To this end, the induced dipole field used to calculate the detuning could be assumed to be the result of the superposition of several dipoles. For example, the area of the iris could be probed at the centre and

four points on the edge (top, bottom, left and right) – points for which the $\vec{E}_n$ and $\vec{H}_t$ field values can be cheaply obtained from the simulation data. The resulting field will, for simple iris shapes still have dipole-like shape and the energy terms ΔW_{el} and ΔW_{mag} can be calculated easily.

However, the experiment showed that the design needed to be reviewed. The experimental results showed a much lower Q factor than anticipated from the simulations (only about 20 %). This can be attributed to two factors:

- The brass alloy available for these experiments is optimised for machinability and does not exhibit as large a conductivity as assumed in the simulations.
- The surface quality was rather meek and polishing was considered too complicated because of the shape of the cavity bottom as shown in Figure 3.17b.

Considering these two drawbacks, two alternatives where discussed:

- Fabricate the cavity from brass (polish if necessary) and electroplate it with silver[1], thus while possibly increasing surface roughness, obtaining a well defined and much higher surface conductivity.
- Fabricate the cavity from copper, thus while accepting slightly more difficult fabrication allowing for very high surface conductivity, excellent heat conductivity and low surface roughness.

The review is greatly assisted using the FEM approach: the loci of the modes for geometry variations can be very quickly obtained using the FEniCS tool. Figure 3.16 shows an example of how the mode chart is altered when the relative permittivity of the tuner is changed. As a consequence, the same resonator could be used with a different tuner material (replace Rexolite® by glass for example to further separate TE_{111} and TM_{210}). In the same way, a quick look could be taken at a variation of the tuner radii or the cavity aspect ratio, taking into account the tuner or the sample already in the design phase.

It can be concluded that although the resonator design did not yield measurement results for any LC mixtures, the simulation method presented before gives great insight into the design process of more complex resonator geometries. With mode charts at hand, one can speed up the design process by varying geometry, introducing degrees of freedom like the tuner and then picking just the right spot for the characterisation to take place. If the detuning by the irises is properly modeled and given the coupling may remain weak, the set of tools necessary for V-band or even W-band resonators with good Q factors should now be available. Furthermore, the FEM approach using FEniCS allows for further modifications like treating the MUT as an actual anisotropic material, thus potentially enhancing extraction accuracy.

[1] Brass needs a preparation step to close superficial holes and structural defects. Nickel, despite its magnetic properties, was tried to this end but failed to show results. Copper may solve the problem but was not tried for the lack of time and facilities.

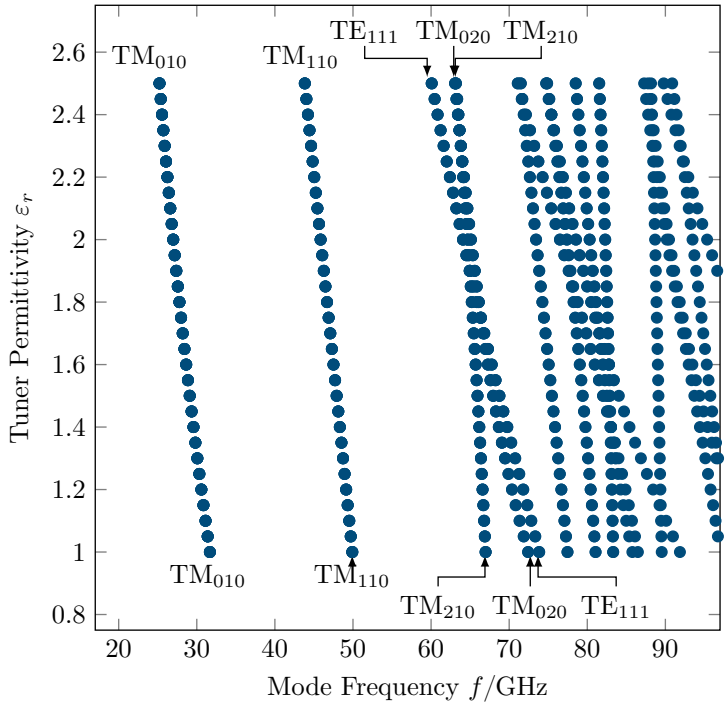

Figure 3.16.: Modechart for the given geometry varying the tuner permittivity up to the value of Rexolite. Clearly visible is the changeover of TE_{111} which starts right of TM_{210} and TM_{020} (bottom) and ends left of the two. Iris detuning is not considered here, so TM_{210} and TM_{020} degenerate. The chart data is obtained within minutes in the 2D approach.

3.4. Terahertz Characterisation

The terahertz region is loosely defined as the range of frequencies between 0.3 and 30 THz. It is confined towards the lower end by the millimetre wave region (mm-wave or EHF, 30 GHz to 300 GHz). At the higher edge there is ambiguity, where it overlaps with the infrared (IR) region and the far infrared (FIR) region which both start at 300 GHz.

A series of publications based on measurements of the permittivity of K15 (the trade name for 4-Cyano-4'-pentylbiphenyl (6CB)) around 2008 sparked the interest in looking at LCs in the THz range more systematically. The first results by Pan et al. and Enikeeva et al. [Pan+03; Eni+07] seemed contradictory and counter-intuitive, as both showed a significant increase of permittivity with frequency without obvious explanation. The frequency range was limited and it was speculated that the increase might be due to the onset of an absorption process outside the measurement range [Vie+12].

Vieweg presented the dielectric properties for eleven commercially available LC mix-

(a) Fabricated resonators, bare brass (background) and Nickel electroplated

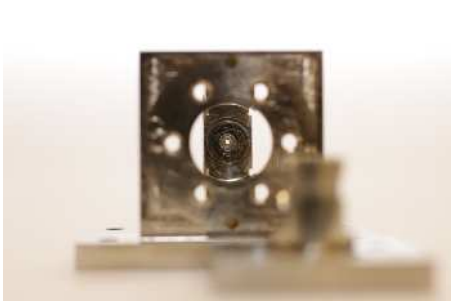

(b) Detail view into resonator cavity

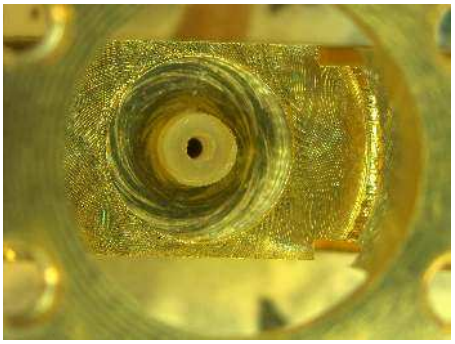

(c) Resonator cavity fit with tuner

Figure 3.17.: Photographs of the 60 GHz resonators fabricated for testing. The overall layout (a) is compatible with the 30 GHz resonator, Nickel electroplating was intended as seed layer for Silver deposition in the cavity. The bottom in (b) shows the filling hole (inner circle), groove for tuner alignment and cavity diameter. The tuner (c) is held in place by the central groove.

tures (amongst which K15) determined by means of the TDS method from 0.3 THz to 2.5 THz [Vie11] and in a later publication the so-called ABCD (*air biased coherent detection*) from 0.3 THz to 30 THz [Vie+12]. Both methods are pulsed measurement techniques.

Soon, results over a wider band [Wil+09] confirmed that the permittivity increase must have in fact been an error. Further work by the same group over an even wider frequency range [Vie+12] showed no indication of an absorption process whatsoever.

Therefore, the focus of this work was shifted to study a specific set of LCs unavailable to most other groups: the Merck mixtures previously used for microwave and millimetre wave applications. It could be shown in that range, that functioning tunable LC devices were possible. So the motivation was to learn more about the properties of these materials in the THz range. Various switches or adaptive optical elements had

been proposed in this context. In this work, the scope is limited to characterisation and possible devices will only be discussed in the conclusions and outlook part.

At Prof. R. A. Lewis' laboratory at University of Wollongong, New South Wales, Australia (UoW) it was possible to use both a ZOmega Terahertz Inc. Z-3 TDS setup and an Fourier Transform Interferometer which offered a frequency range of approximately 2 THz to 8 THz and curiosity was sparked to look at this range too.

In this work, the aforementioned TDS and the FTIR were employed in order to obtain a broadband insight into a number of Merck LC blends. The methods' basic setup and working principles are presented below as an introduction. Further on, the experimental setups are discussed. The concluding discussion of the results and a brief comparison of all methods are given.

3.4.1. Time-Domain Spectroscopy

In TDS, the THz spectrum is generated by ultra-short pulses (pulse durations in the range of ps) which are created in an Auston switch [ACS84], using the fast, non-linear response of a semiconductor to illumination by a pulsed laser (pulse durations in the range of fs). On the receiver side, the signal is analysed by either another Auston switch or by a non-linear device, the optical rectifier (often ZnTe) where the THz pulse is superimposed with the source laser pulse at a given time offset. Commonly, this detection method is simply referred to as optical rectification.

Sweeping the time offset over a large amount of pulses yields a set of samples which represents the pulse shape (an average to be precise but within the margin of repetition error). This pulse representation in time-domain is then transformed numerically into frequency domain and the spectrum is obtained. A schematic of the setup used for the present measurements is shown in Figure 3.18.

The TDS system consists of a femtosecond-pulsed laser creating rapid charge separation on an emitter. In this case, a low-temperature grown Gallium-Arsenide (LT-GaAs) emitter is used. The charges separated by the electric field of the laser pulse create an electric pulse that is coupled to an antenna. The pulse bandwidth can be several THz depending on the setup. The THz pulse propagates through the sample and is focussed on the ZnTe detector where the incoming portion of the original laser pulse is modulated depending on the THz pulse's intensity. A delay stage is used to delay this part of the original laser pulse in order to sample the THz pulses at different instants.

Such systems offer bandwidths of up to 5 THz [ZOm; Vie+14] depending on the system design, i. e. switch and rectifier. The ABCD method, for instance, used by Vieweg et al. uses an air plasma as rectifier and obtains a much larger bandwidth (up to 40 THz in [Vie+12]). The resulting pulse shape contains both a time delay and an attenuation due to the sample. Therefore, the Fourier transformed spectrum contains both magnitude and phase. An extraction of complex permittivity is therefore possible within the system's dynamic range.

On the other hand, the frequency resolution of TDS systems depends on the maximum time offset over which the pulse is sampled. High frequency resolution is therefore only possible at the expense of measurement duration. This last point was considered a minor drawback since all possible signatures of LCs in the THz range were

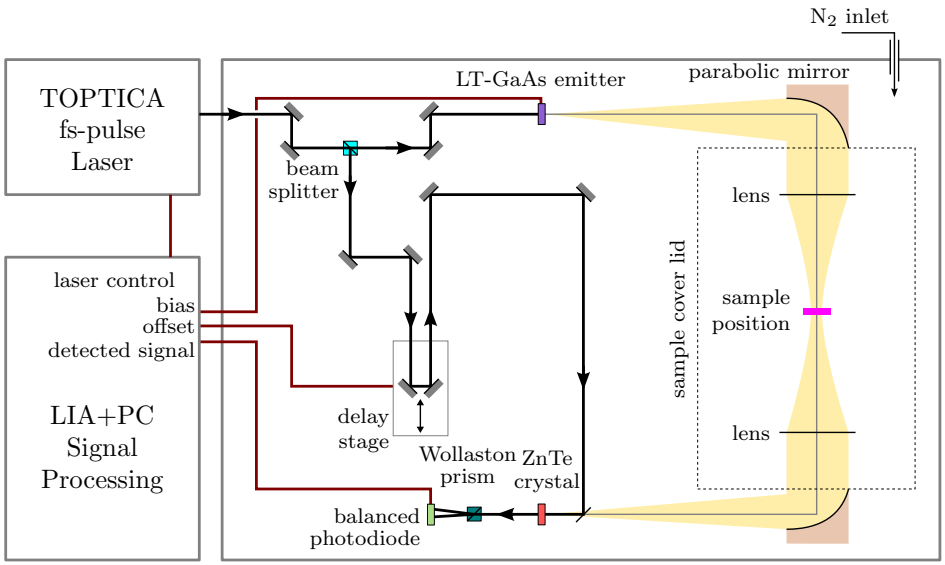

Figure 3.18.: Schematic setup of a TDS system (ZOmega Z-3 at UoW)

considered wideband. This is a fair assumption because resonances in liquids in the IR and THz range are usually strongly coupled and unlike in solids or gases exhibit bandwidths of typically at least several percent.

3.4.2. Fourier-Transform Interferometry

In an FTIR a quasi-white, band-limited light source provides two beams (the "arms" of the interferometer, Figure 3.19): one traverses a fixed length path, the other a path of variable length. Both beams are superimposed and sent through a sample before arriving at the detector. In doing so and in recording the overall intensity at the detector over path length offset d of the second arm, a so-called "interferogram" is obtained. The intensity at the detector is given by

$$I(d) = \int_0^\infty \left| \frac{1}{2} E(\omega) \cdot \left(1 + e^{j\frac{\omega}{c_0}d}\right) \right|^2 \mathrm{d}\omega = \frac{1}{2} \int_0^\infty |E(\omega)|^2 \cdot \left(1 + \cos\frac{\omega d}{c_0}\right) \mathrm{d}\omega. \tag{3.23}$$

The first summand is just half the total spectral power of the source which accounts for a constant offset. The second part, however, has the form of a *cosine transformation*. Similarly to a Fourier transform, the interferogram and the intensity spectrum are transforms of one another. The transformation still holds, if $E(\omega)$ is band-limited, e. g. by filters.

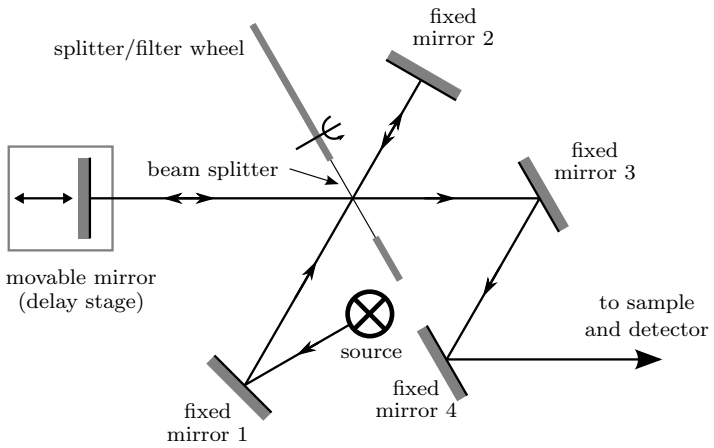

(a) Schematic Beam Line

(b) Photograph

Figure 3.19.: Schematic setup of the Polytec FTIR and photo of the instrument at UoW

FTIR interferometers were most commonly used in the field of IR spectroscopy. The device at UoW, used in the presented measurements, is modified to fit the THz range and cover frequencies from 2 THz to 8 THz approximately.

The same limitations in terms of frequency resolution as for the TDS systems hold for FTIR systems. Furthermore, it can be seen from (3.23) that only the intensity is recorded and therefore phase information is lost. This can be circumvented by placing the sample in one of the arms. However, this breaks the simple transform relation. This approach was suggested by Chamberlain, Gibbs and Gebbie [CGG69], but the FTIR instrument at UoW could not be modified to implement this setup. Therefore,

in these results only the transmissivity or absorption was obtained, respectively.

3.4.3. Experimental Setup

In both cases, TDS and FTIR, the transmission of a THz beam through the sample is used to extract the material properties. The measurements are thus non-resonant. Two sample cells were designed to this end. One made from polymethylpentene (TPX) has a window of 20 mm diameter. The second, a metallic holder with polypropylene (PP) windows, has a 40 mm window. Both are combined with an assembly of two magnets which ensures homogeneous LC alignment without the need of an external voltage source.

TPX Cell TPX offers very good THz transparency, a low permittivity and a low gas permeability. Its mechanical properties are good, it is of high tensile strength and therefore solid and offers good mechanical handling. The only drawback is its brittle texture, which makes it harder to process than other polymers. The cell fabricated at UoW is shown in Figure 3.20. It encloses a cavity for the MUT of 1 mm thickness and 20 mm diameter, which is acceptable for narrow beam or in-focus measurements. All measurements with this cell were carried out near or in-focus.

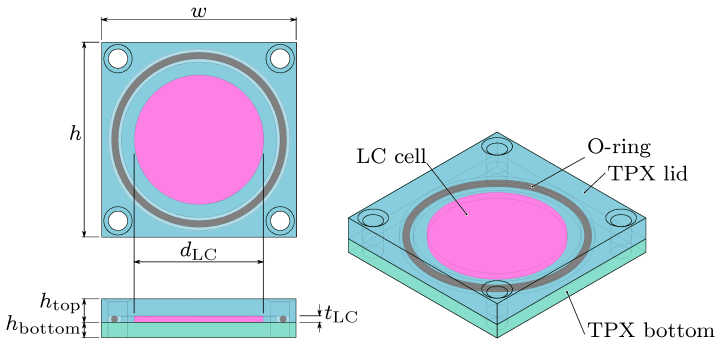

(a) Front and Side View (b) Orthographic Projection

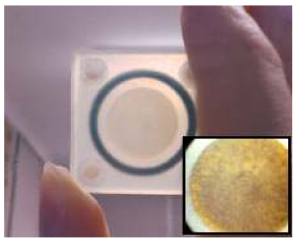

(c) Photograph

Figure 3.20.: Sample Cell made from TPX with $d_{LC} = 20\,mm$, $t_{LC} = 1\,mm$, $h_{top} = 3.65\,mm$, $h_{bottom} = 2.35\,mm$ and $w = h = 30\,mm$.

The material itself was characterised as a reference with other publications and for proper parameter extraction. It is listed in the results section.

PP Cell PP is used for the second sample cell. It has slightly higher permittivity and slightly lower transparency than TPX. However, TPX is prohibitively expensive and PP offers almost the same properties at a fraction of the price (see data in Figure 3.23 on page 51). The cell consists of two identical aluminium covers, two identical PP window plates, one inner and one outer stainless steel ring as spacers and a rubber gasket ring. All parts are assembled, aligned and held by four screws. The MUT is filled through the side using a syringe. The assembly is shown in Figure 3.21.

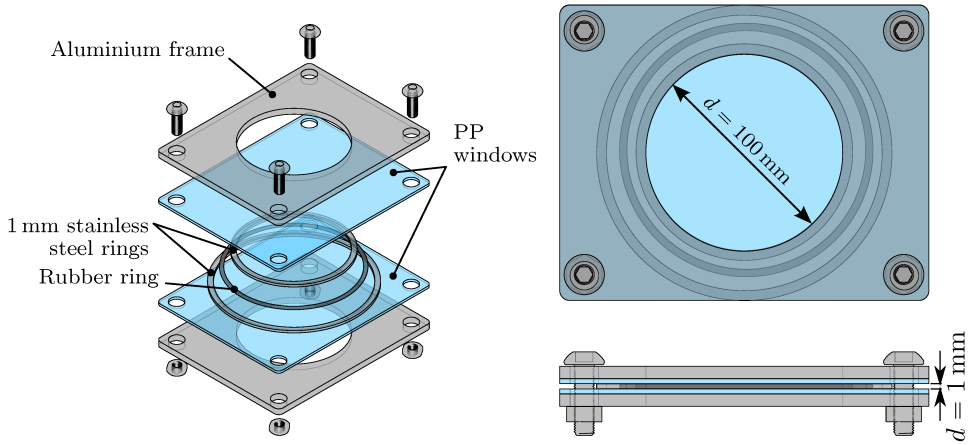

(a) Orthographic Projection (b) Front and Side View

Figure 3.21.: Schema of the sample cell. The MUT is held between the PP windows and the rubber ring. Filling is done using a syringe inserted from the sides. The holder is oriented such that the propagation direction of the Terahertz beam is perpendicular to and centered on the windows.

For each cell (TPX and PP) there is a matching magnet holder of the kind depicted in Figure 3.22. Both consist of two permanent magnets held at an appropriate distance by spacers and providing a constant, homogeneous magnetic field of approximately 0.1 T to 0.2 T which is sufficient to orient the LC in due time.

The cells are placed in the respective setups at the sample positions indicated in Figures 3.18 and 3.19. Note that the position in the FTIR in Figure 3.19 only allows for the determination of the absorption, not of the permittivity.

3.4.4. Measurement Results

The measurements yielded results for various LC mixtures. They were processed numerically in order to extract permittivity and loss data. The TDS data contains

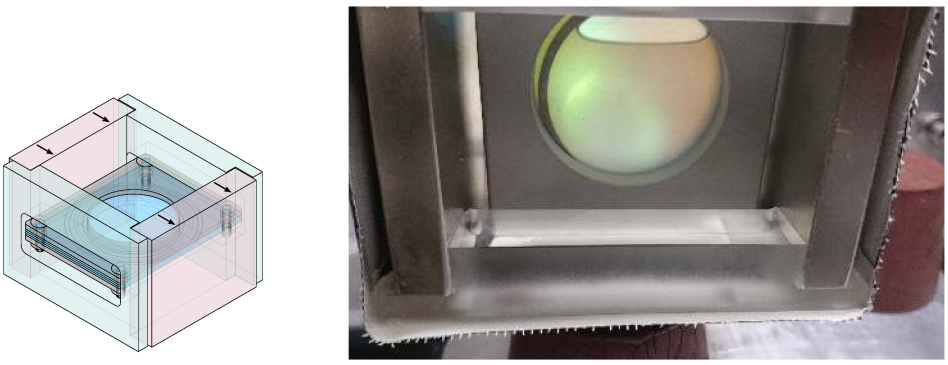

(a) Orthographic Projection (b) Photograph

Figure 3.22.: Schema and photograph of the holder with biasing magnets. The arrows in (a) indicate the orientation of the permanent magnets. Magnetic field is always aligned horizontally. The Terahertz beam polarisation is changed in order to get parallel and perpendicular readings.

both phase and magnitude, so a full set of ε_r and $\tan\delta$ can be obtained. While the initial plan was to use the FTIR in a modified layout to also obtain information on phase, it turned out to be impractical with the small amount of space. Therefore, the recorded data contained only magnitude and conclusions can only be drawn on the dielectric losses using the permittivity data from the TDS measurements.

Parameter Extraction

In the case of the TDS each sampled THz-pulse is first transformed using Fast Fourier-Transform (FFT) to obtain the spectrum of the pulse. Each sample spectrum S_{sample} is paired with an empty reference spectrum $S_{\text{ref}}(\omega)$ of the holder.

In order to obtain a normalised spectrum magnitude, the magnitude of the sample spectrum is divided by that of the reference spectrum. The phase delay introduced by the sample is calculated by first unwrapping the phase of sample and reference spectrum. Free-space propagation is assumed, so the phase-frequency relation is linear and at $\omega = 0$ the phases must naturally be zero. The unwrapped data is fit to an offset linear function, the offset subtracted and the thusly corrected phase data are substracted from each other yielding the phase difference.

This yields a first approximation for the transmission magnitude and phase of the sample. Obviously, this approach ignores resonances in the sample holder which in fact occur as Fabry-Pérot resonances. In order to model these, the work of Duvillaret, Garet and Coutaz was used to obtain the complex refractive index as a result of minimising the difference between an analytic transfer function $T(\omega)$ and the measured

transmission $T_{\text{meas}}(\omega)$ [DGC96], as

$$T(\omega) = \frac{S_{\text{sample}}(\omega)}{S_{\text{ref}}(\omega)} = \frac{2n_{\text{s}}(n_1+n_3)}{(n_{\text{s}}+n_1)(n_{\text{s}}+n_3)} \cdot \exp\left(-i(n_{\text{s}}-n_{\text{air}})\frac{\omega L}{c_0}\right) \cdot \text{FP}(\omega) \quad (3.24)$$

$$\text{with} \quad \text{FP}(\omega) = \left[1 - \left(\frac{n_{\text{s}}-n_1}{n_{\text{s}}+n_1}\right)\left(\frac{n_{\text{s}}-n_3}{n_{\text{s}}+n_3}\right) \cdot \exp\left(-i2n_{\text{s}}\frac{\omega L}{c_0}\right)\right]^{-1}, \quad (3.25)$$

where n_1 and n_3 are the refractive indices of the sample cell windows, n_{s} is the refractive index of the sample and L is the sample cell thickness.

As the samples are optically thick, ambiguity is introduced causing the algorithm to not always converge. If it does, the real part of the refractive index matches well with the one obtained by means of the extracted phase delay. Therefore, the presented data for the refractive index is actually taken directly from the phase difference data.

In the case of the FTIR measurements, no phase information was available. The interferograms of sample and reference measurements were cosine-transformed as described in (3.23). Then, the normalised transmission spectrum is obtained by dividing sample spectrum by reference spectrum.

Using information about the permittivity obtained from the TDS data, $\tan\delta$ is estimated as described below in Section 3.4.4.

TDS Results

First, the validity of the extraction algorithm is tested against two known materials: TPX, the window material in the first measurement campaign. It is cited to have $n = 1.46...1.49$ or $\varepsilon_r = 2.13...2.22$ in the terahertz range [BDL81; Tyd]. In the second campaign PP was used. It shows almost identical refractive index as TPX with $n = 1.49$ or $\varepsilon_r = 2.22$ and slightly higher loss angle [BDL81]. The results shown in Figure 3.23 match well with both optical and terahertz data from various sources.

Using holder 1, four GT3-series materials were characterised and the results were published in [Wei+13b]. Figure 3.24 holds the results. As can clearly be seen, the variations between the materials are relatively small. It should be noted though that the TDS method does not provide the same accuracy as a resonator based method, in particular for the loss angle. The interaction with the MUT is strongly enhanced by the resonance effect. In this non-resonant setup the interaction is limited to the thickness of the sample.

The tendency for $\varepsilon_{r,\parallel}$ of GT3-25003 (Figure 3.24d) is caused by a glitch in the numerical extraction method and becomes less important for higher frequencies.

The second campaign looked at two GT mixtures with high anisotropy and low losses, GT3-18017 and GT5-28004. While GT5-28004 exhibits extremely low loss in the microwave and mm-wave range, the parallel orientation shows a clear rise in losses from around 750 GHz. It is unclear why this happens, but it can be attributed to the material.

The two experimental mixtures Merck-521 and Merck-893 show slightly lower anisotropy and very similar loss values in both orientations. The mixtures are supposed to exhibit a larger anisotropy [personal communication]. The most likely reason is that

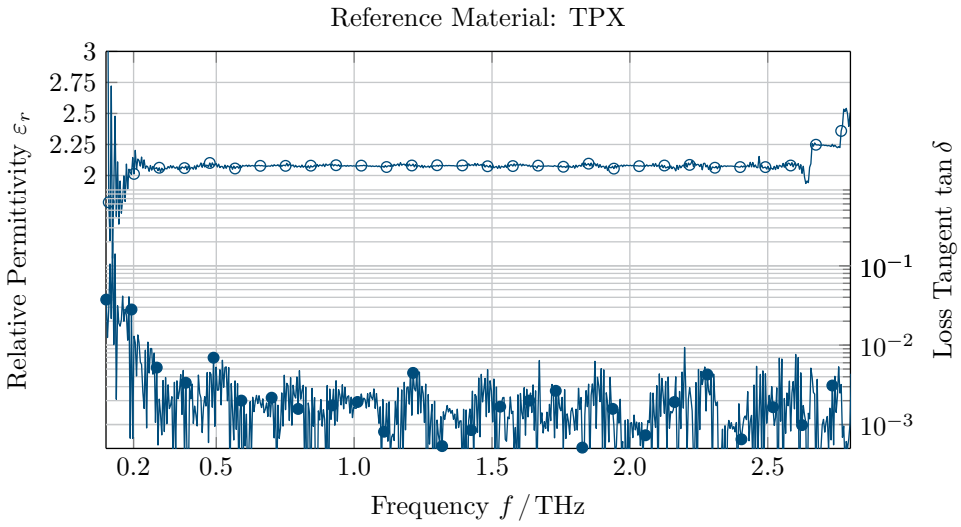

(a) TPX

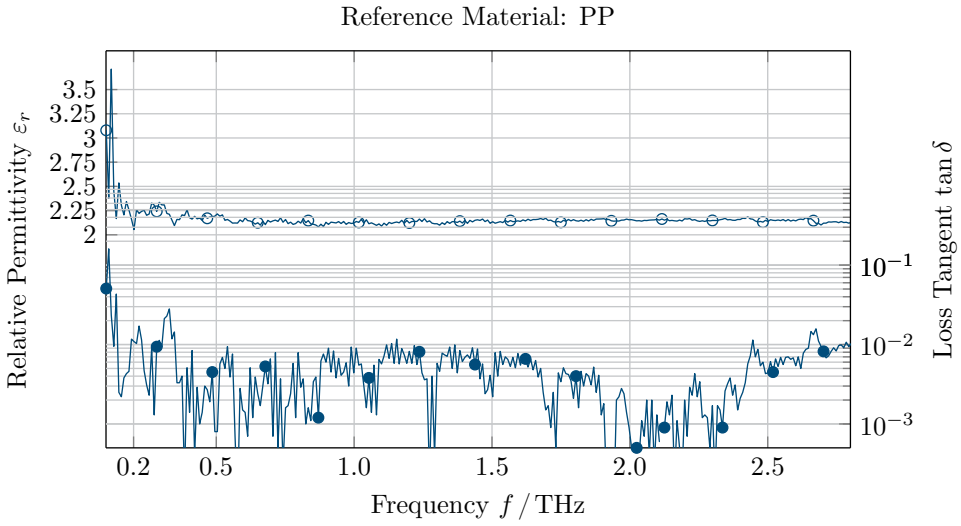

(b) PP

Figure 3.23.: Window material used for the measurements. TPX was used in the first campaign for TDS only. The larger windows of the second setup required more material, hence PP was used.

the material was not fully oriented at the time of the parallel measurement. Especially Merck-521 is an extremely viscous substance.

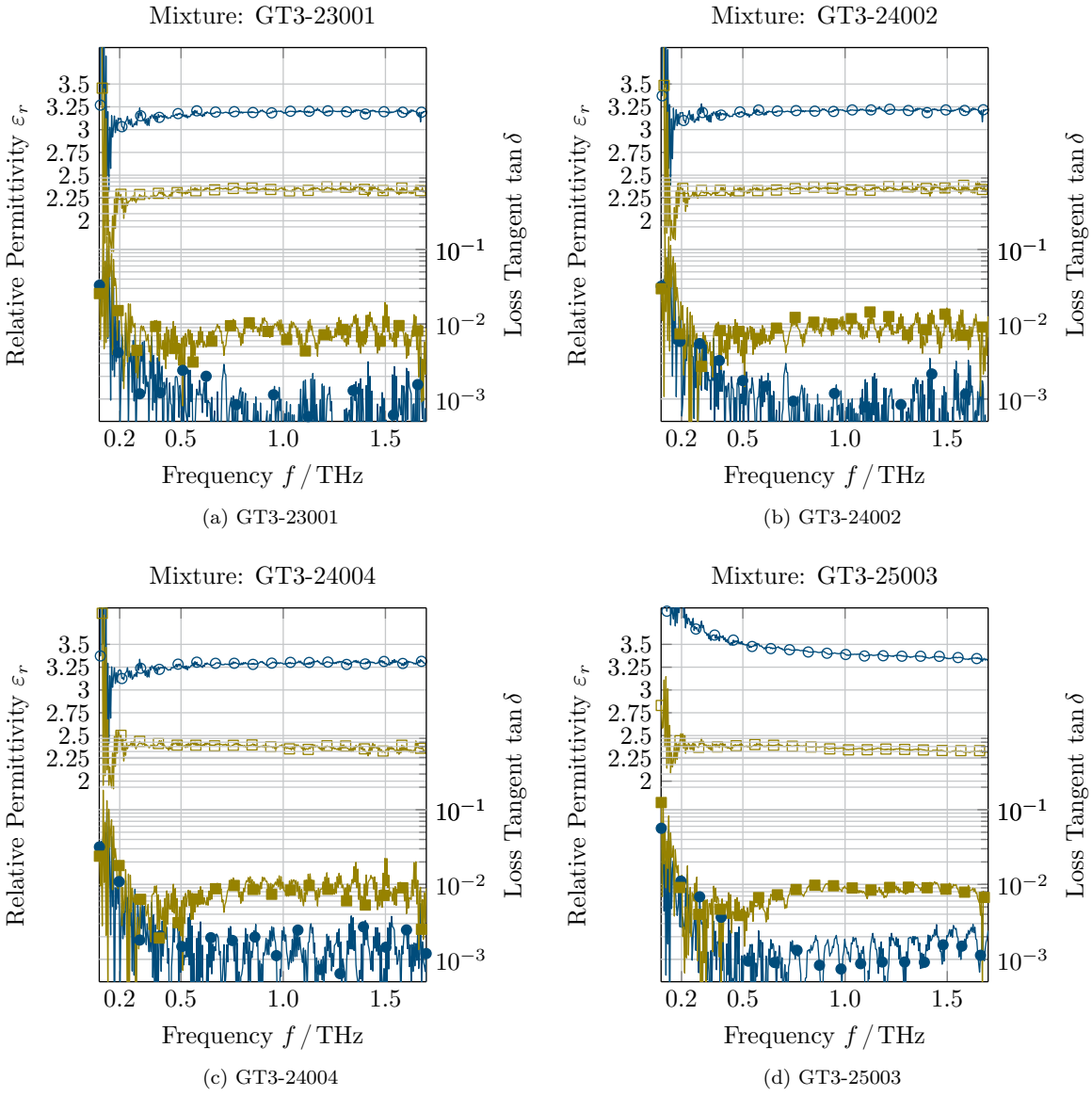

(a) GT3-23001

(b) GT3-24002

(c) GT3-24004

(d) GT3-25003

Figure 3.24.: Material parameters for various GT3-series mixtures. $\varepsilon_{r,\parallel}$, $\varepsilon_{r,\perp}$, $\tan\delta_\parallel$ and $\tan\delta_\perp$. Relative permittivity and loss are very similar. Variations occur mainly by numerical glitches of the extraction algorithm (increasing ε_r at low frequencies can be attributed to this).

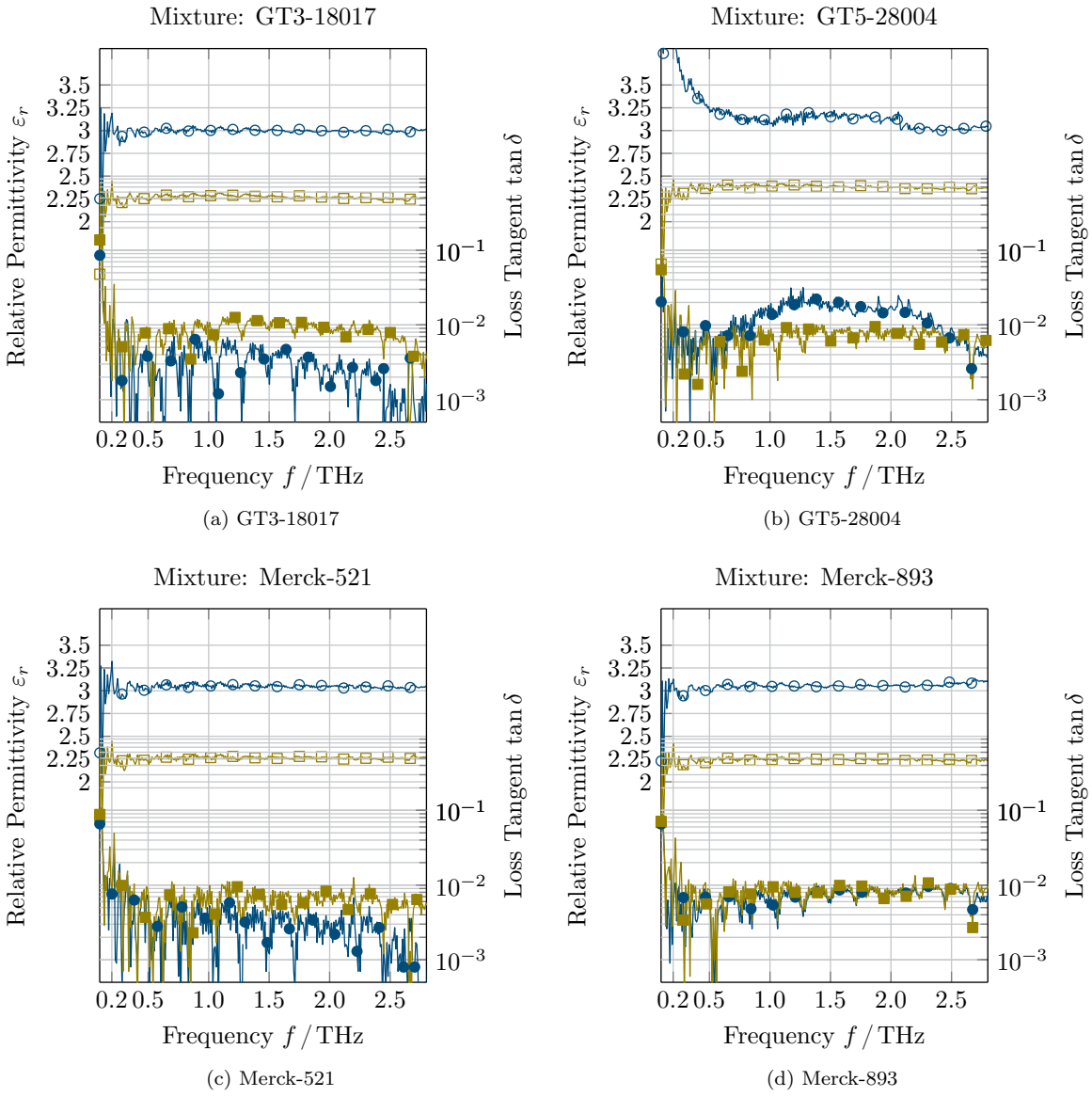

(a) GT3-18017

(b) GT5-28004

(c) Merck-521

(d) Merck-893

Figure 3.25.: High-performance GT3 and GT5 mixtures compared with two experimental materials (TDS). The spread in anisotropy is clearly visible between materials. The anisotropy in $\tan\delta$ is less pronounced than expected. The data quality may be questionable. $\varepsilon_{r,\parallel}$, $\varepsilon_{r,\perp}$, $\tan\delta_\parallel$ and $\tan\delta_\perp$.

FTIR Results

As mentioned before, the FTIR measurements only yield transmission values $T = I(d)/I_0 = e^{-\alpha d}$. Using the dielectric properties ε_r previously determined in the TDS measurements of the LC mixtures, the loss tangent can be calculated as

$$\tan\delta = \frac{2n\kappa}{n^2 - \kappa^2} \tag{3.26}$$

$$\text{with} \quad \kappa \approx \frac{\alpha c_0}{2\omega}, \quad \alpha = -\frac{1}{d}\ln T \quad \text{and} \quad n \approx \sqrt{\varepsilon_{r,\mathrm{TDS}} - \kappa^2} \tag{3.27}$$

First, for each measurement, a beam splitter or "filter" is selected (see Figure 3.19). This is important as different filters have different transmission bands. Figure 3.26 shows the passbands of the three filters relevant to the measurement campaign. The intensity is chosen purely arbitrarily but with the same light source and same sensitivity settings at the detector. The assumption is that an acceptable SNR is achieved where the intensity is higher than 0.5 for both polarisations which is shown by the dashed line.

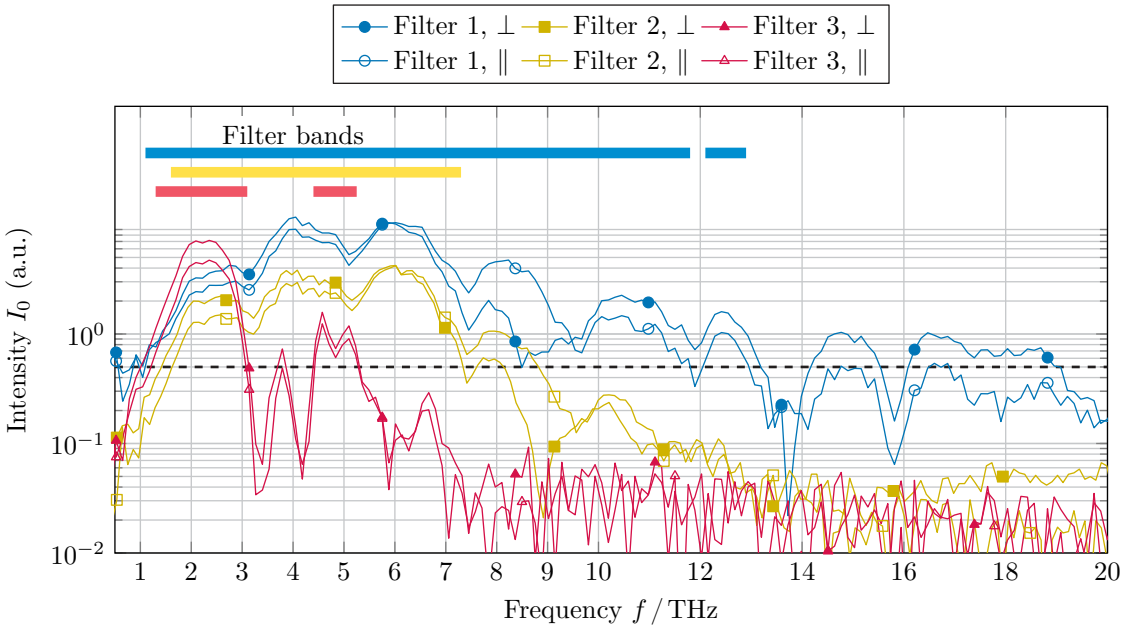

Figure 3.26.: FTIR Filter Sensitivity

The filter used by default is "Filter 2" (yellow). It covers the band from 1.6 THz to 7.3 THz with a good suppression otherwise. In some cases, Filters 1 and 3 are used. "Filter 1" (blue) offers more light and a wider band (ca. 1.1 THz to 12 THz) but at the expense of lower suppression at higher frequencies which degrades the SNR. "Filter 3"

(red) on the other hand provides good dynamic range on the low edge but practically cuts off at 3 THz. The employed filter and range is denoted in every plot by a coloured bar indicating the range.

With the LC GT3-18017 it was hard to obtain enough light with Filter 2. However, the results with the other two filters show good agreement below 3 THz and the tendency to have $\tan\delta_\perp < \tan\delta_\parallel$ towards 5 THz visible in Figure 3.27a can be noticed in Figure 3.27b as well.

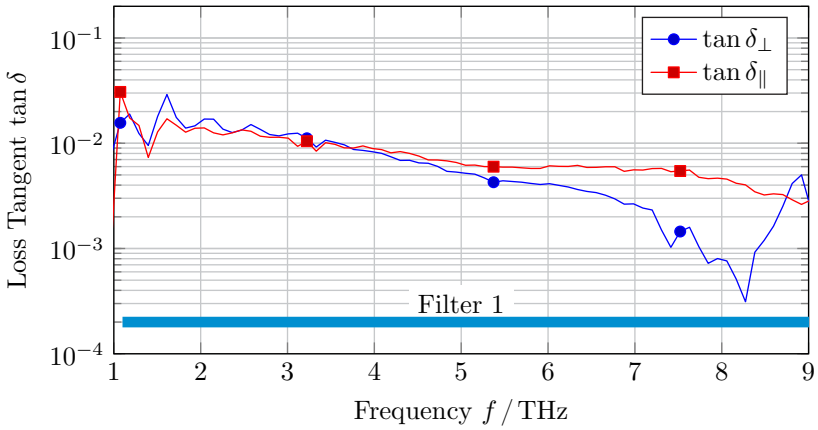

(a) Filter 1

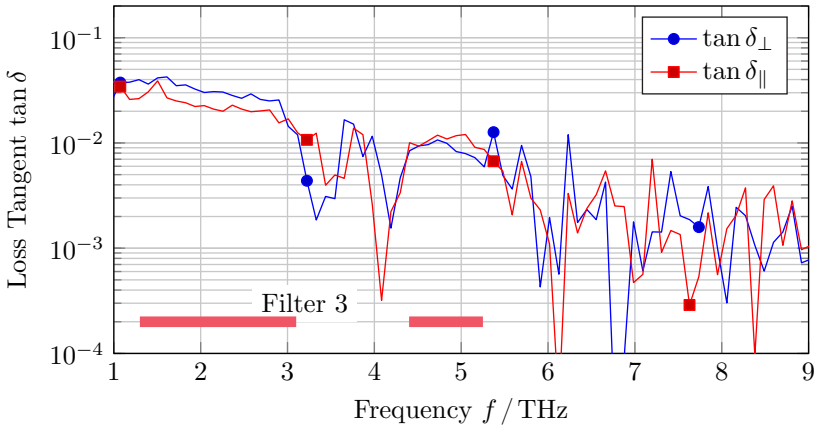

(b) Filter 3

Figure 3.27.: FTIR Spectrum: GT3-18017

This is an unexpected behaviour: normally, it is assumed that $\tan\delta_\parallel < \tan\delta_\perp$. The values obtained here only agree well with the results from the TDS measurements for Filter 1, where values of $\tan\delta \approx 1 \times 10^{-2}$ for both orientations were observed.

This behaviour is repeated with GT5-28004 in Figure 3.28 where both parallel and

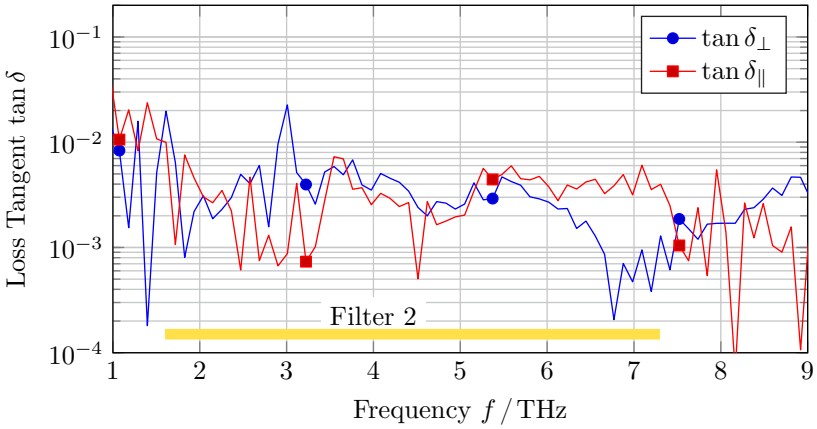

Figure 3.28.: FTIR Spectrum: GT5-28004

perpendicular orientations show similar loss tangents. Above 6 THz this changes suddenly with a steep decrease in $\tan\delta_\perp$. As this happens towards the upper end of the filter, it should be carefully considered. On the other hand, for example scattering of the wave should show the opposite effect and increase the apparent losses.

Finally, two experimental LCs were looked into: Merck-521 and Merck-893. The first is an extremely viscous material. So viscous in fact, that it took five minutes to fill the sample cell. This should be kept in mind when viewing the graphs, as it may indicate that the orientation by the magnetic field may have been incomplete.

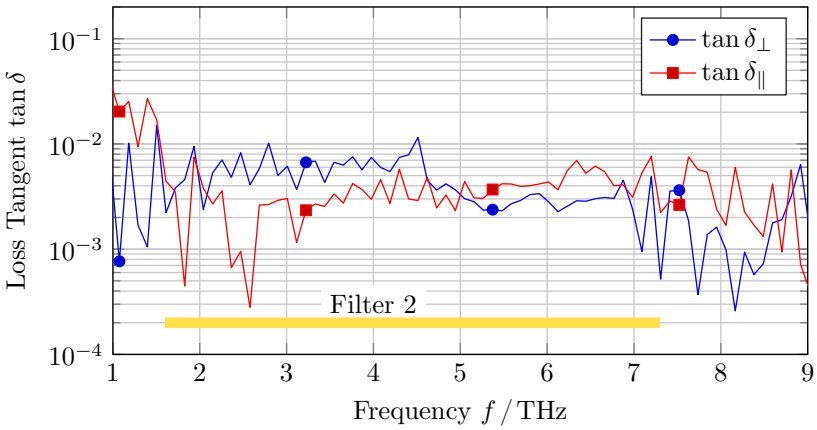

Figure 3.29.: FTIR Spectrum: Merck-521

Figure 3.29 shows a flat, low $\tan\delta$ below 1×10^{-2} with a cross-over at 5 THz similar to the phenomenon observed with GT3-18017. The range of $\tan\delta$ agrees with the

TDS results shown in Figure 3.25c.

The last LC, Merck-893 shows somewhat contradictory results with $\tan\delta$ constantly slightly below 1×10^{-2} in TDS data but starting above 2×10^{-2} and only crossing 1×10^{-2} at around 5 THz.

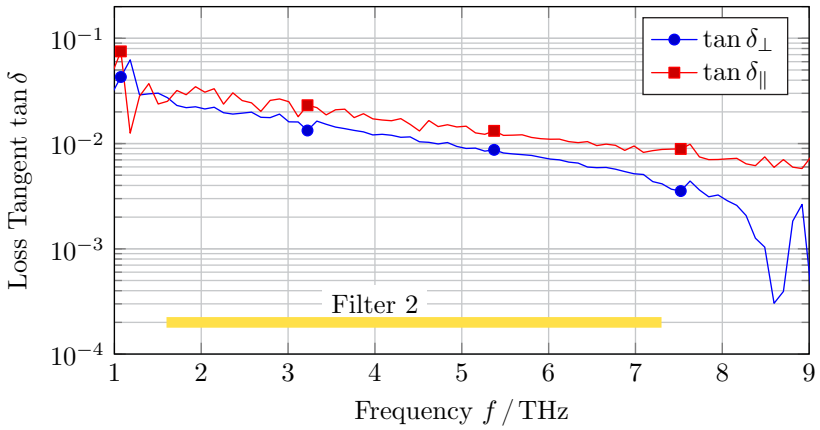

Figure 3.30.: FTIR Spectrum: Merck-893

At this point, it can only be speculated how these discrepancies come into being. One possible reason is scattering in the LC samples. This effect increases with higher frequencies as the wavelength becomes smaller and smaller when compared to defects and domains in the material, which causes the milky appearance in the visible range (see Figures 3.20c and 3.22b). However, the milky appearance is common to all discussed mixtures and there is currently no indication to why some would show this behaviour and others do not.

Results Review

The data presented in the previous section shows that in principle LCs are well suited for terahertz applications as their loss tangent remains relatively low over a wide range of frequencies. Also, the permittivity remains almost constant over a wide frequency range. No sudden increases in loss were observerd, neither were sudden drops in permittivity. Certain mixtures show an inversion of the losses with respect to the orientations compared to what is normally observed in the microwave and mm-wave range.

When compared to resonant measurements or transmission line based measurements in the microwave range, the quality of the data is low. While the resolution of the TDS measurements is approximately 130 datapoints per THz, FTIR measurements have only 8–10 points per THz in the range of interest. It should therefore be borne in mind that this is only a “quick look” into the properties of the present mixtures. Vieweg found much more diversity [Vie11] by looking at the individual compounds.

3.5. Conclusion

The methods presented in this chapter are by no means new. However, they have either been significantly extended, as in the case of the resonant method for parameter extraction, or applied to a new set of materials and over a wide frequency range, as in the case of the terahertz measurements.

Using the FEM to extract the material parameters from the resonant cavity measurements opens up a wide field of new resonator designs. As discussed in the case of the 60 GHz resonator, introducing tuning elements or simply considering the perturbation directly when setting the dimensions of the resonator in a very fast and effective way will help in designing new resonators and to extend the realm of resonant characterisation.

The results of the terahertz studies, however, showed that there is a lot of room for devices at even higher frequencies. Nevertheless, the measurement techniques could be improved and extended yielding for example permittivity data in addition to absorption data in the FTIR measurements.

4. The Lightweight Inter-Satellite Antenna (LISA)

4.1. Introduction

In the 1980s, first on-orbit servicing (OOS) missions were carried out [Sto+09]. In 1993, the Spacelab-D2 mission tested a robotic arm. More and more operations were carried out on-orbit. In parallel, the number of missions gathering large amounts of data grew with Earth-observation (EO) missions such as the European Remote Sensing Satellite (ERS) and its various successors (Envisat but also the Sentinel satellites) successfully surveyed global climate, geology or ocean currents. The main drawback of the OOS missions mentioned above was that they usally had to be operated by a human operator close by the vehicle, i.e. also on-orbit. With the DLR mission "Deutsche Orbitale Servicing Mission" (DEOS) and connected projects, the operator should be located on ground at mission control and the servicing satellite be entirely robotic [Rei+10]. Wilde et al. investigate operations like the approach to a spinning, "out-of-control" satellite (so-called *uncooperative target*) [Wil+15]. While the roundtrip time of 700 ms for such a link poses no problem, operators perceive the link as "good" when at least a frame rate of 7.5 framespersecond is provided. High definition video was not used in the approach study, but may help in repair missions.

The problem most EO missions have to deal with is the data downlink [Har+09]. Most EO missions are placed on LEOs for its relatively low altitudes (160 km to 2000 km above ground). While this is helpful for the mission objective, it is obstructive for data transmission which can only take place during a number of short time windows where the satellite has a ground station in sight, i.e. right below. This is eased nowadays by ground station networks that allow for a number of such time windows per orbit. For some use-cases (e.g. climate research) this is acceptable when data is buffered and then transmitted to earth in large, high data-rate bursts above ground stations. For others, like response to environmental disasters, the direct downlink has the disadvantage of delays in the order of 12 to 72 hours.

These two examples motivate the development a GEO based relay link from LEO (via GEO) to ground because a permanent connection would be beneficial in both cases [Lun+07]. Tracking and Data Relay Satellite System (TDRSS) was the first relay system. Advanced Data Relay and Technology Mission (Artemis), European Space Agency (ESA)'s first such satellite for example, served as a relay establishing a link from LEO to ground for Envisat.

The Sentinel satellites, for example, use an optical link to the European Data Relay Satellite (EDRS) in GEO. X-band direct downlinks are still in use although they may

conflict with mission objectives [Ros+12; Pot+12].

While even today EO missions could work with relatively low bandwidths, the teleoperations and robotics approach inspired the idea of wider bandwidth per channel. At the base of the definition for the LISA_{ES} there was the general use of 23 and 27 GHz bands for up- and downlink in several other systems. National Aeronautics and Space Administration (NASA)'s TDRSS, for example, defines a "Ka-Band Single Access" between 22.5 and 27.5 GHz with a data rate of 800 Mbits^{-1} [NAS01].

Artemis [ESA12], DEOS [Rei+10] as well as the Heinrich Hertz mission (Heinrich-Hertz) [SFO11; Voi10] use communication bands in this range.

Meteosat defines 25.5 GHz to 27 GHz as a downlink range for its third generation satellites [DW12, Chapter 7.1]. For the design and in order to maintain flexibility in case the design was chosen for either of the possible host systems, these bands were defined symmetrically to offer 500 MHz each for two reasons. Another reason was that in a multi-service scenario symmetric channels seem more likely and more useful, and second, because it was relatively straightforward with LC technology to acheive such broadband operation.

Other possible scenarios for a LEO-GEO-ground link could be envisioned: more and more satellite communication either for remote areas or services on the move are discussed. Here, the GEO capacity is clearly limited, so LEO services are brought into focus. These services would need a relay link to establish a (long-latency) permanent data link. There is a wide variety of possible applications: from civil users (e.g. fire brigades in remote areas or internet access on planes, ships or trains) to military users. Even consumer applications like internet access for camper vans are discussed. Obviously, the technology is also interesting for military purposes. It should be therefore noted that the Bundeswehr, the German military forces, joined the Heinrich-Hertz mission, making it a mixed civil-military mission to evaluate technologies.

4.2. Technichal Specifications and Scenario

The mechanical and electrical constraints of LISA_{ES} have been manyfold, often contradictory, and are therefore hard to meet. For example, constructing a mechanically robust metallic waveguide structure with liquid compartment somewhat contradicts the requirement of low weight.

This section will give an overview concerning the scenario in space. The critical benchmark figures for this application are calculated. The apparent angular speed of the tracked satellite is estimated based on a very simple model and translated into minimum requirements towards the minimum phase change rate necessary for the phase shifters in an array.

4.2.1. Derivation of Maximum Apparent Angular Speed of a LEO Satellite as Seen from Relay Satellite in GEO

The antenna has to be equipped to track a satellite in LEO being on a position in GEO [HHH13; Hoe+15]. The LEO's orbital speed, assuming low or no eccentricity of

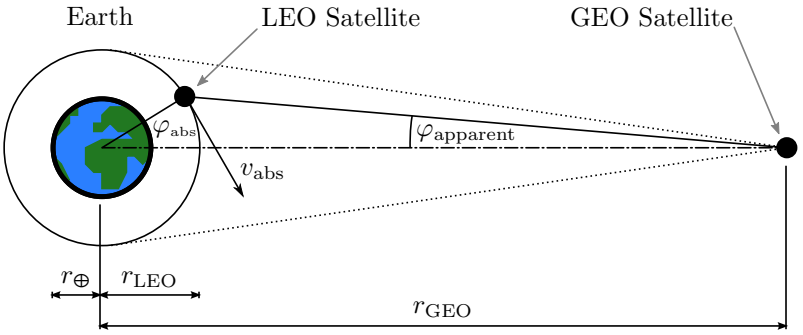

Figure 4.1.: Situation of a LEO satellite as seen from a GEO satellite.

the orbit and a typical satellite mass (i.e. $M_{\text{satellite}} \ll M_\oplus$) is obtained by

$$v_{\text{LEO}} = \sqrt{\frac{GM_\oplus}{r_{\text{LEO}}}}, \tag{4.1}$$

with the gravitational constant $G = 6.6738 \times 10^{-11}\,\text{m}^3\text{kg}^{-1}\text{s}^{-2}$ [NIS10], earth's mass $M_\oplus = 5.972\,19 \times 10^{24}\,\text{kg}$ and average radius $r_\oplus = 6367\,\text{km}$ [NASa] and an orbit radius r_{LEO} in the range of 6600 km to 8400 km. Depending on its altitude, the LEO has a period of

$$T_{\text{LEO}} = \frac{2\pi r_{\text{LEO}}}{v_{\text{LEO}}} = 89\,\text{min to } 128\,\text{min} \tag{4.2}$$

and therefore an angular rate of

$$\dot{\varphi}_{\text{LEO}} = \sqrt{\frac{GM_\oplus}{r_{\text{LEO}}^3}} = 4.05\,^\circ\,\text{min}^{-1} \text{ to } 2.82\,^\circ\,\text{min}^{-1}. \tag{4.3}$$

The maximum *apparent* angular velocity $\dot{\varphi}_{\text{app,max}}$ of the LEO satellite as seen from the GEO position is obtained by translating the absolute velocity v_{LEO} into an angular velocity with center of revolution at the GEO satellite, i.e. a radius of $r' = r_{\text{GEO}} - r_{\text{LEO}}$.

$$v_{\text{LEO}} = \dot{\varphi}_{\text{app,max}} \cdot r' \tag{4.4}$$

$$\Rightarrow \dot{\varphi}_{\text{app,max}} = \sqrt{\frac{GM_\oplus}{r_{\text{LEO}}\left(r_{\text{GEO}} - r_{\text{LEO}}\right)^2}} \tag{4.5}$$

The resulting maximum apparent angular velocity ranges from $0.666\,^\circ$/min to $0.792\,^\circ$/min.

The angular diameter δ of Earth is determined by the ratio of its radius to the distance D from viewpoint (in this case the GEO satellite) to its centre, i.e. $D = r_{\text{GEO}}$, as in

$$\delta = 2 \cdot \arctan\left(\frac{r_\oplus}{D}\right). \tag{4.6}$$

This results in 20.19° for the apparent disc of the earth.

The maximum apparent diameter of a LEO orbit is determined by its orbit radius r_{LEO} and computed in the same way. It ranges from 20.90° to 26.42°.

In order to obtain the dependency of the apparent angle φ_{app} from the orbital angle φ_{LEO}, one can assume the relative location $l_{\text{from GEO}}$ of the LEO as seen from the GEO as

$$l_{\text{from GEO}} = r_{\mathrm{GEO}} - r_{\mathrm{LEO}} \cdot e^{j\varphi_{\mathrm{LEO}}}. \tag{4.7}$$

The apparent angle $\varphi_{\mathrm{app}} = \varphi_{\text{from GEO}}$ is the phase of the complex phasor $l_{\text{from GEO}}$ which is given by the inverse tangent

$$\varphi_{\mathrm{app}} = \measuredangle\, l_{\text{from GEO}} = \tan^{-1}\left(\frac{\sin\varphi_{\mathrm{LEO}}}{r_{\mathrm{GEO}}/r_{\mathrm{LEO}} - \cos\varphi_{\mathrm{LEO}}}\right). \tag{4.8}$$

A good approximation for this expression is $r_{\mathrm{GEO}}/r_{\mathrm{LEO}} - \cos\varphi_{\mathrm{LEO}} \approx r_{\mathrm{GEO}}/r_{\mathrm{LEO}}$ and $\tan\varphi_{\mathrm{app}} \approx \varphi_{\mathrm{app}}$ for $r_{\mathrm{GEO}} \gg r_{\mathrm{LEO}}$, which is obviously the case. This leads to the simplified, approximated relation

$$\varphi_{\mathrm{app}} = \frac{r_{\mathrm{LEO}}}{r_{\mathrm{GEO}}} \cdot \sin\varphi_{\mathrm{LEO}}, \tag{4.9}$$

which can be differentiated with respect to time, knowing the constant angular velocity of the LEO orbit $\dot{\varphi}_{\mathrm{app}}$ to be

$$\frac{\mathrm{d}}{\mathrm{d}t}\varphi_{\mathrm{app}} = \dot{\varphi}_{\mathrm{app}} = \frac{r_{\mathrm{LEO}}}{r_{\mathrm{GEO}}}\dot{\varphi}_{\mathrm{LEO}}\cos\varphi_{\mathrm{LEO}}. \tag{4.10}$$

Inserted into the array formula for the phase Φ of an individual element on position n, this yields

$$\Phi = \frac{kd}{2}(N-1)\sin\varphi_{\mathrm{app}} = \frac{kd}{2}(N-1)\sin\left(\frac{r_{\mathrm{LEO}}}{r_{\mathrm{GEO}}} \cdot \sin\varphi_{\mathrm{LEO}}\right) \tag{4.11}$$

or in terms of the shift rate $\dot{\Phi}$, i.e. the phase shift change over time,

$$\dot{\Phi} = \frac{kd}{2}(N-1)\frac{\mathrm{d}}{\mathrm{d}t}\sin\varphi_{\mathrm{app}} \tag{4.12}$$

for a center-pivoted linear array of N elements with spacing d and k the wavenumber.

$\dot{\Phi}$ is maximised when $\dot{\varphi}_{\mathrm{app}}$ is maximised. This is the case for $\varphi_{\mathrm{app}} \approx 0$, i.e. when the LEO is straight below the GEO. $\dot{\varphi}_{\mathrm{app}}$ then becomes

$$\dot{\varphi}_{\mathrm{app}}^{\mathrm{max}} = \frac{r_{\mathrm{LEO}}}{r_{\mathrm{GEO}}}\dot{\varphi}_{\mathrm{LEO}}. \tag{4.13}$$

The time dependency at this point can be approximated linearly with $\sin x \approx x$ such

Figure 4.2.: Comparison of three standard waveguides (WR42, WR34 and WR28) with the LISA waveguide. Attenuation is calculated assuming copper walls.

that finally

$$\dot{\Phi}^{\max} = \frac{kd}{2}(N-1)\frac{\mathrm{d}}{\mathrm{d}t}\sin\left(\dot{\varphi}_{\mathrm{app}}\cdot t\right) \approx \frac{kd}{2}(N-1)\frac{\mathrm{d}}{\mathrm{d}t}\left(\dot{\varphi}^{\max}_{\mathrm{app}}\cdot t\right) = \frac{kd}{2}(N-1)\dot{\varphi}^{\max}_{\mathrm{app}} \quad (4.14)$$

and hence

$$\dot{\Phi}^{\max} = \frac{kd}{2}(N-1)\frac{r_{\mathrm{LEO}}}{r_{\mathrm{GEO}}}\dot{\varphi}_{\mathrm{LEO}}. \quad (4.15)$$

Using the angular rates obtained before and assuming a 16-element array, this evaluates to a phase change rate of

$$\dot{\Phi}^{\max} = 46.84\,^{\circ}\,\mathrm{min}^{-1}\ldots 57.29\,^{\circ}\,\mathrm{min}^{-1}, \quad \text{at } 23\,\mathrm{GHz} \text{ and} \quad (4.16)$$

$$\dot{\Phi}^{\max} = 59.61\,^{\circ}\,\mathrm{min}^{-1}\ldots 72.91\,^{\circ}\,\mathrm{min}^{-1}, \quad \text{at } 27\,\mathrm{GHz} \quad (4.17)$$

4.2.2. Antenna Gain and Choice of Frequency Bands

The $\mathrm{LISA_{ES}}$ antenna demonstrator features a symmetric 1:16 feed network mainly developed in its mechanical predecessor $\mathrm{LISA_{MS}}$ (Light-weight Intersatellite Antenna – Mechanical Steering) [PHW09]. However, the $\mathrm{LISA_{ES}}$ network is static, i.e. it does not contain moveable parts. The feed network defines a custom waveguide cross-section of $7.30\times3.35\,\mathrm{mm}^2$ which is a compromise: it offers the combined bandwidth of a WR34 *and* a WR28 waveguide. Its reduced height is due to geometrical constraints in the antenna feed network. On the other hand, group velocity dispersion and attenuation are increased towards the lower end of the band (cf. Fig. 4.2 on page 63).

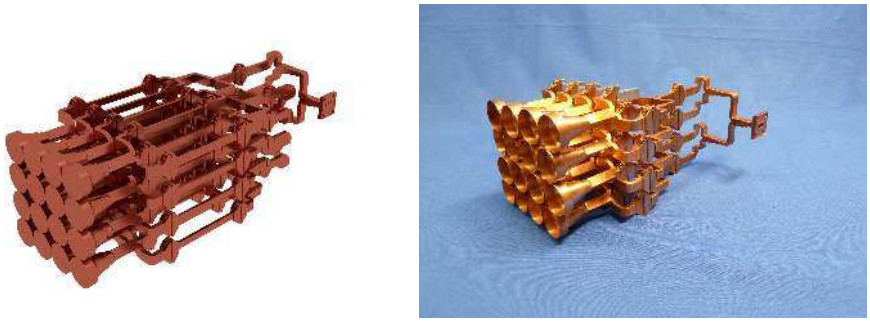

(a) CAD visualisation (b) Fabricated parts without phase shifters

Figure 4.3.: CAD visualisation and photo of the $\mathrm{LISA_{ES}}$ array structure (CAD model and photo courtesy LRT and LLB, TUM)

In LISA_{MS}, the feed network was directly connected to an array of horns to achieve high overall gain [PHW09]. In LISA_{ES} a new layer is inserted: the horns, with individual gain of more than 15 dBi, and the feed network are connected through an array of Liquid crystal phase shifters [HHH13; Wei+13a; Wei+13c] which are the subject of this chapter. Calculations (analytic and using CST, NTP-Ingenieure GmbH & Co. KG, Neubiberg, Germany (NTP)) showed an acheivable broadside gain, for the 4×4 array, of more than 27 dBi at 23 GHz. Extrapolated to the 16×16 array this translates into an overall gain of approximately 39 dBi.

The feed network and the LISA_{ES} antenna are designed to cover a large bandwidth, incorporating a large portion of the K-band but also the lower end of the Ka-band, and to provide the capacity to handle large power load. This is made possible by the excellent linearity of LC [Goe+06; Göl09].

The frequency bands were chosen based on the earlier data relay missions like TDRSS or DEOS. As mentioned earlier, the LCPS allow for wideband usage. The antenna's operational bands are therefore extended to 500 MHz bandwidth for each band and set to 23.0 GHz to 23.5 GHz and 27.0 GHz to 27.5 GHz, respectively. Furthermore, there is no fundamental reason not to use further bands. The dispersion caused by the array can be compensated using the LCPS and a wide operational frequency range is generally available.

4.2.3. Mass

A central aspect when developing a demonstrator for space is to consider its mass. The initial concept that led to the development of LISA_{ES}, published by Gäbler et al. [Gäb+09b], did not consider weight as a problem and as such suggested a full brass waveguide. The conventional fabrication approach would consist in stripping down the metal cladding of a waveguide phase shifter to a minimum. However, this would still cause significant mass per length.

For a long waveguide, arguably a 0.75 mm wall thickness may be considered the best case possible. Consider Figure 4.4 which is based on [Gäb+09b]: Assuming a brass phase shifter of these dimensions[1] the mass of the compontent would result in approximately

$$M' = M_{\text{met}} + M_{\text{cont}} + M_{\text{LC}} \tag{4.18}$$

$$= \underbrace{0.1615\,\text{g/mm}}_{\text{Metal}} + \underbrace{0.0078\,\text{g/mm}}_{\text{Container}} + \underbrace{0.0071\,\text{g/mm}}_{\text{LC}} = 0.1765\,\text{g/mm}. \tag{4.19}$$

This is mainly due to the high density of any metal. For the structure presented in [Gäb+09b], this for example translates into a 2π phase shifter which at 30 GHz requires 70 mm and therefore weighed at least 12.35 g – not considering any flanges! The structure presented in this chapter is even longer, and would result in a total weight of 21.18 g for the waveguide alone.

[1] Brass: $w_{\text{met}} \approx 0.75\,\text{mm}$, $\varrho_{\text{Brass}} \approx 8.5\,\text{g/cm}^3$; PTFE: $w_{\text{cont}} \approx 0.5\,\text{mm}$, $\varrho_{\text{PTFE}} \approx 2.2\,\text{g/cm}^3$; LC: $w_{\text{LC}} \approx 2\,\text{mm}$, $\varrho_{\text{LC}} \approx 1\,\text{g/cm}^3$

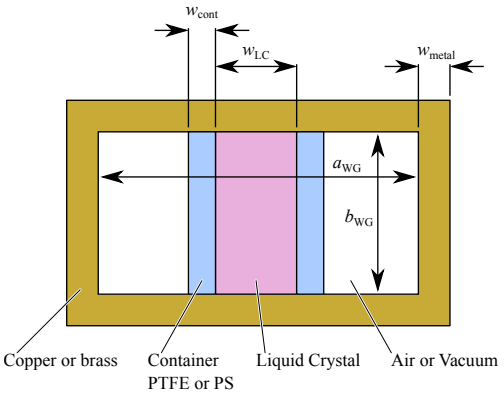

Figure 4.4.: Proposed cross-section before project start. Metallic waveguide walls provide structural stability. The air or vacuum filled portion of the cross-section is intended for minimum IL. Dimensions and relations are approximate.

In the conventional way of fabrication, such a long and thin-walled waveguide would not be possible. A different process of fabrication is therefore used. It results in significantly thinner waveguide walls and mechanically favourable properties. It is presented on the following pages in Section 4.3.

Specifically, after the development efforts and considerations are discussed that were not obvious from the start, Section 4.3.4 summarises the process and gives a weight figure.

4.2.4. Overview of Technical Specifications

Table 4.1 sums up the general technical specifications.

	Unit	4 × 4 Demonstrator	16 × 16 Model
Operational Frequencies	GHz	23 and 27	
Antenna Gain	dBi	25	37
Scanning Range	°	±11 conus	
Beam Scanning Speed	°/min	0.666 to 0.792	
Element Tuning Speed	°/min	8.0 to 17.1	46.84 to 72.91
Size	mm^2	100 × 100	400 × 400

Table 4.1.: Technical specifications for the LISA 4 × 4 demonstrator and the 16 × 16 model.

Particular attention should be given to the two speeds under consideration. While the beam scanning speed is fixed by the scenario, the element tuning speed depends directly on the number of array elements. This imposes a natural limit onto the size of waveguide based LC phased arrays.

4.3. Lightweight Phase Shifter Design

From the general constraints and specifications discussed before, a more specific set of technical specifications for the individual LCPS can be derived. The LCPS' length is governed by the efficiency of the device in terms of phase shift per length. The cross-section is mainly limited by the waveguide cross-section defined by the feed network and the space constraints imposed by the array layout.

Initially, a highly integrated design close to the initial suggestion by Gäbler et al. was conceived (cf. Fig 4.5). In contrast to the former suggestion [Gäb+09b], it does no longer contain air- or vacuum-filled regions in its cross-section. Its qualitative layout is shown in Figure 4.5 and described the starting point of LISA_{ES}.

The waveguide cross-section is divided into three domains: (1) LC in the centre, (2) dielectric on the left and right side and (3) a polymer sheet (e.g. Mylar®) sealing off the LC reservoir and carrying the biasing electrodes.

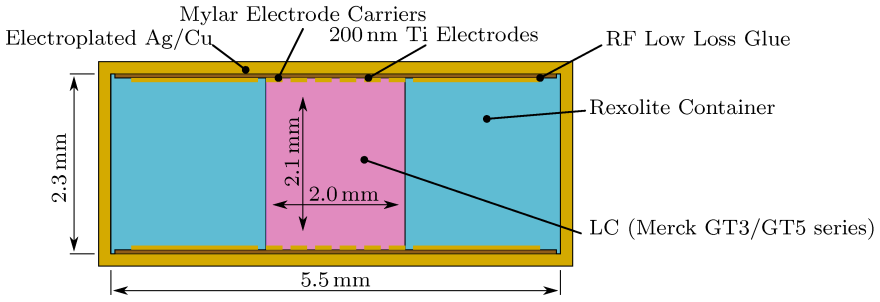

Figure 4.5.: Proposed cross-section on project start. Metallic waveguide walls support structural stability. The main structural carrier is the Rexolite core. Dimensions and relations are approximate.

The design was compact and simulations showed a high phase shift per length and good figure of merit which are shown in Table 4.2 for two LC mixtures. The first devices were fabricated in 2011 but soon revealed a major drawback of the design: it is extremely difficult to assemble. The electrode sheets were glued onto the Rexolite container and it turned out to be almost impossible to close this seam against LC leaks (see glossy areas in Figure 4.6b where LC can be seen covering the whole structure on the surface). Hence, the rate of failing devices due to LC reservoir leaks was 100 %. Furthermore, the design was monolithic, therefore rendering variations impossible. When exceptionally high IL were observed during a set of measurements they could not be clearly attributed to either the LC performance, the leakage or the electrodes

Band	23 GHz to 23.5 GHz			
Material	$\mathbf{\Delta\Phi}$ / °	IL / dB	FoM / °dB^{-1}	$\mathbf{\Delta\Phi}$ / °mm^{-1}
GT3-23001	439.74	3.46	127.07	6.28
GT5-26001	478.94	1.81	264.32	6.84
Band	27 GHz to 27.5 GHz			
Material	$\mathbf{\Delta\Phi}$ / °	IL / dB	FoM / °dB^{-1}	$\mathbf{\Delta\Phi}$ / °mm^{-1}
GT3-23001	465.92	3.59	129.74	6.66
GT5-26001	504.89	1.89	267.49	7.21

Table 4.2.: Predicted performance figures of the initial design (only 70 mm of LC channel) for two LC mixtures GT3-23001 and GT5-26001

on the biasing sheets.

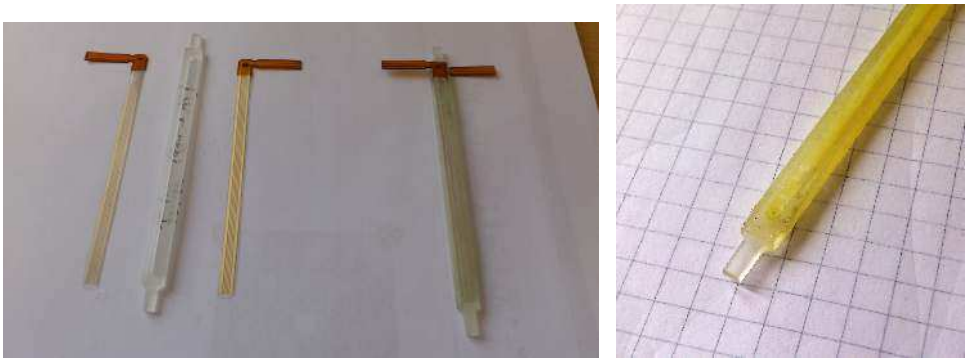

(a) Picture of initial monolithic LCPS (b) Picture of broken device

Figure 4.6.: Photographs of the monolithic design which failed mainly due to problems attaching the electrode sheet to the LC container

It did, on the other hand, prove that given a proper understanding of how to fabricate, assemble and glue polymer components, the LCPS design may be significantly improved.

As a consequence, the design was modularised. The biasing electrodes were separated from the LC reservoir. In several steps the filling method was developed to allow reliable filling, re-filling and sealing.

4.3.1. Container Design

Considering the large fill-factor of the container material, careful research was carried out to which material should be used to house the LC reservoir. Polytetrafluoroethyl-

ene (PTFE), commonly referred to by DuPont's brand Teflon®, was ruled out due to its softness and hence bad fabrication properties and the fact that glueing material to PTFE is particularly complicated. Further research suggested to use Rexolite-1422, a cross-linked polystyrene with excellent microwave properties:

- Low permittivity of $\varepsilon_r = 2.54$ at 10 GHz and $\varepsilon_r = 2.53$ up to 500 GHz according to C-Lec Plastics Inc.[2]
- Low dissipation factor of $\tan\delta = 6.6 \times 10^{-4}$ at 10 GHz which was confirmed in this work to be less than 1×10^{-3} between 20 GHz to 30 GHz
- Low specific gravity of 1.05 g/cm^3 and high tensile strength, i.e. excellent mechanical properties supporting the antenna structure
- Low outgassing, a prerequisite to be used in space applications
- Available in ESA's and NASA's material databases [ESA15; NASb]

The permittivity is low and only slightly larger than the typical $\varepsilon_\perp \approx 2.4$ of many LC mixtures. Compared to typical parallel permittivities with $\varepsilon_\parallel \approx 3.2$ this provides a large contrast and results in a relatively strong field confinement in the LC. Tuning efficiency is therefore increased.

The low relative permittivity makes matching the feed network against the phase shifter easier. The phase shifter cross-section is decreased as to keep the cut-off frequency in the range of 20 GHz to 21 GHz in all tuning states at a LC fill-factor of approximately 1/3. This resulted in waveguide dimensions of 5.5 mm × 2.3 mm.

The container incorporates two main functions: containing the LC and providing the taper between feed network and phase shifter section on one side and phase shifter and horn on the other side. The design process was carried out in CST.

Determining the Cross-section The LC reservoir dimensions were determined as follows: the height h_{LC} is chosen as large as possible. Essays in milling Rexolite and subsequent sealing tests at TUM have suggested 150 µm as the minimum wall thickness which can be fabricated, the safe minimum is 200 µm. h_{LC} is therefore chosen to be 1.8 mm.

In an iterative process, the initial LC reservoir width was $w_{\mathrm{LC}} = 2.2$ mm to ensure a 33 % fill factor. At the end of the process however, the width was chosen to be $w_{\mathrm{LC}} = 2.5$ mm in order to achieve 600° phase shift with a 120 mm device (i.e. 100 mm LC channel). The fill factor is therefore 37 %.

The Rexolite container was fabricated in at least three different ways over the whole duration of the project:

1. The initial approach consisted of a U-shaped bottom with the reservoir and a stamp-like cover which were assembled using Rexolite adhesive. However the bond was not free of air bubbles and the adhesive was hard to process.

[2] Cf. http://www.rexolite.com/general-qualities and [San13]. Other results: [FB97]

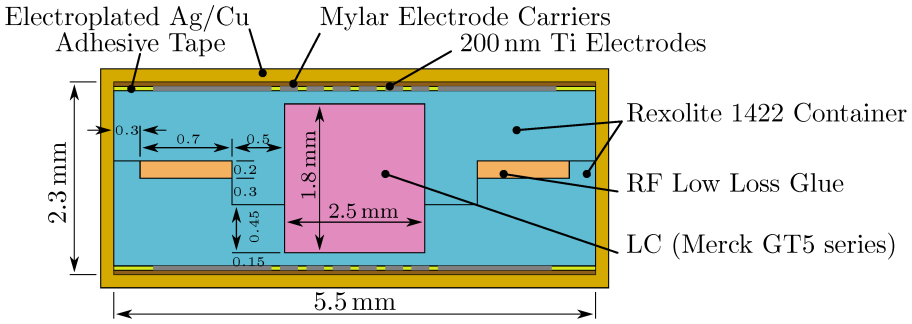

Figure 4.7.: Final cross-section design of the LISA_{ES} LCPS. The 50 µm Pyralux AP electrode carriers are attached to the container using 50 µm adhesive tape. The overall height is 2.3 mm, with the container height being only 2.1 mm. The top and bottom wall thickness of the container (rosé) is only 0.15 mm. Once container and sheets are assembled, the wall is deposited by evaporation of some 100 nm to 1000 nm of silver (Ag) and subsequently electroplated with Copper (Cu) to form some µm of metallic wall. Drawing not to scale for readability, all dimensions in mm.

2. In a second approach, the cutting plane was tilted from a horizontal cut to a vertical cut, resulting in a C-shaped reservoir and a vertically aligned stamp-like cover. The joint between the two parts was improved by a larger contact area and a perforation which improved outgassing and significantly improved the joint quality despite the use of Rexolite adhesive. However considerations concerning the LC filling process required a redesign.

3. In the last step, the cutting plane was tilted back to the horizontal plane, cutting the container symmetrically. The cover part is perforated in order to allow for uniform outgassing. The Rexolite adhesive was replaced by an epoxy-based RF-compatible adhesive, Zeiss Glue 56, which has better curing properties and results in much more reproducible joints (cf. Fig. 4.7: yellow indicates the adhesive channels, magenta indicates LC and tank and lid parts of the container are indicated in blue).

This final layout is presented in Figure 4.7.

While the initial design had a height of 2.2 mm, the final height of the container rather is 2.3 mm. This was inspired by the 50 µm adhesive sheet put underneath each biasing sheets.

4.3.2. Phase Shifter Length and Matching

Every continuous phase shifter's length is mainly governed by the maximum desired phase shift. In the case of LISA_{ES} it should provide 360° continuous phase shift.

Looking at the transient phase measurements at the end of this chapter and previous work, e.g. [Hu11], the switching step, that has to occur from 360° back to 0°, takes time. Hu discusses this issue and suggests spreading the instants when a jump occurs over a certain span. This requires leeway in order to delay the jump and continue increasing (or decreasing the phase shift). It was therefore decided to increase the desired maximum phase shift to 400°, thus yielding a 11 % leeway.

When first measurements were carried out, for several reasons the desired 400° were far from being reached. As a result of these uncertainties, it was concluded that the phase shifter prototype should be designed for 600° phase shift. The real phase shifters usually provide about 10 % less. The decision for example would allow for an exchange of the typically used LC GT5-26001 to a hypothetical blend that – while introducing lower losses – offers a lower tunability. The phase shifter would still function. Furthermore, this approach would allow a study of array performance depending on the state of phase shifters in an array: the "regular" performance, that is obtained when phase shifters switch at 400°, could be compared to a case were switching is omitted due to the large available leeway.

Tebbe et al. have recently investigated the influence of the switching process and the reduction in gain which results from it. While large gain reductions were observed where the array was used without any leeway, the overall gain reduction could be kept at 3 dB with delayed switching, taking advantage of the extra range in differential phase shift [Teb+16].

LC Name	**Method**	$\varepsilon_{\parallel}$	$\tan\delta_{\parallel}$	$\varepsilon_{\perp}$	$\tan\delta_{\perp}$
GT3-23001	CPM (IMP)	3.16	3.3×10^{-3}	2.47	15.1×10^{-3}
GT3-23001	CPM (Merck)	3.28	3.8×10^{-3}	2.46	14.3×10^{-3}
GT5-26001	CPM (Merck)	3.27	2.2×10^{-3}	2.39	7×10^{-3}
GT5-28004	CPM (Merck)	3.32	1.4×10^{-3}	2.4	4.3×10^{-3}

Table 4.3.: LC Mixtures considered for LISA_{ES}. Characterisation method: 19 GHz cavity perturbation method [Gäb15]

Using the material data given in Table 4.3 (courtesy Merck), the phase shift profile shown in Figure 4.8 and Table 4.4 is obtained by means of numerical simulation using FEniCS with a method described in Appendix A.2. In this case, LC director dynamics have not been considered: the steady state is assumed such that $\vec{E}_{\text{DC}} \parallel \vec{n}$ everywhere in the LC.

Despite showing the lowest performance in phase shift (Table 4.4), GT3-23001 was chosen as material for the LISA_{ES} prototypes for its availability, significantly faster tuning speed than Merck Licristal® GT5-28004 and better long-term stability than GT5-26001[3].

Confirming these calculations, simulations using both CST and the FDTD simulator for LC and RF dynamics (SimLCwg) showed that between $5\,^{\circ}\,\text{mm}^{-1}$ to $6\,^{\circ}\,\text{mm}^{-1}$ were

[3] GT5-26001 was considered less stable than GT3-23001 against spontaneous phase changes due to pollutants likely to get in contact with the material during fabrication.

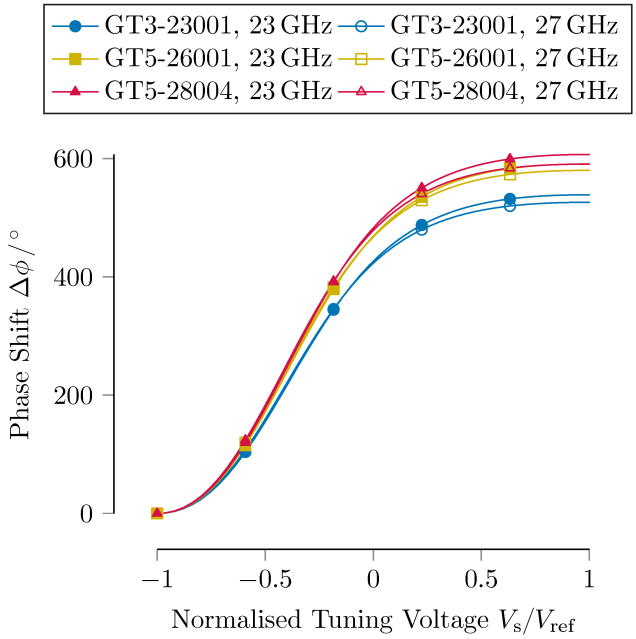

Figure 4.8.: Calculated phase shift over full tuning voltage range assuming ideal LC orientation for three LC mixtures evaluated in the two bands (23 GHz and 27 GHz)

possible. It should be noted though, that in CST the LC was modeled as isotropic material with $\varepsilon_{\parallel}$ and $\varepsilon_{\perp}$ respectively, so the maximum phase shift is generally overestimated.

The length of the LC container was therefore fixed to 100 mm, the cross-section profile extruded accordingly to 100 mm length and capped by a taper on each side. The taper's function is threefold: to close the container, to provide a filling channel and to taper electrically from the LISA-flange to the phase shifter cross-section. Moreover, the condition for "good" matching is to achieve at least $|S_{11}| = |S_{22}| \leqslant 15\,\mathrm{dB}$ in the two bands considered.

In order to fulfill these requirements, a stepped impedance transformer is set up. The initial waveguide cross-section (i.e. the outline) is converted into the cross-section in one single step. The dielectric filling, however, is increased stepwise: a first small brick centered in the E-plane is followed by a larger brick. Finally, the container is reached. To ease fabrication, the bricks are aligned with the bottom of the phase shifter, so the piece does not need to be turned and machined from the backside. When designing the taper, the input plane is in the LISA cross-section, the output plane is located at the beginning of the LC reservoir. In order to fill the LC reservoir, the taper is extended by a chimney-like structure (referred to as chimney) that mates with micro-fluidic flanges.

Mixture	f / GHz	$\Delta\beta$ / m^{-1}	$\Delta\phi$ / °
GT3-23001	23	94.06	538.94
GT3-23001	27	91.84	526.22
GT5-26001	23	103.15	591.00
GT5-26001	27	101.27	580.26
GT5-28004	23	105.97	607.14
GT5-28004	27	103.12	590.83

Table 4.4.: Maximum phase shift for three LC mixtures evaluated in the two bands (23 GHz and 27 GHz). For $\Delta\phi$ a length of 100 mm is assumed.

The length between the chimney and the beginning of the LC reservoir is fixed. It serves as space for inserting the electrode sheets, more specifically the ribbon carrying the contact leads to connect to the exterior electronics.

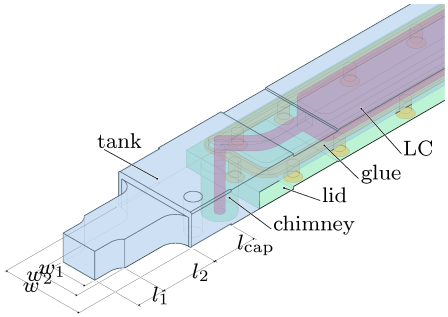

(a) Isometric projection of the taper structure

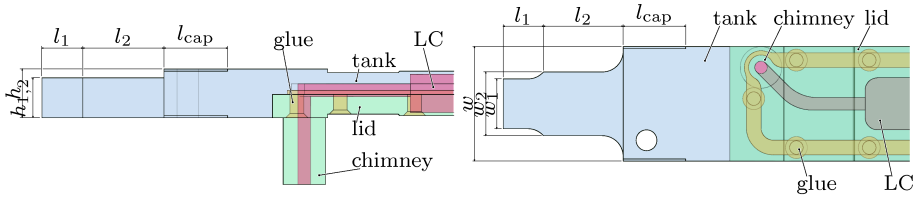

(b) Side view

(c) Top view

Figure 4.9.: Overview of the taper structure for the LISA phase shifter

Each brick is characterised by its length, width, and height, resulting in six parameters. The relative position of the waveguide wall step is another variable. This produces a seven-dimensional, i.e. very large problem space. The automated optimiser in CST was used to this end.

Lastly, the bricks are merged and the inner edges are tapered with an inner radius of

1 mm to ease fabrication. Additionally, a hole is added which serves as alignment hole for a pin which is inserted through the flange once it has been fit with the assembled body. The optimisation is run again to account for these design changes with a smaller optimisation margin.

When the container is closed and sealed with electrode sheets applied (see Section 4.3.3), the flanges are attached at TUM. It is aligned using the container geometry with an optional alignment pin to prevent the flanges from slipping off the assembly. An assembly is shown in Figure 4.10, both in full and in cut view.

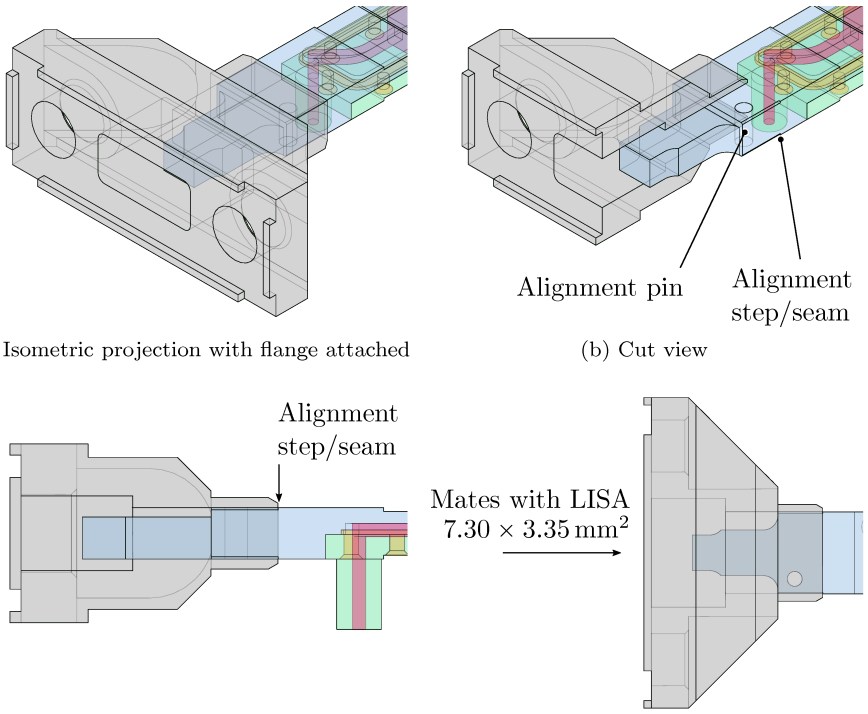

(a) Isometric projection with flange attached

(b) Cut view

(c) Side view

(d) Top view

Figure 4.10.: LISA container with attached flange

The flanges serve both as connectors and step in waveguide cross-section. On the container side, a waveguide of $5.5 \times 2.3\,\mathrm{mm}^2$ across is provided. Towards the feed network and across the flange plane, a cross-section of $7.30 \times 3.35\,\mathrm{mm}^2$ is implemented. On each side of the container, there is a male and a female version respectively, which mates with a fitting LISA $7.30 \times 3.35\,\mathrm{mm}^2$ flange of the respective opposite orientation. Only one version is shown in Figure 4.10.

Several design and optimisation runs have been carried out both by the author as well as Ralf Gehring with NTP. The design presented in Figure 4.9 is `TUM-LI0514-01` obtained by NTP and was fabricated in two batches throughout 2015.

4.3.3. Biasing Electrodes and Network

The biasing electrodes were a major design question in the LISA_{ES} project. Several unknowns had to be clarified. In Gäbler et al. [Gäb+09b], the biasing electrodes were lithographically processed onto a transparent biaxially-oriented polyethylene terephthalate (boPET) substrate with an evaporated Aluminium layer provided by HVB GmbH, Berlin. The primer was conventional packaging material (metal coated boPET for lower gas permeability). In the initial biasing electrode designs, this material was used. However, for the given phase shifter lengths the yield from fabricating the electrode sheets was extremely low (approximately only 1 in 20 was functional). At first it seemed inexplicable until it was explained that Aluminium evaporated on PET substrates never forms closed, homogeneous layers. It rather forms a perforated, inhomogeneous metal layer which is visible against the light. This phenomenon is known as the "starry sky" (*Sternenhimmel*) effect. Long research carried out by TUM resulted in a replacement: commercial low-dissipation Pyralux AP with custom 200 nm Titanium electrodes.

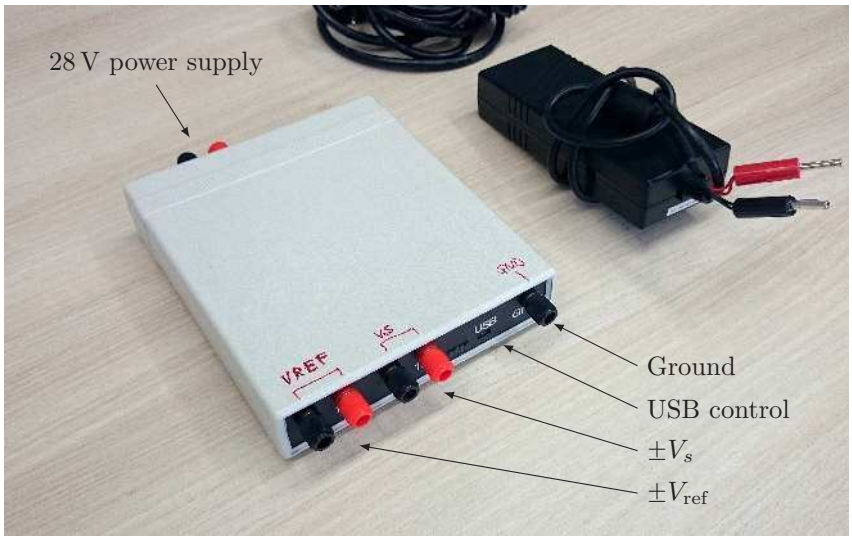

Figure 4.11.: Electronic Driver Box for the LISA_{ES} phase shifters built at IMST GmbH

The final design of the biasing electrodes consists of three main components: the carrier sheet (Pyralux AP), the Titanium electrodes and the screen-printed resistive network.

The voltages needed for biasing are provided by the electronic driver box developed by IMST GmbH, Figure 4.11. It provides two variable voltage channels V_{ref} and V_s of ± 164 V with respect to common ground. They are connected to the outer contacts of the electrode sheets described in the following paragraphs in a way described in Figure 4.12.

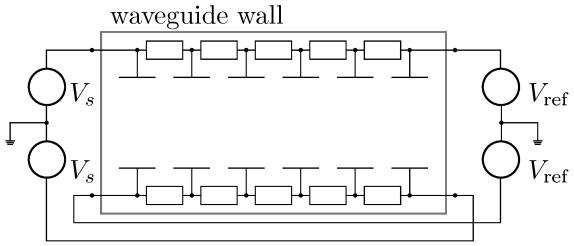

Figure 4.12.: Connection diagram for electrical biasing. Each pair of sources is connected diagonally, resulting in either vertical or horizontal potential drop for the two extreme biasing states.

Carrier Sheet The electrodes are processed onto a sheet of Pyralux AP by Cicor Reinhardt Microtech GmbH, Ulm, Germany (Cicor). The Pyralux AP sheet is 50.8 µm thick[4], has low RF dissipation ($\tan\delta < 5 \times 10^{-3}$ at 18 GHz) and a relative permittivity of 3.3 at 10 GHz (cf. [DuP09]).

Four sheets at a time are processed on one substrate (sheet of 152.4 mm × 127 mm).

Metallisation The provided Pyralux AP sheets come with copper cladding which is removed initially. Later, the electrode structure is processed lithographically at Cicor. Its structure is depicted in Fig. 4.13.

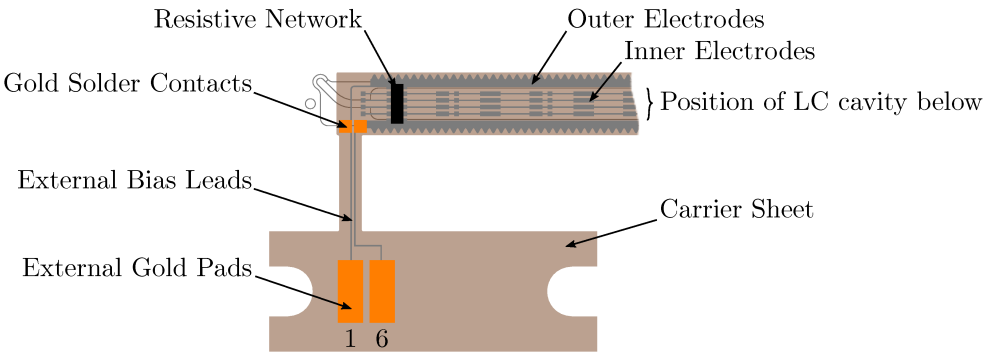

Figure 4.13.: Drawing of the electrode structure: leads provide external contact, the inner electrodes "soften" the potential drop and create a smooth $\vec{E}_{\mathrm{DC}}$, the outer electrodes contain ripples that suppress spurious strip modes.

The electrodes are made of Titanium for two reasons: (1) Titanium, while hard to process, is inert against the chemicals employed in the electroplating process which forms the metall waveguide in the final phase shifter. On the other hand, (2) the specific conductivity of Titanium is very low which makes it less perturbing for the

[4] As a variation, sheets of 25.4 µm are processed as well, but considered too fragile to work with.

guided RF mode. In order to improve contact resistance and make handling easier, the contact pads are electroplated with a sequence of Au, Ni and Au.

Resistive Network The biasing is supposed to work current-less, i.e. the potential drop along the width of the waveguide is designed to be achieved via a resistive network with high overall resistance. This is achieved by screen-printing a patch of Polymer Resistor Series ESL RS 12116 across the bias lines.

Surprisingly, incorporating the resistive network into the RF part of the phase shifter does not degrade performance much. The RF dissipation of the Polymer Resistor RS 12116 is not known. This might become of concern once power handling capabilities of the phase shifters are of interest, but so far there is no indication that it will impede performance. The integration rather improved performance, since the four slots needed to feed the biasing lines can now be smaller by a factor of 2–3 compared to the approach where every single line is fed from outside.

The implemented network features an overall resistance in the range of 1 MΩ to 20 MΩ with the final batches being consistently in the range of 10 MΩ to 20 MΩ. The conductivity of Ti is high enough so the bias lines do not contribute notably to the overall resistance of the network. The capacitance of bias lines to waveguide wall dominates the capacitive behaviour of the arrangement. It can therefore be modeled electrically as shown in Fig. 4.14.

A SPICE[5]-Simulation was carried out in order to verify that the driving voltage is distributed properly within the phase shifter. The voltage gain of a signal inserted from one pad (here Pad 1) degrades towards the right (Pad 6) but remains less than 3 dB attenuated for frequencies up to almost 400 Hz. This is sufficient for electrical biasing without the danger of charge migration in the surrounding materials, in particular in the LC.

The attenuation is obviously a result of overall electrode capacitance and inter-electrode resistance of the form of an RC low pass filter. The values proposed here are extracted from geometry in the case of the capacitances and depend mostly on the length of the phase shifter (i.e. a shorter phase shifter results in lower capacitances).

The resulting DC potential is calculated using FEniCS and a simple, charge-free Poisson equation. The electrodes' potential is defined by the resistive network and the resulting potential is indeed rather "smooth" as Fig. 4.15 shows.

The field lines show that the electrical field is not homogeneous and thus the director field $\vec{n}_{\mathrm{DC}}$ cannot be perfectly aligned. The actual director field is the result of a complex reorganisation process. Biasing the LC with a strong, homogeneous magnetic field yields the most homogeneous results (e.g. by large permanent magnets). The result of the electric biasing comes close, as the measurements will prove, but always remains below the performance of the magnetically biased case.

Obviously, the potential depends on the actual resistance values between adjacent electrode lines. The variation $\sigma_{(n,n+1),(1\ldots S)}$ of one resistance $R_{(n,n+1),s}$ over all sheets S is only important for the variation in voltage gain (see Figure 4.14b). This gain,

[5] A SPICE compatible package was used: the GNU Circuit Analysis Package (Gnucap), Version 2009.12.07 RCS 26.136

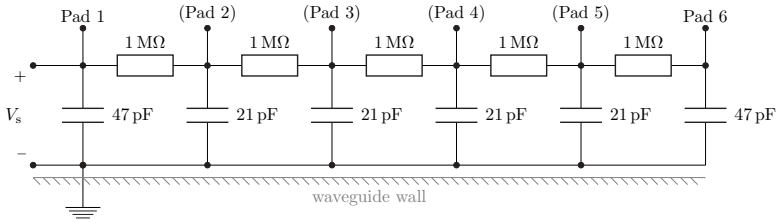

(a) Equivalent biasing circuit (bias V_s)

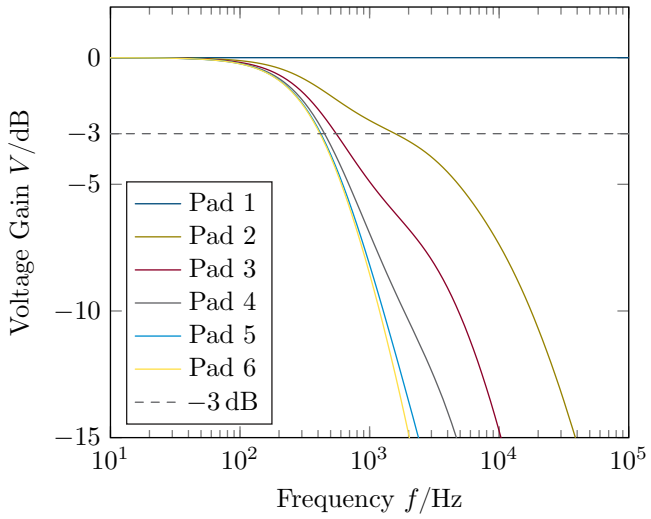

(b) Voltage transmission onto biasing lines

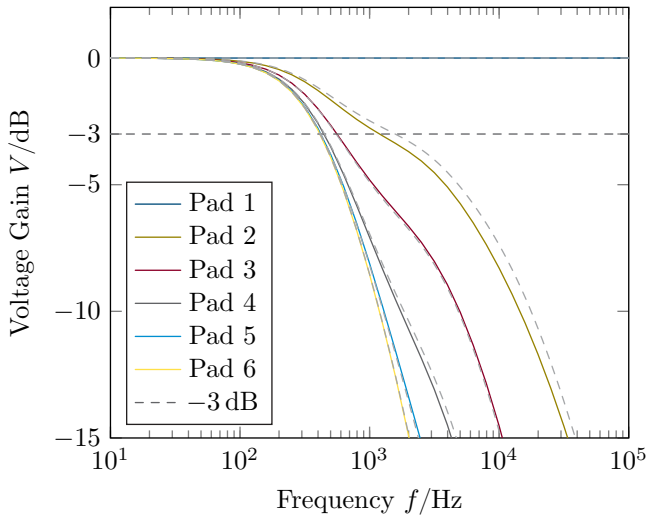

(c) Voltage transmission onto biasing lines if adjacent resistors vary by up to 30 % (dashed lines refer to equal resistances)

Figure 4.14.: Equivalent circuit model and calculation results of a biasing electrode sheet at the waveguide wall. The electrodes are separated from the wall by 50 µm polyimide film. For comparison, a case where adjacent resistors vary by 30 % is shown ($R_{1,3,5} = 1.1\,\mathrm{M\Omega}$, $R_{2,4} = 0.85\,\mathrm{M\Omega}$)

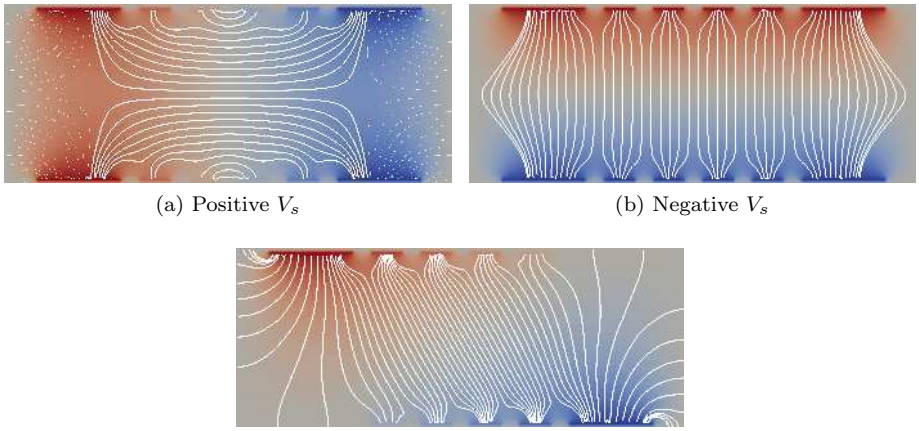

(a) Positive V_s (b) Negative V_s

(c) $V_s = 0$

Figure 4.15.: Configuration of the biasing potential (and field) in horizontal, vertical and an intermediate position.

however, is governed mainly by the overall resistance from first to last electrode line. What is important for the actual potential within one phase shifter is solely the variation of resistances $R_{(n,n+1),s}$ on one sheet s, $\sigma_{(n,n+1),s}$. A sample of six sets of four sheets (in total 24 electrode sheets) was taken and the resistance values between all electrodes were determined (Table 4.5). The values depend on the distance between sheets and on the width and thickness (variation) of the resistive paste applied across the lines.

It is clear from Table 4.5 that overall repeatability is not yet given. However, the technology used is in line with standard flexible substrate technology and it can be assumed to be more of a question of equipment and routine to reduce the overall variability. Individually however, the standard deviations σ are below 30 % already for the most part. This means, that with few exceptions, adjacent resistance values differ by no more than 30 %.

The final sheet design is depicted in Fig. 4.16. Two main derivates are discussed: (1) varying the shape of the individual electrode lines in order to suppress stripline modes and (2) varying the "wiring", i.e. how the voltage is fed onto the sheet and into the phase shifter respectively.

This can be summed up as follows:

1. Two electrode shapes are considered: on the one hand, a simple design with two bias lines of equal width at the edges and four smaller lines of equal width in the middle. On the other hand, a more complex design, where the width of the bias lines is stepwise modulated in order to suppress stripline modes propagating between the bias lines and the waveguide wall, which acts as a ground plane. As measurements that are summarised in the following section show, these stipline

Sheet			Set Number 2	5	7	8	6	3
1	$\bar{R}$	MΩ	0.898	1.896	1.380	1.816	1.360	2.776
	σ	%	13	17	29	17	14	11
2	$\bar{R}$	MΩ	1.554	4.506	1.200	4.450	1.180	4.160
	σ	%	26	27	24	37	12	15
3	$\bar{R}$	MΩ	0.830	1.512	0.778	1.416	0.600	1.174
	σ	%	29	18	28	28	35	14
4	$\bar{R}$	MΩ	0.448	1.048	0.320	0.780	0.780	0.784
	σ	%	65	18	21	10	21	10

Table 4.5.: Average values and standard deviation of the resistance values between lines on 24 fabricated electrode sheets. Sheet 4 of Set 2 had $R_{(3,4)}$ short circuited (indicated in red).

(a) Without filter structure on centre strip lines

(b) With filter structure on centre strip lines

Figure 4.16.: Final layout version 3.16 of the electrode sheets fabricated in 2015. Variations with and without contact ribbons were fabricated. Legend: carrier in brown, Titanium electrodes in grey, Gold pads in orange and resistive paste in black.

modes do not seem to couple very well with the dominant quasi-TE01 mode in the phase shifter and are therefore negligible.

2. Three possible ways of connecting the electrodes with the outside world are considered: The first is direct connections leading to six pads on the outer contact pad. This allows contacting each electrode even if no internal resistive network is present or if it is broken. The second consists in two connections to the larger,

outmost bias lines and two pads on the contact pad. While individual contacts are not an option anymore, the width of the through hole in the waveguide wall can be significantly smaller in this case. And finally the third provides contact pads on the inside of the phase shifter which are contacted by soldered wire leads. Their capacitive impact is compensated for by the placement of the filling chimney.

Both variations can be easily tested in the split-block structure used for verification as shown in Figure 4.17.

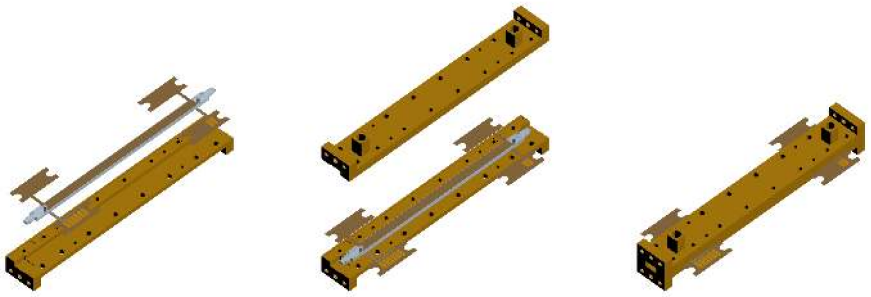

(a) Electrode sheets glued onto container (b) Fit into split-block bottom (c) Split-block cover, container aligned via chimneys

Figure 4.17.: Assembling phase shifter and split-block: the container with electrode sheets (a) is inserted into the split-block (b) and aligned by the chimney holes which serve as LC filling channels (c).

4.3.4. Fabrication Process

The final phase consists in assembling the LCPS using a five step procedure depicted in Figure 4.18.

The process steps are summarized below:

Step 1 The Rexolite containers are fabricated, assembled and glued at GEWO Feinmechanik GmbH, Wörth/Hörlkofen, Germany (GEWO) and shipped to LRT (Chair of Astronautics (Lehrstuhl für Raumfahrttechnik, LRT)).

Step 2 At Chair of Astronautics (Lehrstuhl für Raumfahrttechnik, LRT) (LRT) the electrode sheets are assembled and if applicable soldered with wires, then isolated und subsequently attached to the container by transfer on adhesive tape (3M 300LSE, 50 µm). The flanges are attached. Then, they are shipped back to GEWO.

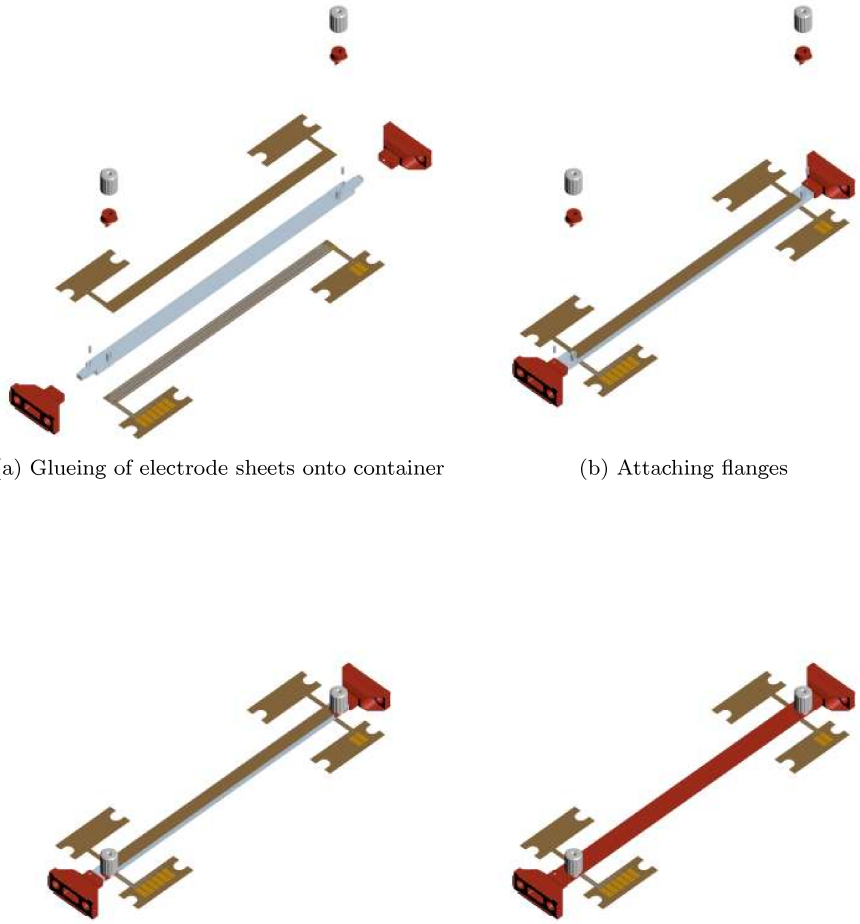

(a) Glueing of electrode sheets onto container

(b) Attaching flanges

(c) Fitting filling nozzels with caps

(d) Depositing Ag/Cu waveguide wall

Figure 4.18.: Assembling the phase shifter for electroplating: the container with electrode sheets (a) is fitted with flanges using press-fit and alignment pins for locking (b). (c) Filling nozzles with caps are attached. Prepared accordingly, (d) a seed layer (Ag) is evaporated and the Cu wall is desposited.

Step 3 At GEWO, the filling nozzles are attached and fixed by glueing using Zeiss Glue 56. The assemblies are then shipped to Otto Klobe & Sohn GmbH, Kaufbeuren, Germany (Klobe).

Step 4 At Klobe, a silver layer is deposited using multiple evaporation runs which each can significantly heat the device. At a time, 120 nm to 140 nm Ag are deposited.

3 to 4 layers are deposited. The technique will be described in further detail in upcoming LRT publications. For the final step, the assembly is shipped to Galvano-T GmbH, Windeck/Rosbach, Germany (Galvano-T).

Step 5 At Galvano-T, a layer of Copper is deposited by means of electroplating. The overall thickness is subject to mechanical constraints and not specified here any further as the skin depth δ_s is below 450 nm even at the lowest operating frequency and at a penetration depth of $d \approx 2.0\,\mu\text{m}$ the current density has dropped below 1 %. During the process, the LC container is sealed and typically filled with de-ionised (DI) water. Now, the device is ready for LC filling. Note, that steps 4 and 5 are summarised as one step in Figure 4.18.

Figure 4.19.: Photographs of an assembled and electroplated phase shifter (2015). LC filling tube, electrode contact pads and flanges are visible.

A finished, electroplated LCPS is shown in Figure 4.19 alongside an example of a failed device.

Depending on the actual process which is still under development, the total weight of the LCPS may vary. A typical total weight would be 23 g out of which approximately 10 g are the attached copper parts (flanges and nozzles).

4.4. Lightweight Phase Shifter Measurements

4.4.1. Prerequisites

In order to carry out measurements in a controllable environment, two types of measurements are conducted routinely. Electrically biased measurements demonstrate the objective functionality. However, many failing parts might cause an otherwise well performing phase shifter to fail in an electrically biased measurement. To distinguish between plain RF performance and high-end functionality, a second type of measurement is routinely carried out: The magnetically biased measurement.

To this end, a large magnetised volume had to be provided. The phase shifters are typically very long ($l > 100\,\text{mm}$) and bulky (cross-sections in the range of up to $30 \times 30\,\text{mm}^2$). A large setup of permanent magnets had to be designed in order to meet this requirement and to provide a strong magnetic field of $B \approx 0.25\,\text{T}$.

Figure 4.20 shows the layout of this device, dubbed "Magneto": It offers a pivoting cage which carries a yoke with two strong, permanent magnets (courtesy Vacuumschmelze GmbH & Co. KG, Hanau, Germany (VAC)) with a pole piece attached to each of them.

4.4.2. Issue of Electrode Sheet Shape Consistency

The phase shifter design was conceived with electroplating in mind. As such, too little attention was put on the mechanical tolerances between container and waveguide walls. The assumption was, that due to the metal deposition directly onto the container, the air gap between container and wall would be exactly zero.

This turned out to be a false conclusion as the first set of measurements proved – at least in the split-block waveguide. While the matching was largely fine, the IL took on random values as Figure 4.21 shows. Insertion loss would vary wildly between somewhere below the IL in case of no electrode sheets inserted and more than 20 dB.

The magnitude of the effect was surprising – as was its inconsistency (see Figure 4.22). It is assumed that because the combined height of container and electrode sheet was approximately 50 µm smaller than the waveguide height, due to fabrication tolerances, the electrode sheet was not fixed in height direction and therefore may have alternated contact between container and wall. At this moment, the assumption of an electrode perpendicular to the RF-field was broken and ohmic losses occured.

It was then the question if this was the effect of the increased distance between the electrodes and the waveguide wall. To find out, a spacer sheet was inserted – filling the air gap – and increasing the distance from electrode to wall from 50 µm to 100 µm (nominally). In the reference case, the distance of the electrodes to the wall was set to 50 µm by inserting a spacer between container and sheet (see insets of Figure 4.22). As a result of the additional 50 µm between electrodes and wall the IL increased by more than 2 dB (see Figure 4.22). This led to a revision of the design: the height of the testing split block no longer allows a tolerance in height. In the revision put to test in the following section, it is set to fit. As a result, this kind of malfunction is no longer observed. In the following section, the residual losses due to the electrode sheets will be analysed and discussed.

4.4.3. Study of Losses Induced by Electrode Sheets

As discussed previously, introducing electrode sheets into the phase shifter comes at the price of higher IL. This is on the one hand due to the dielectric losses induced by the polyimide sheet and the resistive paste. On the other hand, the electrodes themselves may induce losses. The way these losses manifest themselves can be twofold: coupling of power out of the TE_{01} mode into highly lossy stripline modes, as discussed in the previous section, or metallic losses in the electrodes that play a minor role due to their strong capacitive coupling with the waveguide walls. The design attempt aimed at the latter effect: the thin polyimide sheet sets the electrodes at such a small distance to the waveguide wall, that their momentary potential is practically in phase with the waveguide wall. As a result, the TE_{01} mode experiences something like a rough

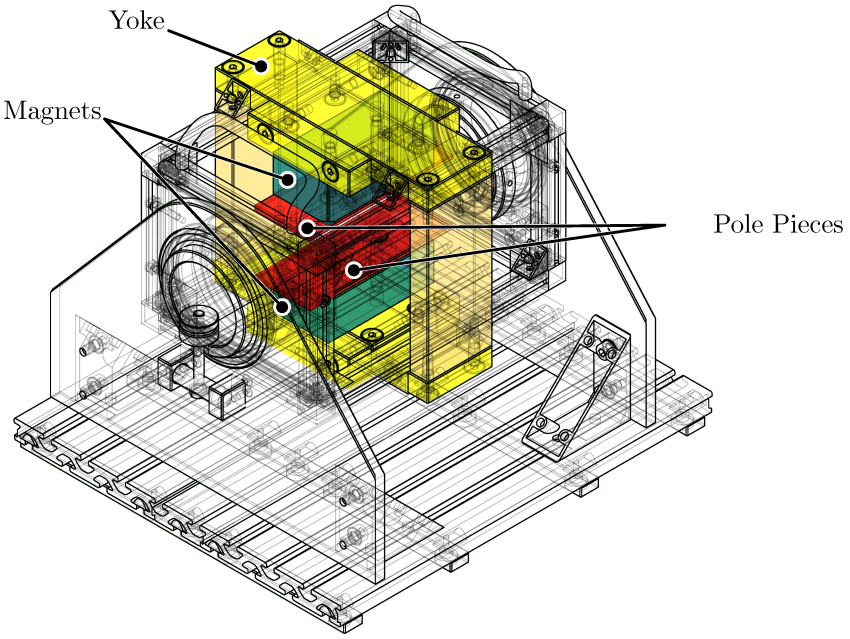

(a) Isometric view

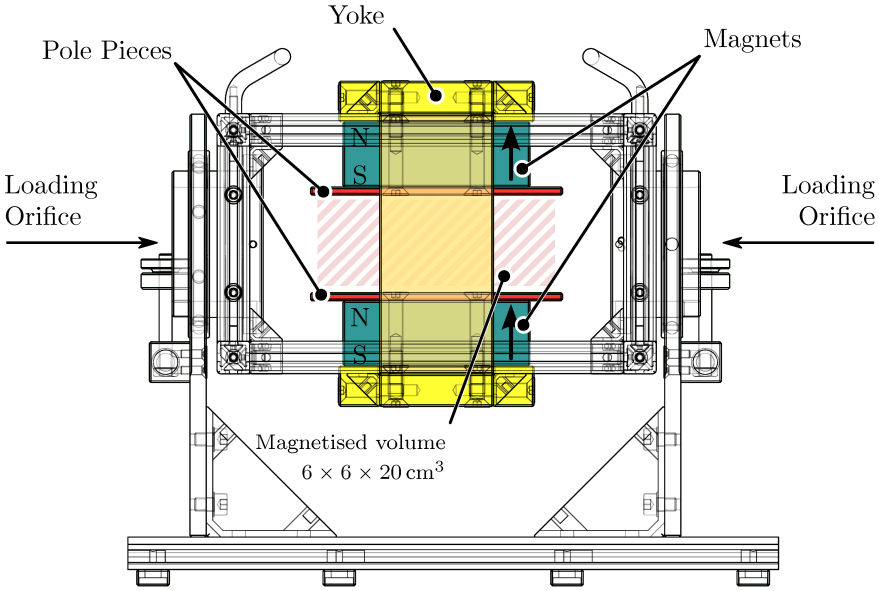

(b) Side view

Figure 4.20.: The magnetic biasing device (dubbed "Magneto") to quickly and readily orient LISA_{ES} phase shifters without electrical bias

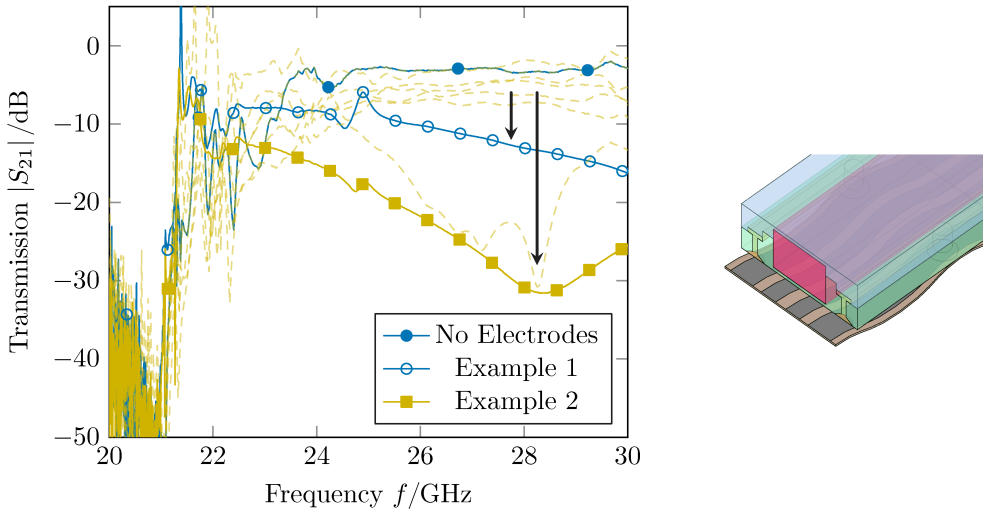

Figure 4.21.: Non-reproducible excess in IL supposedly due to deformations or wrinkeling of the electrode sheets illustrated by example

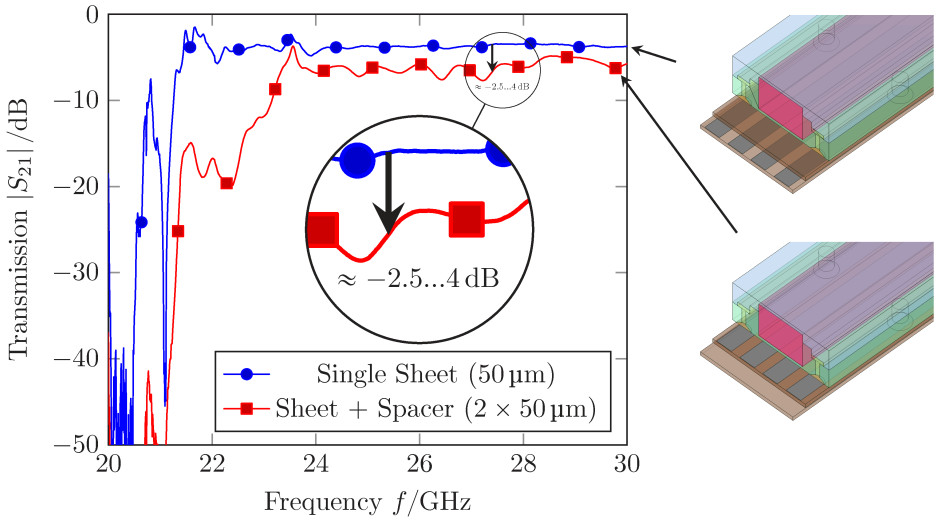

Figure 4.22.: Effect of electrode-to-wall distance on IL by inserting a spacer sheet into the waveguide

wall. This in turn obviously induces additional IL but can be managed to stay below a certain threshold.

In turn, a batch of five electrode sheet pairs is tested against a bare container that

contained no LC cavity, hence was entirely made of Rexolite, called a "dummy" for its lack of functionality. Figure 4.23 shows two measurement results. One is taken with only the bare dummy with no sheets at all. At the time, unfortunately no bare sheets (i.e. sheets without electrodes, contacts or resistive network) were available. So, individual distinctions as to which part of the sheet is responsible for how much of the induced losses, could not be carried out. The other measurement is taken with two electrode sheets (specimen No. 708-611) of 50 µm thickness. Clearly, the IL increases but the magnitude of this increase is surprisingly low, given how complex a shape is inserted into the waveguide. Especially surprising is the fact that the sheet already has the resistive network printed onto it.

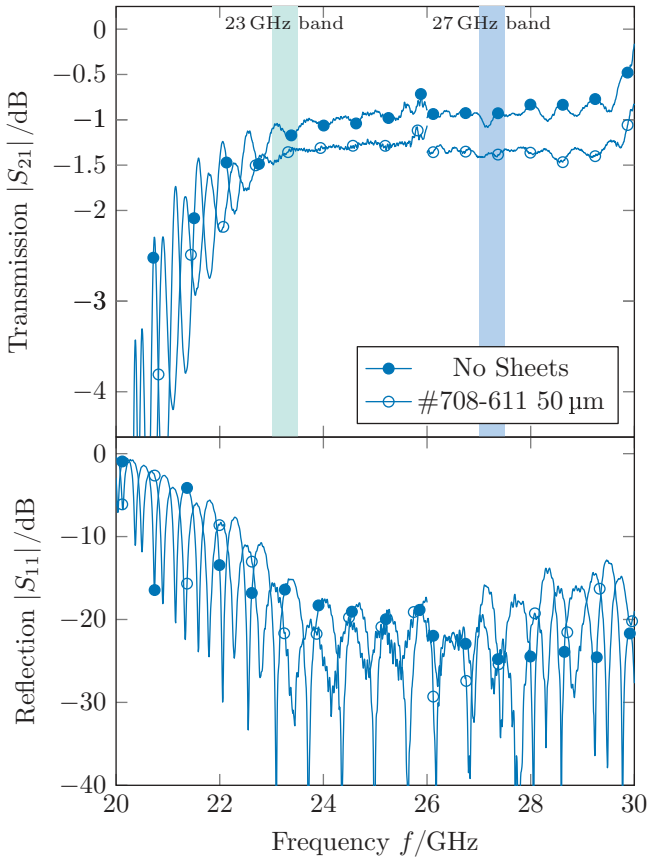

Figure 4.23.: Example of the measurement of a bare Rexolite dummy (full container without cavity) compared to a Rexolite dummy equipped with two sheets No. 708-611. The average IL is determined by taking the average over each band at 23 GHz to 23.5 GHz and 27 GHz to 27.5 GHz

In order to compare the five different sheets, the averages over the two frequency

bands in question (23 GHz to 23.5 GHz and 27 GHz to 27.5 GHz, respectively) are taken and the results are shown in Table 4.6. The bare dummy itself accounts for an IL of around 1 dB. It is increased by typically around 0.3 dB in the 23 GHz and 0.4 dB to 0.6 dB in the 27 GHz band.

		23 GHz		**27 GHz**	
Sample	d/µm	IL_{avg}/dB	$IL_{avg} - IL_{ref}$/dB	IL_{avg}/dB	$IL_{avg} - IL_{ref}$/dB
Dummy	0	−1.12	—	−0.94	—
Sample	d/µm	IL_{avg}/dB	$IL_{avg} - IL_{ref}$/dB	IL_{avg}/dB	$IL_{avg} - IL_{ref}$/dB
708-610	25	−1.60	−0.48	−1.40	−0.45
708-611	50	−1.44	−0.32	−1.61	−0.66
708-612	50	−1.39	−0.27	−1.35	−0.41
708-642	50	−1.33	−0.21	−1.56	−0.61
708-643	25	−1.36	−0.24	−1.27	−0.33

Table 4.6.: Comparing the average IL in each band with the reference case (no sheets, "Dummy"). The additional IL due to the sheets is displayed and typically below 0.5 dB at 23 GHz and below 0.67 dB at 27 GHz. No clear trend can be identified in terms of the sheet thickness.

There is no clear winning candidate to be identified. All sheets, even the 25 µm sheets perform well but over both bands none can show a clear advantage. As a result, no more 25 µm sheets were produced. Their supposed advantage of introducing a smaller volume of lossy dielectric and a smaller electrode-wall distance did not reflect in the measurement results. This may be due to the wrinkeling problem discussed in the previous section. Furthermore, they are very fragile.

Amongst the 50 µm sheets, the layout with the simple electrode shape, i.e. without filter structures was chosen for further consideration. It seemed unnecessary to complicate the fabrication process by imposing stronger than necessary requirements on the photolithography process. The given layout can be reliably fabricated even with standard printed circuit board (PCB) processes.

Given the small influence of the electrode shape, it can be speculated that most of the losses actually stem from the volume of lossy dielectric introduced here. As Pyralux AP [DuP09] is not the only flexible substrate on the market, future designs could use materials of lower $\tan\delta$.

Concludingly, it could be said that the sheet layout, the material choice and the fitting were sufficiently tested for a full prototype test.

4.4.4. Experimental Verification

Consequently, a prototype was fabricated in 2013 along with a split-block brass waveguide to test the containers and electrode sheets. The setup is shown in Figure 4.24. The LC filling channel was just a short stub on the side with a pin to close it inserted

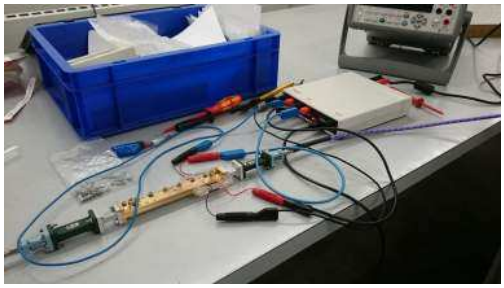

Figure 4.24.: Phase shifter connected to PNA-X for measurement. Electrical biasing is done using the driver box developed by IMST GmbH

from the top. This proved insufficient as will be shown henceforward. However, it was sufficient to obtain the proof that the concept worked.

The shortcomings of the 2013 revision are identified in the next section and lead to an improved design in the 2015 revision. The container layout introduced earlier in this chapter is the 2015 revision. The performance is analysed in terms of static properties as well as the dynamic behaviour.

2013 Container Version

In this study [Wei+13a; Wei13; Wei+13c], the set of previously presented electrode sheets is combined with a LC container filled with GT5-26001. Each combination is characterised using magnetic biasing first. To this end, the assembly is inserted into the magnetisation volume of "Magneto" and let rest for several minutes with the magnets either left-right (horizontal alignment) or above-below (vertical alignment) of the phase shifter. This way, a very homogeneous LC director field is obtained and the maximum performance can be observed.

The phase $\sphericalangle S_{21}$ in both cases (horizontal and vertical alignment) is subtracted from each other to obtain the differential phase shift $\Delta\Phi$. There is an ambiguity as the value of $\sphericalangle S_{21}$ is the 360° modulo of the actual phase βl. The data are confirmed live during measurement by looking at the instantaneous phase on the Vector Network Analyser (VNA) display.

In a second measurement, each combination is electronically biased using the driver box developed by IMST GmbH introduced earlier (cf. Figure 4.11 on page 74). Steering is now achieved by an electric field. Naturally, it is not as homogeneous as the magnetic field because it is created by only a finite number of discrete electrodes. This reflects in a lower phase shift $\Delta\Phi$.

In both cases the maximum IL is extracted and the figure of merit is determined as

$$\mathrm{FoM} = \frac{\Delta\Phi}{\max \mathrm{IL}}, \tag{4.20}$$

a function of frequency.

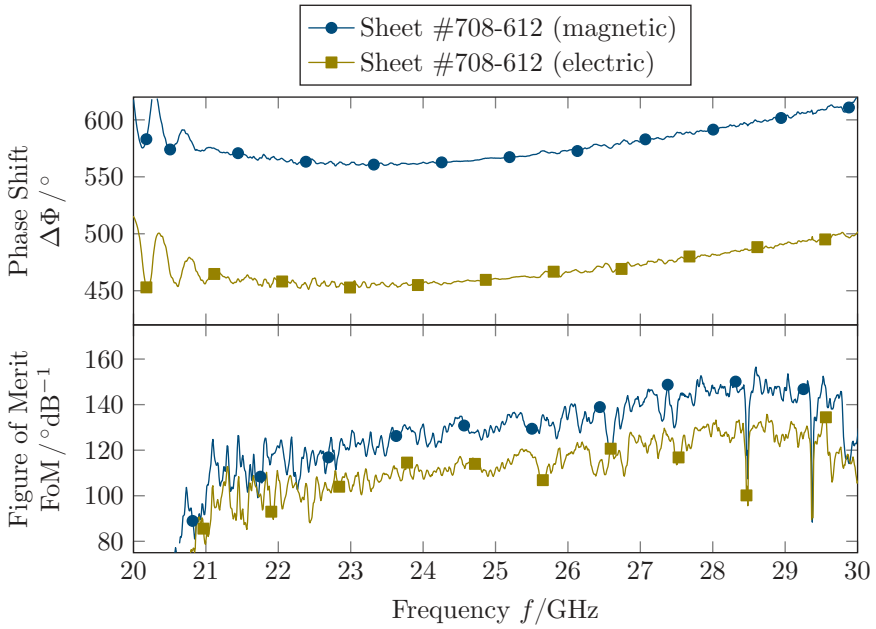

Figure 4.25.: Magnetically and electrically biased performance using sheet pair No. 708-612

Figures 4.25 to 4.27 show the resulting phase shift $\Delta\Phi$ and figure of merit for both the magnetically and the electronically steered case. Due to the higher $\Delta\Phi$ in the magnetic case, the figure of merit is generally higher in the magnetic case.

Still, even in the electrical case, the figure of merit exceeds an figure of merit of 120 °/dB in the 23 GHz band. The figure of merit increases almost monotonically (ignoring the noise) to more than 160 °/dB which is excellent, given the high degree of integration of the phase shifter presented here.

Only one set of sheets (No. 708-610) failed at the electrical test. The IL in this case was exceptionally high which resulted in a comparatively very low figure of merit of only approximately 100 °/dB as shown in Figure 4.28.

The matching is acceptable at approximately −15 dB but it can be observed in Figure 4.29 that the matching leaves a lot to be desired. The reason for this turned out to be a design error that stayed undetected until measurement, where in all models, the permittivity of the sheets was set to 1.0. This illustrates the delicacy of the design: the permittivity only a small fraction of a total height of 100 µm of the cross-section has a large influence on the device's matching.

Another problem was identified during the measurements: the mechanism to fill and seal the cavity turned out to be unreliable, releasing LC into the waveguide over time. The reasons for this behaviour were manifold: at the time, the seam was glued using Rexolite adhesive which produces a porous, capillary-filled volume which allowed the

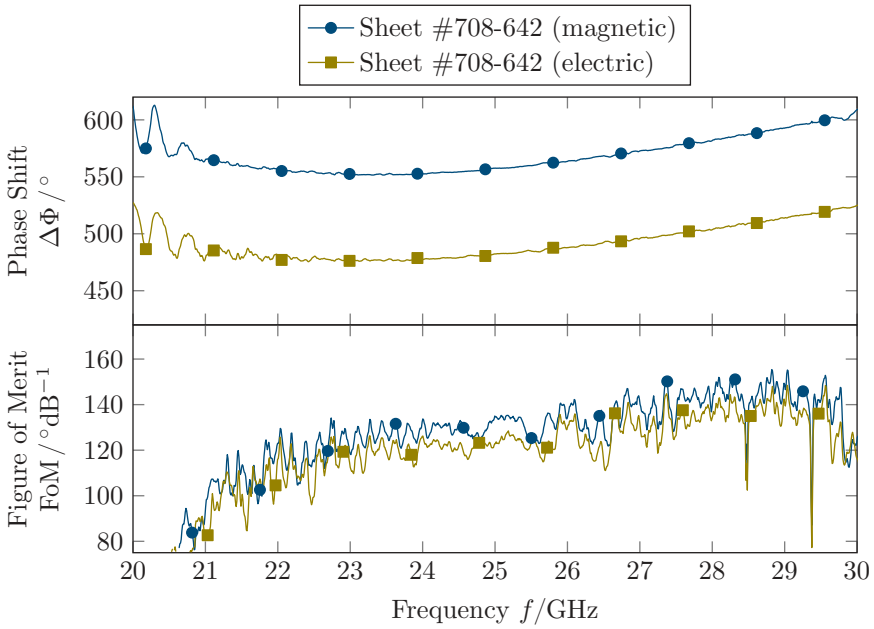

Figure 4.26.: Magnetically and electrically biased performance using sheet pair No. 708-642

LC to creep. Furthermore, the geometry of the glueing seam in combination with imperfections such as the porosity caused the glueing seam to fail or the cover part to break. Also, the filling nozzle was a mere hole in the container side wall. Sealing off this hole after filling proved practically impossible once LC had been in contact with the surface of the container due to the strong wetting effect and creeping properties of the LC.

A solution to the latter (the sealing problem) was the introduction of the chimney through which the LC can be inserted. A probable solution to the porous glueing seam problem was replacing of the Rexolite adesive by Zeiss Glue 56, an epoxy-based two component glue which has much lower viscosity and gas-free curing properties while maintaining an acceptable $\tan\delta$ (see Chapter 3).

With the error in the model identified and the solution to the leaking filling mechanism, finally a major redesign of the taper section was carried out throughout 2014 which led to the new 2015 revision of the phase shifter. This revision will be discussed in the following section.

2015 Container Version

With the changes made and a new set of sheets, the 2013 measurements were repeated. This time though, the main objectives were showing good sealing properties and ease

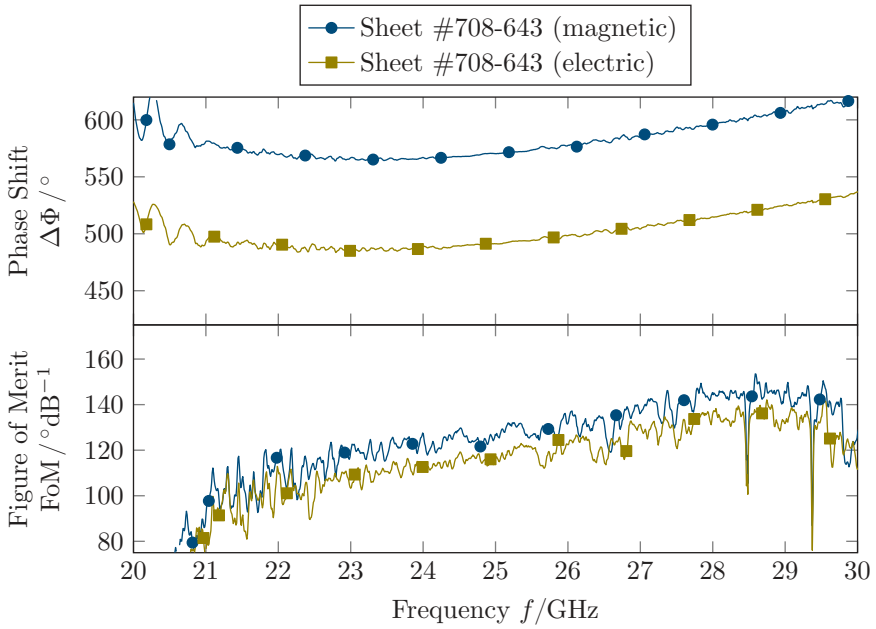

Figure 4.27.: Magnetically and electrically biased performance using sheet pair No. 708-643

of filling. The matching had been improved by revising the flange and electrode sheet positions and correcting the model. The effect is most visible in the electroplated phase shifter measurements shown in the next section. The improved matching in place, the dynamic behaviour of the phase shifters was characterised using the continuous-wave mode of the PNA-X at 23.75 GHz for the split-block which had slightly degraded matching compared to the electroplated design.

Again as before, the first set of measurements is carried out using fully magnetic biasing with the "Magneto" setup. The results of a representative selection of measurements are shown in Figure 4.30 where the top graph shows the switching from vertical to horizontal orientation and the bottom graph vice versa. The phase values are normalised to the respective onset which makes the visual comparison easier.

The first observation is that the switching process starts with a small delay but develops a very steep slope. Once 90 % are reached, the curve goes into saturation. The last part from 90 % to 99 % takes about 5 times as long as the slope from 10 % to 90 %. Looking at the 10 %–90 % rise time Δt, the results are very coherent no matter what direction the switch takes place.

A second observation concerns the saturation level of the phase. As the phase is normalised, no accurate information is available with respect to the start phase. It seems – and this has not been ultimately clarified – that the level of saturation can vary slightly, causing the start phase to vary. In the experiment for practical reasons,

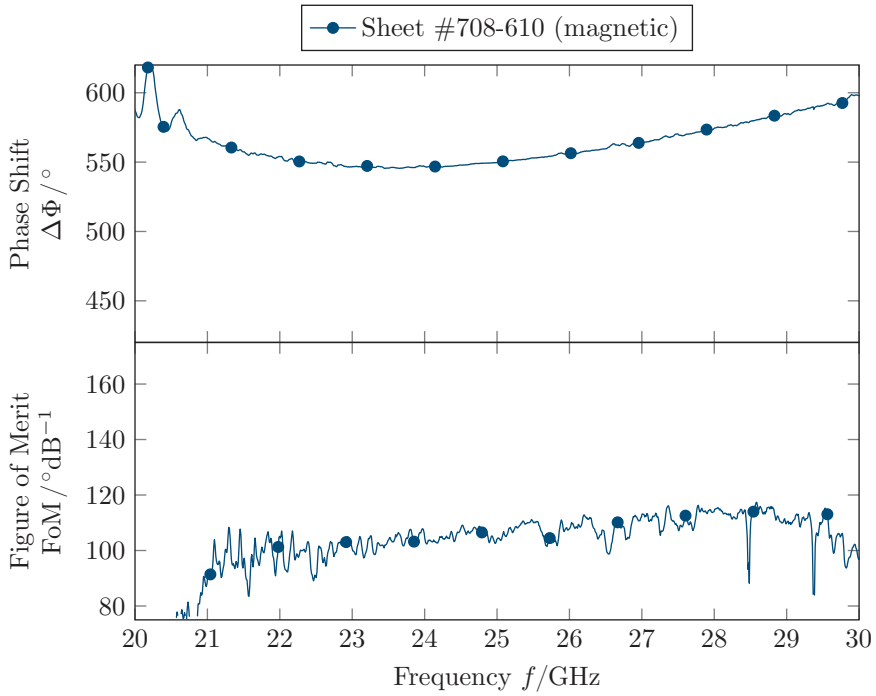

Figure 4.28.: Performance of a magnetically tuned 25 µm sheet (708-610). Thinner sheets, while intrinsically better in terms of losses are much harder to align and flatten. So the performance is strongly degraded. Electrical tuning did not work with this sheet.

after recording a horizontal-to-vertical switch, the opposite direction was recorded and so forth. The device was left to rest for several minutes in one state before switching back. However, as is obvious from Figure 4.30, this did not prevent a variation in saturation phase. A solution to this problem cannot be presented at this time.

A third observation is that, while both directions show similar 10 %–90 % rise times Δt, the 10 %–90 % phase shift $\Delta\Phi_{10\%}^{90\%}$ is slightly lower. Furthermore, the curve shape is slightly different, with a more pronounced pinge at the onset of the switching process (more instant reaction) and the saturation process takes much longer – to the extent that its end cannot be seen in the recorded data which was as long as 270 s, i.e. 4.5 min. In the magnetic biasing case, the 10 %–90 % rise time always took on values of $\Delta t \approx 30$ s.

For the second set of measurements the electronic driver box developed within LISA_{ES} by IMST GmbH is used for biasing. In this case, less sheet pairs could be used as in some cases electrodes or contact lines were broken. The driver box provides two symmetric voltage sources with respect to common ground. Common ground is connected to the waveguide case. The voltage source $\pm V_{\text{ref}}$ is fixed to a predefined

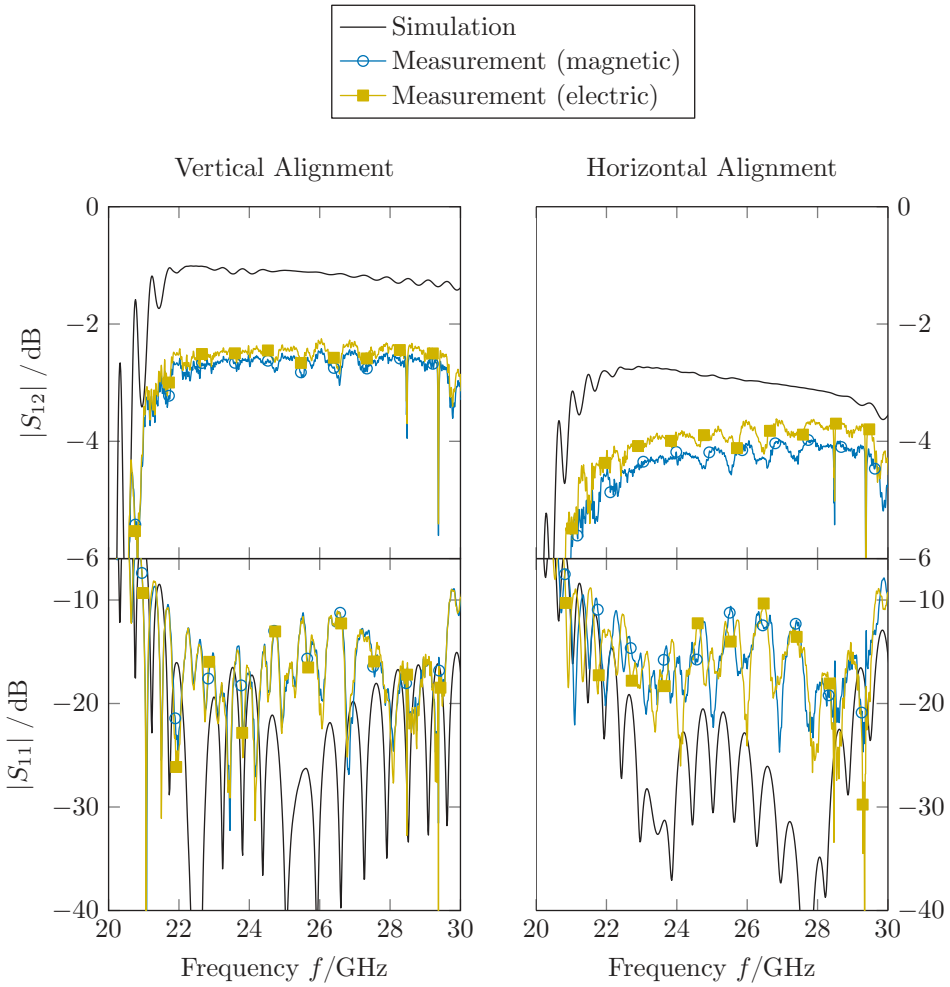

Figure 4.29.: Discrepancy between simulation and measurement due to modelling error and hence wrong taper geometry. The simulation results with the (wrong) model are shown in black. $|S_{12}|$ disagree slightly because some loss mechanisms (ohmic losses in electrodes) are difficult to simulate. Matching $|S_{11}|$ is strongly degraded.

value, usually $\pm 164\,\mathrm{V}$. The other voltage source, $\pm V_s$ is variable and can be tuned over the whole range from $\pm 164\,\mathrm{V}$.

Each source pair is connected to diametrally opposing electrode contacts as shown in Figure 4.12. In this way, the electric DC field can be set quasi-continuously from horizontal to vertical by driving V_s from one extreme $\pm V_{s,\max}$ to its inverse $\mp V_{s,\max}$.

Figure 4.31 displays the results. Notably, the horizontal to vertical switching dis-

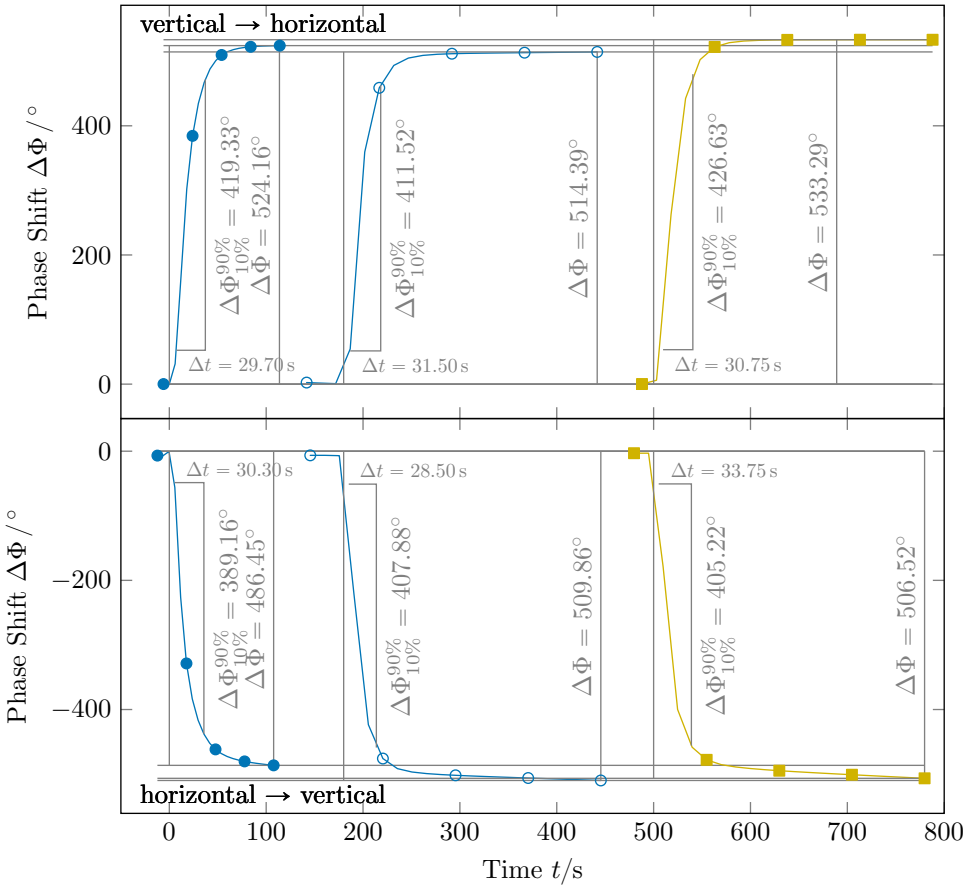

Figure 4.30.: Magnetic steering: phase shift responses of a phase shifter with electrode sheet No. 708-770 to switching the magnetic bias field orientation for a continuous-wave excitation at 23.75 GHz. The top graph shows switching from vertical to horizontal orientation, the bottom graph shows switching from horizontal to vertical. Overall measured phase shift, 10 %–90 % phase shift, and rise time respectively are displayed.

played in the bottom part of the figure shows performance not far off the magnetically biased results discussed previously. The 10 %–90 % phase shift is slightly smaller at $\Delta\Phi_{10\%}^{90\%} \approx 370°$. This can be explained with the reduced overall maximum phase shift, which is due to the non-homogeneous biasing field.

The most remarkable difference to the magnetic case is the dramatically increased switching time Δt of more than 200 s in the vertical to horizontal switching case. The time obtained in the first attempt is not representative, as the saturating phase is cut-off too early. Even in the second attempt, a large portion of the switching process

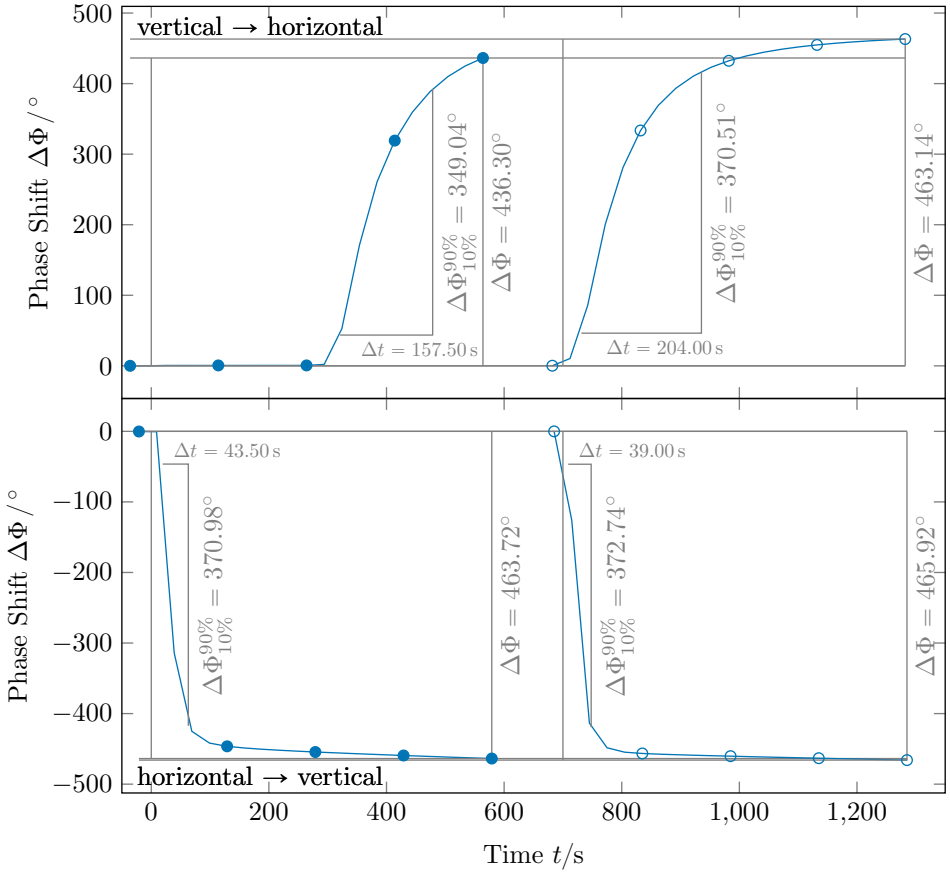

Figure 4.31.: Electric steering: phase shift responses of a phase shifter with electrode sheet No. 708-770 to switching the electric bias field orientation for a continuous-wave excitation at 23.75 GHz. The top graph shows switching from vertical to horizontal orientation, the bottom graph shows switching from horizontal to vertical. Overall measured phase shift, 10 %–90 % phase shift, and rise time respectively are displayed.

seems not to be recorded.

This effect is easily explained by the fact, that the effective electric field magnitude is two times lower in the horizontal orientation than in the vertical orientation. This in turn leads to an increase in switching time of at least the square, i.e. at least a factor of 4. In reality, as can be easily seen, a factor of 5 to 6 seems to be more realistic.

With this measurement, the project goal to prove a sealable, mechanically robust, electrically performant LC phase shifter with electrical biasing and a minimum of 360° total phase shift was finally reached. The performance however, was not as good as

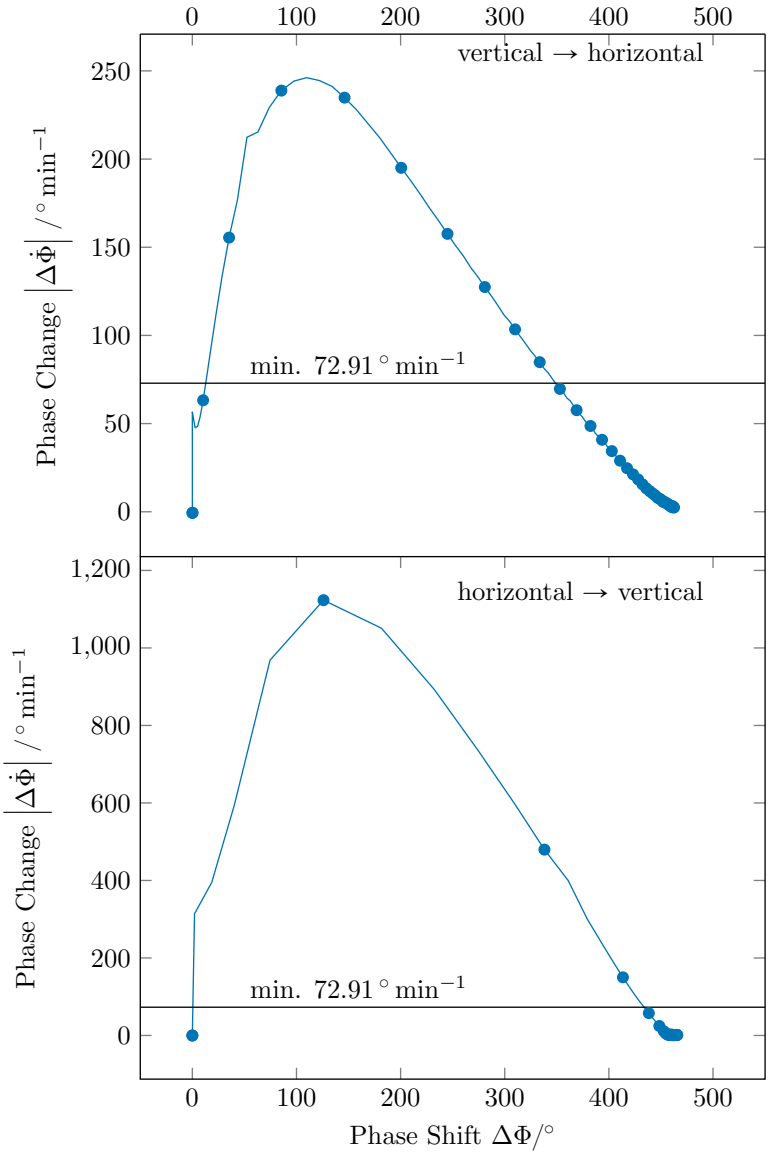

Figure 4.32.: Phase change per minute as a function of momentary differential phase based on the slowest electrical switching observed in Figure 4.31 set into perspective with Table 4.1

anticipated initially. While matching is overall very good, the IL is still larger than 1 dB and 3 dB, respectively.

The switching time, especially in the vertical-to-horizontal switching direction, is extremely long. This is not a problem for tracking in general, as Figure 4.32 shows, but at the instants where switching occurs, i.e. once the maximum differential phase shift is reached. As will be discussed later, unfortunately, no array tests could be carried out. Apparently, the fabrication process of the electroplated (i.e. final form) phase shifter proved to be prone to errors of which some would entirely destroy a device.

4.4.5. Electroplated Phase Shifter

(a) No. 708-768 (b) No. 708-772

Figure 4.33.: Device Under Test No. 708-768 is magnetically functional though lacking electrical functionality – note the missing contact pads on the lower left side. No. 708-772 was fabricated with contact stubs without pads. The phase shifter is non-functional due to a cleavage in the electroplated wall, on the left edge near the middle.

After the functionality of the phase shifter containers (or cores) had been proven, a batch was sent off for production. This included the final steps described in Section 4.3.4: assembly and masking, seed metallisation and electroplating. Several small and rather mechanical issues caused the electroplating solution to crawl into the structure, apparently damaging the electrodes (despite them being made of Titanium) and caused partial and even full electrical dysfunctionality. Therefore, the measurements

presented in this section show magnetic biasing only. Examples of two electroplated phase shifters are shown in Figure 4.33.

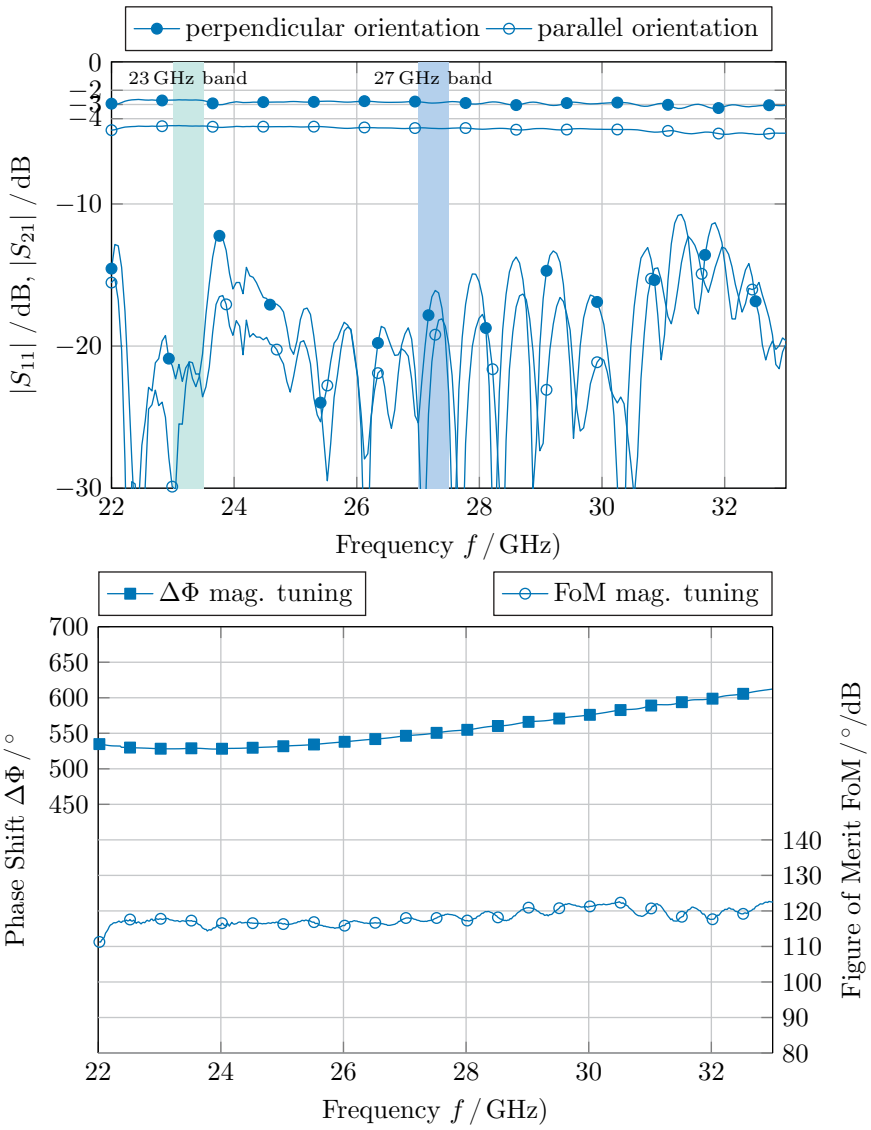

Figure 4.34.: Magnetically biased static results of electroplated phase shifter using electrode sheet pair No. 708-768

The drastically improved matching is clearly visible in Figure 4.34 and 4.35. Special attention was payed to improving the matching in the lower, 23 GHz band, which

failed to meet the expectations in the 2013 version of the phase shifters. The work of designing and optimising the taper section was carried out by Dr. Gehring, Airbus Defence and Space (Airbus DS).

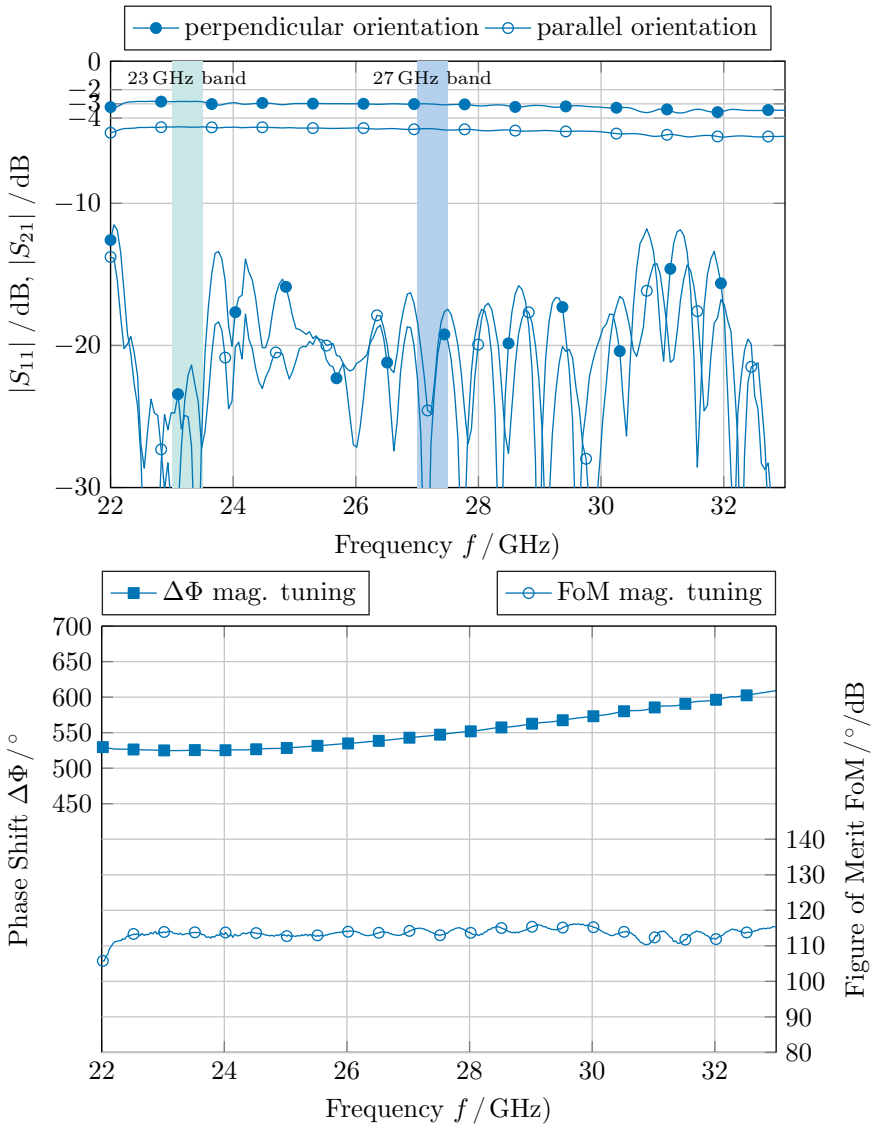

Figure 4.35.: Magnetically biased static results of electroplated phase shifter using electrode sheet pair No. 708-767

Both results show that the matching in the 27 GHz band can still be improved, but

meets the minimum requirement of $S_{11,22} \leqslant -15\,\mathrm{dB}$. In terms of the maximum phase shift, the electroplated phase shifters perform equally well as their split-block counterparts. The overall figure of merit is slightly below $120\,^\circ/\mathrm{dB}$ if the whole measurement assembly is considered. If the transitions at the input ports are de-embedded, the figure of merit increases significantly.

The main problem remains visible: the IL remains at more than 2 dB despite the high degree of integration and the fact that the walls of the waveguide are now composed of a layer of silver surrounded by copper. This should, in theory, reduce waveguide losses compared to the brass split-block used before. The only conclusion that can be drawn from this observation is that the largest part of the IL is due to dielectric losses.

If one looks back at Figure 4.23, where both LC and glue were absent, the answer is that either of these materials are responsible for the additional losses. In the case of GT5-26001, the maximum loss angle is obtained in the horizontal biasing field orientation, where $\tan\delta_\perp \approx 7 \times 10^{-3}$.

The properties of the glue are assumed to be $\varepsilon_r = 3.1$ and $\tan\delta \approx 1 \times 10^{-2}$ in this prototype. If a glue can be found with better RF performance, also the overall phase shifter performance and hence the figure of merit can be drastically improved.

At last, one observation concerning the balance of IL over steering states is made: horizontal and vertical state exhibit a difference in IL of $\Delta\mathrm{IL} \approx 1.5 \ldots 2\,\mathrm{dB}$ which is inconvenient for array operation. As pointed out in [Gäb15], this can be circumvented by choosing a larger aspect ratio which would result in a reduced waveguide height. At this time and during this thesis, this question was dropped for reasons of feasibility: the height of the LC cavity had already been reduced by the fact that sheets alone would not seal the cavity. A further decrease in height would reduce the tunable fraction of cross-section area and hence reduce performance. However, it seems, this way has to be taken in order to decrease $\Delta\mathrm{IL}$ below 1 dB.

Concerning the dynamic behaviour, only magnetic measurements are available as discussed previously. Figure 4.36 shows a set of three recordings per switching direction.

In the case of horizontal-to-vertical switching (bottom graphs in Fig. 4.36) no significant difference to previous magnetically biased measurements is visible. The rise time is in the range of $\Delta t \approx 30\,\mathrm{s}$, the overall phase shift $\Delta\Phi \approx 530^\circ$ and the 10 %–90 % phase shift $\Delta\Phi_{10\%}^{90\%} \approx 420^\circ$.

In the opposite direction however (vertical to horizontal orientation), the rise time increases by a factor of 2 to $\Delta t \approx 60\,\mathrm{s}$. This may be due to the LCPS not being fully centered during measurement which resulted in a position further towards the magnets' edges. In turn, the magnetic bias field would be weaker and tuning therefore slower.

4.5. Conclusion

In this chapter, a K/Ka-band LC phase shifter for space operation was developed and characterised. The design underwent three major re-designs in order to address the numerous constraints posed by the scenario. For the first time, a non-planar phase

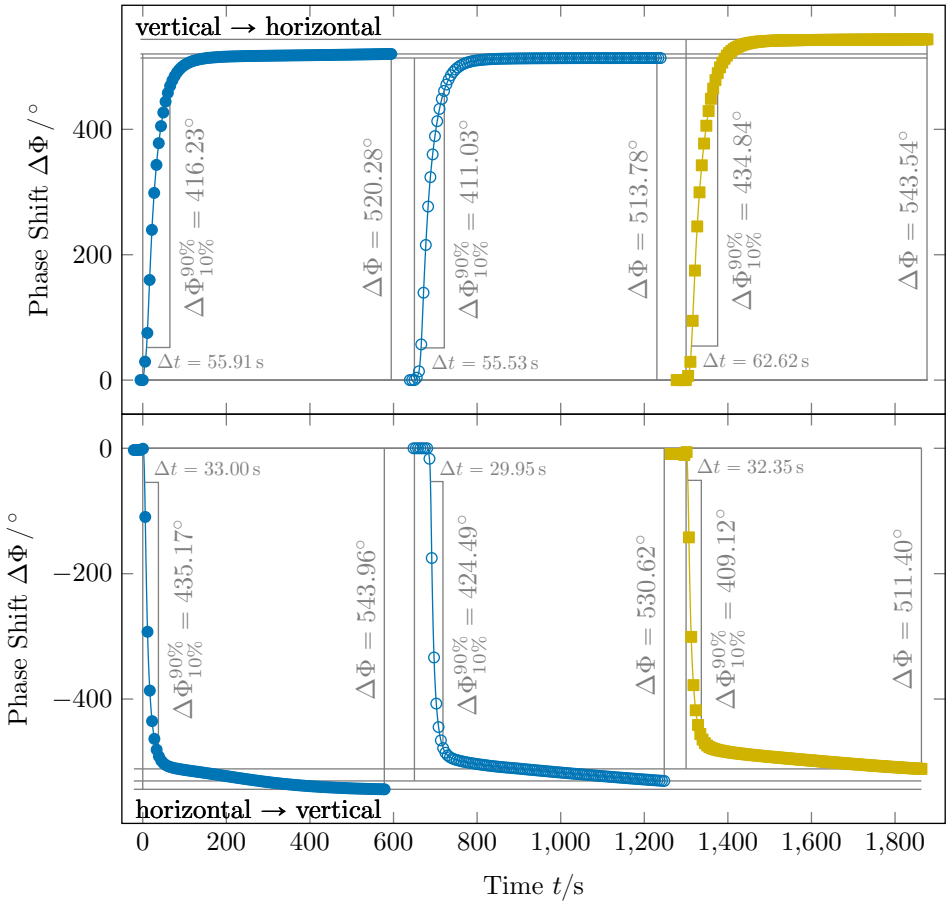

Figure 4.36.: Magnetic steering of electroplated phase shifter: phase shift responses of a phase shifter with electrode sheet No. 708-776 to switching the magnetic bias field orientation for a continuous-wave excitation at 23.75 GHz. The top graph shows switching from vertical to horizontal orientation, the bottom graph shows switching from horizontal to vertical. Overall measured phase shift and 10 %–90 % phase shift and rise time respectively are displayed.

shifter had to be sealed hermetically for use in a vacuum environment. Particular attention was paid to the weight and structural stability of the device. This is unusual for similar microwave devices. To the knowledge of the author such a high integration of materials, complex geometries and lightweight design has not been carried out so far.

Obviously, the project objective, namely the fabrication and characterisation of the

LISA_{ES} phased array could not be met. However, for the first time it was possible to design and fabricate a LC phase shifter in waveguide topology, study its static *and* dynamic, i.e. switching behaviour and obtain figures of its switching speed and IL. Within the frame of this thesis, no electrically functioning, electroplated device could be obtained. Nevertheless, the performance demonstrated – either in the split-block setup or the magnetically biased electroplated phase shifters – was excellent.

The particular scenario showed that in certain situations the most obvious drawback of LC in non-planar topologies, its slow response time, does not hinder its applicability. With less viscous and thus faster LC mixtures, quicker response and fewer perturbations at switch-back times could be acheived – typically at the expense of larger IL. On the other hand, this work shows the limits of LC technology: the liquid state of the material makes it harder to handle than most other technologies. And while other phase shifter technologies may induce larger IL or bandwidth limits, the amount of auxiliary effort, weight and volume in order to circumvent the issues described in this chapter, was considerably larger than initially believed.

Results from projects carried out in parallel to LISA_{ES} suggest that maybe rather than phase shifters, reconfigurable filters may acually benefit more from LC technology: here, the volumes are smaller, the typical operation regime involves less frequent switching events and the encapsulation in metallic cavities may very well reduce the sealing requirements.

5. Conclusion and Outlook

5.1. Contributions of the Thesis

Within the LISA_{ES} project, novel concepts combining light-weight construction, the use of low-loss polymers, and the integration of the biasing network have been designed and experimentally tested. The resulting phase shifter exhibits a high FoM $\gtrsim 120\,^\circ/\text{dB}$, full $> 360^\circ$ phase shift and a flat response over a wide frequency range (22 GHz to 28 GHz, i.e. $\mathsf{BW} \approx 25\,\%$).

The approach of the research project was ambitious and comprised many different technologies all included in one device. While this work focuses on the RF design of the phase shifter, significant scientific results and new engineering concepts have been brought forward by all involved partners. This said, especially the integration of light-weight construction techniques, like the use of electroplated waveguide walls, would not have been possible outside the frame of the LISA_{ES} project.

Furthermore, in this thesis it was possible to demonstrate reliable electronic biasing of the phase shifter and thus to verify the behaviour of so large a bulk of LC in a mm-wave device.

Switching times of 45 s in the fast direction and 210 s in the slow direction could be demonstrated in a fully electronic setup. Differential phase changes of up to $4.2\,^\circ\,\text{s}^{-1}$ (fast direction) and $20.8\,^\circ\,\text{s}^{-1}$ (slow direction) were demonstrated and set in context with the application scenario of LEO tracking. The suitability of LC technology for this kind of scenario could therefore be demonstrated.

An IL of typically better than 4 dB could also be demonstrated. This is of particular interest: on the one hand, in space applications heavy power duty is expected with transmit powers ranging up to the kW range. On the other hand, in the receive case the phase shifter loss plays an important role in the overall noise figure of the array. This will be discussed further in the outlook part of this chapter.

The second large contribution of this thesis is the characterisation of LC materials in resonant cavities at frequencies higher than 30 GHz and in the THz range.

A resonator design at 30 GHz and an extraction method based on the FEM were presented and discussed. The novelty in this case is the generality with which the extraction method can be employed: in addition to radial variations of the dielectric filling, the new method allows all geometries as long as they are cylindrical. This, for the first time, allows the full consideration of the filling hole necessary in LC characterisation methods.

The concept has also been taken one step further, demonstrating the new possibilities in a 60 GHz resonator concept. While the device did not allow for the complete characterisation of LCs, it presented a new concept to select suitable higher-order res-

onant modes for characterisation. In this case, the new FEM-based method not only allows for a much greater variety in geometrical parameters but also allows for the fast and responsive creation of mode charts which help finding good geometries, high Q factors, and a proper spacing of the resonance frequencies.

The second part of the study of material parameters presented data up into the FIR range to about 8 THz. It could be shown that many LC mixtures are highly transparent even at such high frequencies, while certain others showed absoption. In the case of the highly transparent mixtures, in accordance with theory, no or very low dispersion (i.e. change of permittivity over frequency) was found. This is an excellent basis for the use of LCs at even higher frequencies and inspired preliminary work in the range of 250 GHz which will be discussed further below.

5.2. Outlook

One of the main issues to be taken into further consideration is the aspect of noise introduced by the IL of the presented phase shifters. An IL of 4 dB corresponds to a contribution to the overall noise figure *before* the Low-Noise Amplifier (LNA) of a receive array of at least 4 dB or 2.5. In addition to degradation of the link, for example in the case of $\mathrm{LISA}_{\mathrm{ES}}$, due to the slow switching speed of somewhere between -1 and -3 dB, the SNR would further suffer if the IL cannot be improved.

Fortunately, there are several options. The main component, the LC, is still under development, so it is still possible that mixtures of low viscosity can be found that exhibit lower losses. The structural element, the container, could be fabricated from other materials that show lower loss. It could also be further perforated to include air/vacuum or foam compartments. The use of adhesives could be optimised by changing the mechanical structure of the phase shifters, thus reducing the parasitic effects of these very dissipative materials.

Last but not least, with lower viscosity and hence, faster switching, the overall length of the device could be reduced, leading to lower IL. This is true as well for LC with higher anisotropy, although the limit of what is possible should already be more or less reached in this respect.

The aspect of losses and noise in LC based arrays is already considered at this time ([Nic+17], submitted for consideration at EuCAP 2017). Further improvements in the mechanical structure, the use of auxiliary materials like adhesives and none the least the LC can be expected as the technological aspects already found their way into various other applications.

Considering the characterisation of materials at higher frequencies, the direction is mostly given: improve the Q factor of resonators at frequencies higher than 30 GHz by using higher order modes and use extraction methods similar to the one presented in this work. The eigen-permittivity method should be considered further in this regard, as it allows for the extraction of the material parameters directly which may come handy as the cross-dependencies of transversal and longitudinal field components become stronger.

Another very important aspect is the characterisation of LC in the THz range. The

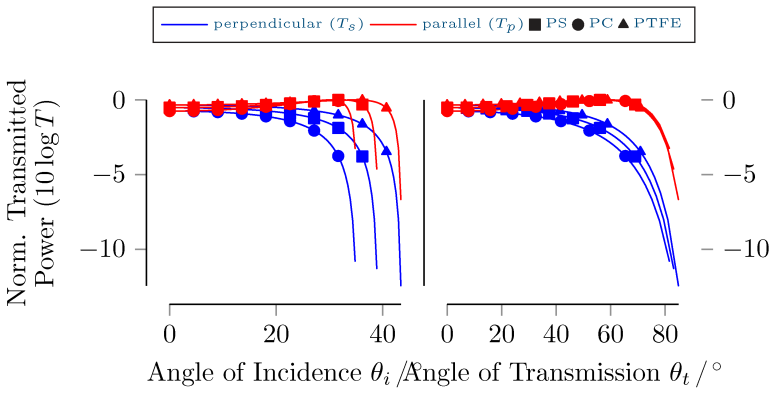

Figure 5.1.: Power fraction transmitted through a dielectric interface $\varepsilon_{r,1}$–ε_{Air} with $\varepsilon_{r,1} > \varepsilon_{Air}$ for several likely materials plotted both as a function of angle of incidence (i. e. array steering angle) and angle of transmission (i. e. apparent steering angle in the air). Both polarisations are considered separately.

initial motivation to go forward into this direction was to see if LC phased array antennas were possible at even higher frequencies.

To this end, during this thesis, a study was carried out looking at possible applications for LC technology in emerging fields. The relation between device size and switching speed, low losses at higher frequencies, combined with the demand for high data rates on unregulated, potentially mid- to short-ranged data links (high data rate consumer electronics, "bridging the air-gap", data hubs) inspired the idea of a 250 GHz LC phased antenna array.

In a frequency range ten times higher than in the case of LISA_{ES}, the waveguide dimensions are ten times smaller. As switching speed increases roughly proportionally to the electrode distance, this could *centuple* the switching speed, rendering possible steering or beamforming at a speed of e.g. human interaction.

Even with an aperture of several wavelengths the array would not be larger than a common postal stamp or coin. Integrated into the chassis of, for example, a television or computer screen it would establish a connection with, for instance, a mobile phone placed right in front of it.

At 250 GHz the waveguide gauge is WR3.4 with a base width of $a = 864\,\mu\text{m}$ and height $b = a/2 = 432\,\mu\text{m}$. These dimensions are typical for the copper sheets on PCBs. Using the micro-milling capabilities of current PCB prototyping machines, it was demonstrated that such waveguides can be fabricated. Furthermore, 3D printing becomes more and more mature by the day. Devices of these dimensions should therefore pose no obstacle in being cheaply printed, or laminated and structured.

The wavelength in free space at 250 GHz is $\lambda_0 = 1.2\,\text{mm}$. A maximally steerable array is obtained if the elements are spaced at no more than $0.6\lambda_0 = 720\,\mu\text{m}$. While

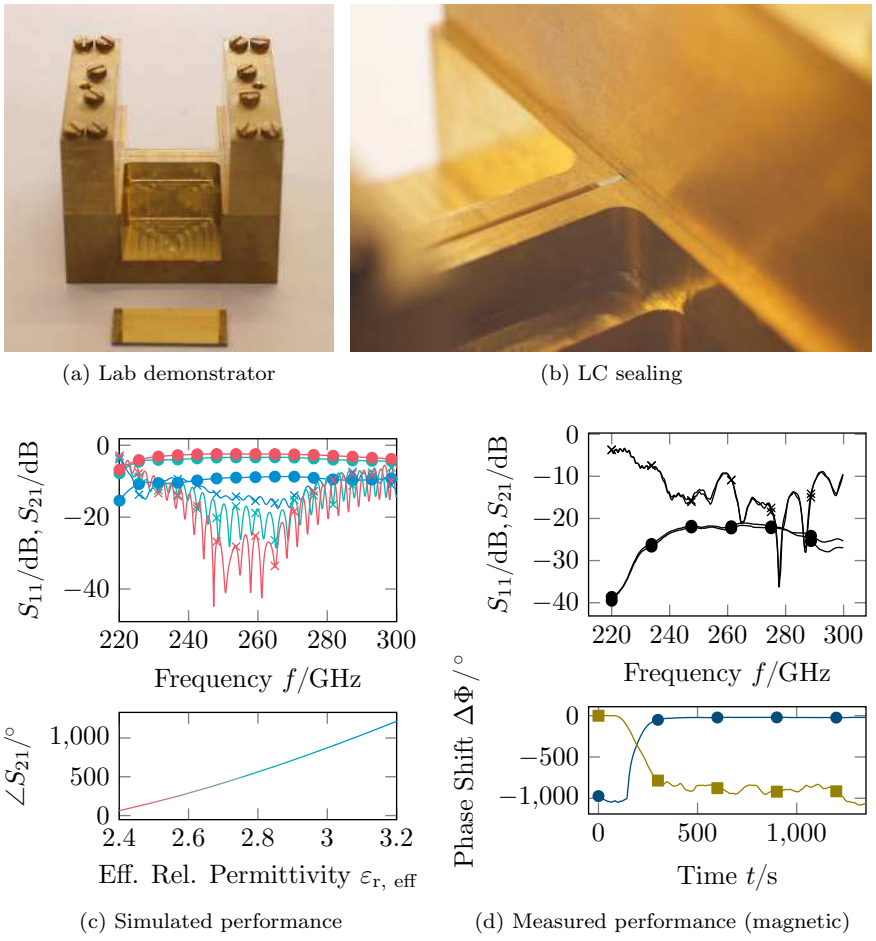

(a) Lab demonstrator

(b) LC sealing

(c) Simulated performance

(d) Measured performance (magnetic)

Figure 5.2.: Components of a waveguide phase shifter demonstrator at 250 GHz: (a) holder for testing lids, e.g. with integrated biasing electrodes, or sealing techniques. (b) Sealing against LC leaking. (c) Performance theoretically possible using LC data at 250 GHz and (d) measured performance with imperfect RF sealing. S_{11}, S_{22} are marked with a cross (—×—), S_{12}, S_{21} are marked with dots (—●—). In (c) the colour of the phase data corresponds to the respective S-parameter colours.

in the vertical direction this would theoretically work as $b < 0.6\lambda_0$, in horizontal direction this is not possible. But for the application brought up above, this is not even necessary.

As shown in Figure 5.1, a simple look at Fresnel's equation for the power transmission through a dielectric interface shows that, at least in theory, a rather large effective

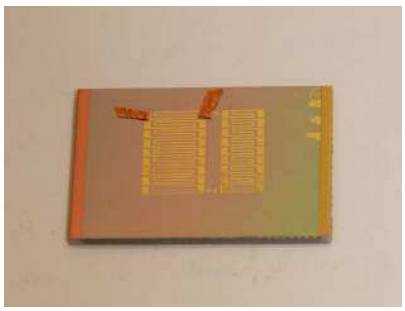

(a) Electrodes on SiO_2/Si_3N_4 on PCB

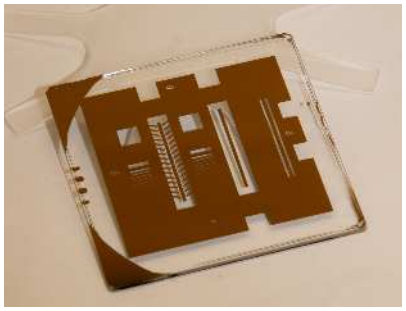

(b) Structuring test for gold nano-wires

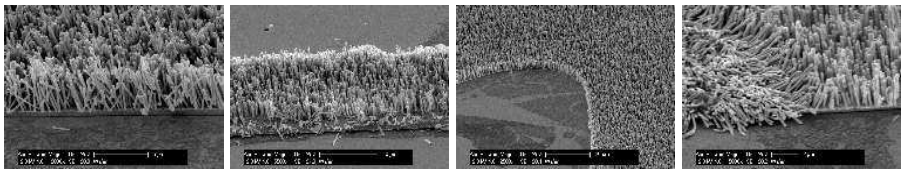

(c) SEM images of structured gold nano-wires

Figure 5.3.: Technology studies for a 250 GHz LC phase shifter: (a) Insulated electrodes realised using a SiO_2/Si_3N_4 on Copper/PCB process, (b) test mask for fine ($\approx$ 50 µm) structuring of gold nano-wires, and (c) scanning electron microscope (SEM) imges of implemented gold nano-wire structures. From left to right: defined border fidelity, fine (sub-50 µm) line fidelity, corner fidelity (radius below 50 µm) and RF-sealing by flattening of the wires

steering range should be covered by only a small actual steering range of the array. This is due to the fact that the array, were it used in a television for instance, would certainly be hidden in the plastic casing. These are usually made of materials like polycabonate (PC), pigmented high-density polyethylene (HDPE) or polystyrene (PS), all of which feature permittivities in the range of 2.4 to 3.0.

In a Master's thesis [Ric15], viable topologies and fabrication processes for a stackable row of 250 GHz LCPS were evaluated. Figures 5.2 and 5.3 show the technologies that were realised and tested in order to evaluate the idea.

A working, magnetically biased LC phase shifter was presented with FoM $\approx 45\,^\circ$/dB. A full-wave simulation in CST showed that around $120\,^\circ$/dB should be possible.

These results are preliminary but show already promising performance, despite problems with the contact resistance of the waveguide lid. This is a typical issue at such high frequencies and can be circumvented using contact areas covered in gold nanotubes fabricated at Institute of Electromechanical Design / Institut für Elektromechanische Konstruktion (EMK). Figure 5.3c shows a set of scanning electron microscope (SEM) images testing the accuracy of the gold nano-wire process for structured de-

position. The overall result was promising and should be pursued further. In a last step [Mar16], the design of electrodes integrated in a waveguide lid was investigated. The study showed that it is compatible with the gold nano-wire process.

Unfortunately, timely constraints would not allow the completion of this preliminary work. The fabrication processes, which included complex lithography and wet-chemical etching, needs to be further explored and tested. However, it is compatible with established processes for planar topologies and should therefore be adaptable.

Overall, the study yielded a number of interesting insights: LC phase shifters also work at significantly higher frequencies, the technological issues are process-related and non-fundamental and the performance, though still far from the projected performance, is better than expected.

The key challenge that could be identified was the intermediate scale, i.e. the fact that the geometrical dimensions often *either* fit microfabrication *or* classical precision fabrication (like CNC milling) but almost never both. Given the emergence of high-precision 3D printing however, the fabrication challenges may well be overcome.

The phase shifters could then be integrated in sheets similar to printed circuit boards, or be stacked and attached using techniques already present e.g. in automotive radar transducers. The resulting package would be a cube of size similar to that of playing dice and, integrated in comsumer electronics or the loading bridge at an airport. Combined with a performant THz transceiver it could transmit a large amount of data in very short time (e.g. download the latest pictures and videos from a handheld device or contact-less updating of the media database of an airplane, flight data, or maps) exploiting the large gain that is possible.

A. Mathematical Appendix

A.1. Derivation of Cavity Eigenvalue Problem for Finite Elements

A.1.1. Classical Resonator Formulation: Complex Resonance Frequency

Maxwell's equations in differential form

$$\operatorname{curl}\vec{E} = -\frac{\partial\mu\vec{H}}{\partial t} \quad \operatorname{curl}\vec{H} = \frac{\partial\varepsilon\vec{E}}{\partial t} + \sigma\vec{E} \quad \operatorname{div}\varepsilon\vec{E} = \rho \quad \operatorname{div}\mu\vec{H} = 0 \tag{A.1}$$

can be simplified for the problem of resonant cavities with dielectric loading, assuming no free charges ($\rho \equiv 0$), non-magnetic materials ($\mu \equiv \mu_0$), and harmonic fields yielding

$$\vec{E},\vec{H}\,(\vec{r},t) = \vec{E},\vec{H}\,(\vec{r})\cdot e^{j\omega t} \quad \longrightarrow \quad \frac{\partial}{\partial t} \to j\omega. \tag{A.2}$$

Taking $\operatorname{curl}\operatorname{curl}\vec{E}$, dividing by μ_0 and inserting $\operatorname{curl}\vec{H}$ yields

$$\frac{1}{\mu_0}\operatorname{curl}\operatorname{curl}\vec{E} = \omega^2\varepsilon\vec{E} - j\omega\sigma\vec{E}. \tag{A.3}$$

The finite element representation of the problem is obtained by taking the inner product on the domain Ω with a test function $\vec{\mathcal{E}}$, thus

$$\frac{1}{\mu_0}\int_\Omega \operatorname{curl}\operatorname{curl}\vec{E}\cdot\vec{\mathcal{E}}\,\mathrm{d}V = \omega^2\int_\Omega \varepsilon\vec{E}\cdot\vec{\mathcal{E}}\,\mathrm{d}V - j\omega\int_\Omega \sigma\vec{E}\cdot\vec{\mathcal{E}}\,\mathrm{d}V. \tag{A.4}$$

The left-hand term is split using the identity $\operatorname{div}\left(\vec{A}\times\vec{B}\right) = \left(\operatorname{curl}\vec{A}\right)\cdot\vec{B} - \left(\operatorname{curl}\vec{B}\right)\cdot\vec{A}$, inserting the curl of the e-field $\operatorname{curl}\vec{E} = \vec{A}$.

$$\operatorname{div}\left(\left(\operatorname{curl}\vec{E}\right)\times\vec{\mathcal{E}}\right) = \left(\operatorname{curl}\left(\operatorname{curl}\vec{E}\right)\right)\cdot\vec{\mathcal{E}} - \left(\operatorname{curl}\vec{E}\right)\cdot\left(\operatorname{curl}\vec{\mathcal{E}}\right) \tag{A.5}$$

The integration of $\left(\operatorname{curl}\left(\operatorname{curl}\vec{E}\right)\right)\cdot\vec{\mathcal{E}}$ on Ω therefore falls into two parts

$$\int_\Omega \left(\operatorname{curl}\operatorname{curl}\vec{E}\right)\cdot\vec{\mathcal{E}}\,\mathrm{d}V = \int_\Omega \left(\operatorname{curl}\vec{E}\right)\cdot\left(\operatorname{curl}\vec{\mathcal{E}}\right)\mathrm{d}V + \int_\Omega \operatorname{div}\left(\operatorname{curl}\vec{E}\times\vec{\mathcal{E}}\right)\mathrm{d}V, \tag{A.6}$$

and furthermore applying Gauß's theorem

$$\int_\Omega \left(\operatorname{curl}\operatorname{curl}\vec{E}\right)\cdot\vec{\mathcal{E}}\,\mathrm{d}V = \int_\Omega \left(\operatorname{curl}\vec{E}\right)\cdot\left(\operatorname{curl}\vec{\mathcal{E}}\right)\mathrm{d}V + \int_{\partial\Omega}\vec{n}_{\partial\Omega}\cdot\left(\operatorname{curl}\vec{E}\times\vec{\mathcal{E}}\right)\mathrm{d}S, \quad \text{(A.7)}$$

where $\vec{n}_{\partial\Omega}$ is the inner normal unit vector on the domain boundary $\partial\Omega$.

The final form therefore reads

$$\frac{1}{\mu_0}\int_\Omega \operatorname{curl}\vec{E}\cdot\operatorname{curl}\vec{\mathcal{E}}\,\mathrm{d}V = \omega^2\int_\Omega \varepsilon\vec{E}\cdot\vec{\mathcal{E}}\,\mathrm{d}V + \frac{1}{\mu_0}\int_{\partial\Omega}\vec{n}_{\partial\Omega}\cdot\left(\operatorname{curl}\vec{E}\times\vec{\mathcal{E}}\right)\mathrm{d}S - j\omega\int_\Omega \sigma\vec{E}\cdot\vec{\mathcal{E}}\,\mathrm{d}V \quad \text{(A.8)}$$

The first r.h.s. term represents the interaction of $\vec{E}$ and ε. The second term contains a Poynting vector alike formulation which vanishes on conductive boundaries and may be used as absorbing boundary condition (ABC) on open domains. It is henceforth neglected as radiation loss is not considered here (the coupling of the resonator to the feed lines is supposed to be less than $-15\,\mathrm{dB}$ at resonance).

The induced current $\vec{J}$ is described by the electric field on a conductive surface and the material conductivity. For typical conductors like Copper, Brass or the likes with electric conductivities in the range of $> 10\times10^6\,\mathrm{S/m}$ the skin effect confines the induced current $\vec{J}$ to a sheet of several tens to hundreds of nm. The induced current can therefore be described by a surface current $\vec{J}_s$ with little error and be tangential to the surface.

The tangential component of $\vec{E}$ on a boundary $\partial\Omega$ with normal component $\vec{n}$ is obtained by

$$\vec{E}_\parallel = -\vec{n}\times\left(\vec{n}\times\vec{E}\right). \quad \text{(A.9)}$$

Given constant conductivity on the boundary, the last term of the r.h.s. can therefore be reformulated as

$$j\omega\int_\Omega \sigma\vec{E}\cdot\vec{\mathcal{E}}\,\mathrm{d}V = -j\omega\sigma\int_{\partial\Omega}\vec{n}\times\left(\vec{n}\times\vec{E}\right)\cdot\vec{\mathcal{E}}\,\mathrm{d}S. \quad \text{(A.10)}$$

The trial field $\vec{\mathcal{E}}$ is by definition zero on the boundary. The boundary integral therefore vanishes for this case.

[Jin10] presents a similar weak form with slightly different boundary conditions.

Electric field and test function, $\vec{E}$ and $\vec{\mathcal{E}}$ are approximated as

$$\vec{E}\approx\sum_{i=1}^{N} e_i\vec{N}_i \quad\text{and}\quad \vec{\mathcal{E}}\approx\sum_{j=1}^{N} e_j\vec{N}_j \quad \text{on}\,\Omega, \quad \text{(A.11)}$$

using curl-conforming (Nédélec function space) basis functions $\vec{N}_{i,j}$ [LMW12].

Following the discretisation method, (A.8) is represented in discrete form such that the left-hand side

$$\frac{1}{\mu_0}\int_\Omega \operatorname{curl}\vec{E}\cdot\operatorname{curl}\vec{\mathcal{E}}\,\mathrm{d}V = \frac{1}{\mu_0}\sum_{i,j}\int_\Omega e_i\operatorname{curl}\vec{N}_i\cdot e_j\operatorname{curl}\vec{N}_j\,\mathrm{d}V = \mathbf{M}_{ij}\cdot\vec{e} \tag{A.12}$$

which is called the mass matrix and is readily assembled by the FEniCS kernel.

Transformed into discrete form, in the same manner, the right-hand side yields

$$\omega^2\int_\Omega \varepsilon\vec{E}\cdot\vec{\mathcal{E}}\,\mathrm{d}V - j\omega\sigma\int_{\partial\Omega}\vec{n}\times\left(\vec{n}\times\vec{E}\right)\vec{\mathcal{E}}\,\mathrm{d}S = \\ = \ldots = \omega^2\sum_{\varepsilon=\varepsilon_\mathrm{I},\varepsilon_\mathrm{II},\ldots}\varepsilon\int_\Omega \mathbf{A}_{ij}\cdot\vec{e} \quad - j\omega\sigma\cdot\mathbf{B}_{ij,\partial\Omega}\cdot\vec{e}. \tag{A.13}$$

$\mathbf{B}_{ij,\partial\Omega}$ is created by multiplying $\mathbf{A}_{ij}$ by a sparsed identity matrix $\mathbf{I}_{\partial\Omega}$ selecting only the boundary elements.

Combining (A.12) and (A.13) forms a generalised eigenvalue problem of the form.

$$\mathbf{M}_{ij}\cdot\vec{e} = \lambda\mathbf{A'}_{ij}\cdot\vec{e}. \tag{A.14}$$

Depending on the posed problem ("find empty resonator's wall conductivity", "find sub-domain's permittivity", ...) the r.h.s. can be reformulated such that λ corresponds to σ, ε, ..., therefore allowing an elegant and usually fast way of determining characteristic properties.

A.1.2. Adaptation to Exploit Cylindrical Symmetry

In order to comply with the need to solve the problem discussed above in real-time (in the sense of the measurement procedure, i. e. faster than seconds) the axial (cylindrical) symmetry of the problem is exploited.

Ciarlet and Labrunie [CL11] present a "method for computing numerically the solution to the time-dependent Maxwell equations in an axisymmetric domain", which is discussed in great detail.

The main aspect, relevant for this application, is the adaption to axisymmetry of the curl operator and the suggestion to decompose the problem into two spaces: a Nédélec space for the curl-containing portion (E_r, E_z) and a Continuous Galerkin (CG) or Lagrange space for the third coordinate (E_φ).

The axisymmetric problem is therefore described by a 2D slice through the resonator and a term $e^{jk\varphi}$ (the authors use θ) which accounts for the mode order k in angular direction. The overall solution is obtained by superimposing individual modes (Fourier analysis), but this is not relevant in the present case, since we are only interested in pure harmonic modes.

In cylindrical coordinates, the curl operator of a vector field $\vec{F} = F_r\vec{e}_r + F_\varphi\vec{e}_\varphi + F_z\vec{e}_z$

for angular (φ) order k becomes

$$\left(\operatorname{curl}_k \vec{F}\right)_r = \frac{jk}{r} F_z - \frac{\partial F_\varphi}{\partial z} \tag{A.15}$$

$$\left(\operatorname{curl}_k \vec{F}\right)_\varphi = \frac{\partial F_r}{\partial z} - \frac{\partial F_z}{\partial r} \tag{A.16}$$

$$\left(\operatorname{curl}_k \vec{F}\right)_z = \frac{1}{r}\left(\frac{\partial \left(r F_\varphi\right)}{\partial r} - jk F_r\right) \tag{A.17}$$

where jk denotes the partial derivative $\partial\varphi$ due to the $e^{jk\varphi}$ symmetry of the problem.

In FEniCS [LMW12], the real-valued approach is implemented by two functions `curl_rz` and `curl_p` as shown in Listing A.1.

```
# Function definitions for the UFL expressions
def curl_rz(w_rz, w_phi, m):
    g_r = m*w_rz[1] - w_phi.dx(1)
    g_z = w_phi.dx(0) - m*w_rz[0]
    return as_vector([g_r, g_z])

def grad_rz(w_rz):
    return w_rz[0].dx(1) - w_rz[1].dx(0)
```

Listing A.1: Shorthand expressions implementing the curl operator and the cross product in an axisymmetric, real-valued problem.

The vector field $\vec{F}_{rz} = F_r\vec{e}_r + F_z\vec{e}_z$ is discretised using Nédélec elements while remaining vector field $\vec{F}_\varphi = F_\varphi\vec{e}_\varphi$ is described solely by it's scalar coefficient F_φ using Lagrange elements.

This is achieved by creating a mixed function space V as shown in Listing A.2.

```
(geo, regions, borders) = convertMesh("resonator-60ghz-gmsh.geo",
↪  dim=2, noConvert=False)

mesh = Mesh(geo)
materials = MeshFunction('size_t', mesh, regions)
conductive = MeshFunction('size_t', mesh, borders)

V  = FunctionSpace(mesh, "N1curl", 1)  # 1st kind, 1st order

N_rz = TestFunction(V)
M_rz = TrialFunction(V)
```

Listing A.2: Creating Function Spaces from 1st or 2nd kind Nédélec (N2curl) and Lagrange (CG, Continuous Galerkin) elements and creation of the test and trial functions

The mass and stiffness matrices are defined via the l.h.s. matrix entries a_{mn}, the r.h.s entries b_{mn} and the conductive boundary entries g_{mn} as given by (A.12) and (A.13), respectively. Using UFL (unified form language) provided by the FEniCS/Dolfin package, this is written in a compact manner as shown in Listing A.3.

```
23 r = Expression('x[0]')
24 dx = Measure("dx")[materials]
25 ds = Measure("ds")[conductive]
26 bc_wall = DirichletBC(V, Constant((0.0, 0.0)), conductive, 1)

27 u_rz = Function(V)

28 eps_r = Eps_R([2.8, 3.75, 1.0, 1.0])

29 mode = ("TE", 1, 1, 2)
30 target_frequency = 30e9

31 k_0_sq = ((2*pi*target_frequency/c0)**2)
32 m = float(mode[1])
33 a_mn = (r * dot( grad_rz(N_rz), grad_rz(M_rz) ) )*dx
34 b_mn = (r * eps_r * dot( N_rz, M_rz ) )*dx
```

Listing A.3: UFL terms defining the l.h.s. and r.h.s of the eigenvalue problem and supplementary instructions

Matrix initialisation, assembly and solution of the eigenvalue problem is shown in Listing A.4.

```
37 a_mn = (r * dot( grad_rz(N_rz), grad_rz(M_rz) ) )*dx
38 b_mn = (r * eps_r * dot( N_rz, M_rz ) )*dx

39 S_te = PETScMatrix()
40 T_te = PETScMatrix()

41 assemble(a_mn, tensor=S_te)
42 assemble(b_mn, tensor=T_te)

43 bc_wall.apply(S_te)
44 bc_wall.apply(T_te)
```

Listing A.4: Setting up matrices for eigenvalue solver

Finally, the Scalable Library for Eigenvalue Problem Computations (SLEPc) eigensolver is prepared and called and provides all converged solutions to the EVP in a handy object shown in Listing A.5.

```
te = SLEPcEigenSolver(S_te,T_te)
te.parameters["tolerance"] = 1e-16
te.parameters["spectral_shift"] = k_0_sq
te.parameters["spectral_transform"] = "shift-and-invert"
te.parameters["spectrum"] = "target real"

te.solve(1)

for i in range(te.get_number_converged()):
  k_r, k_i, ev_r, ev_i = te.get_eigenpair(i)
  f_res = np.sqrt(k_r)*c0/(2*np.pi)
  print("Found f_res = %.5f GHz" % (f_res/1e9))
  u_rz.vector()[:] = ev_r
  plot(u_rz, key="UV", title=("u_rz, f_ana=%f, f_res=%.3f" %
  ↪  (target_frequency/1e9, f_res/1e9)), interactive=False)
  interactive()
```

Listing A.5: Extracting and visualising solutions

The setup of the problem changes slightly once the φ-component of the field is considered, which is the case once TE modes are considered. In this case, an additional boundary condition forces E_φ to be zero along the central axis or otherwise the solution does not obey the symmetry constraints. Listing A.6 shows the extension capable of calculating TE and TM modes.

```
bc_wall = DirichletBC(V, Constant((0.0, 0.0)), conductive, 1)
bc_ctr  = DirichletBC(V.sub(0), Constant(0.0), conductive, 2)
```

```
a_mn =   (1.0/r * dot( curl_rz(N_rz, N_phi, m), curl_rz(M_rz, M_phi,
↪  m) ) )*dx \
       + (    r * dot( grad_rz(N_rz), grad_rz(M_rz) ) )*dx
b_mn =   (    r * eps_r * dot(N_rz, M_rz) )*dx \
       + (1.0/r * eps_r * dot(N_phi, M_phi) )*dx
```

```
bc_wall.apply(S_te)
bc_wall.apply(T_te)
bc_ctr.apply(S_te)
bc_ctr.apply(T_te)
```

Listing A.6: Adapting the code to TE/TM problems

The geometric model is a gmsh `.geo`-file which is automatically meshed and imported. It contains all geometric information as well as material and boundary markers. Materials and boundaries are generically tagged by numbers, which makes the format slightly cryptic but versatile: The metallic boundary will be tagged 1 for example (cf.

Listing A.7), regardless of what conductivity it posesses. This pays off in the final programme, where resonance frequency and quality factor are known from measurement and the objective is to find the conductivity and/or permittivity value of the boundary or a sub-domain as eigenvalues of the eigen-permittivity problem.

In order to account for losses in this approach, both cavity wall losses and dielectric losses can be accounted for by their respective contributions to the loaded quality factor. This is valid, assuming

1. the metallic power loss P_{metal} is low and
2. the dielectric power loss P_{diel} is low.

A.1.3. Adaptation to Exploit Cylindrical Symmetry and Complex Valued Problems

In some cases, in particular when the cavity wall's surface impedance is low, or the material under test either exposes large losses or moderate losses but occupies a large portion of the cavity, the problem cannot be considered purely real valued and the losses cannot be accurately calculated using the power loss method.

Altough this is intrinsically not the case in the method considered here (only valid for high-Q cavities, characterising moderate- to low-loss liquids), there is another aspect that makes considering a complex-valued problem interesting: the determination of all parameters could be unified into one expression.

If the problem is complex valued, the inner product (u, v) is now altered for u and v to be complex-valued functions

$$\langle u, v \rangle = \int_{\Omega} u \cdot v^* \,\mathrm{d}x \tag{A.18}$$

which in turn can be expressed by its real and imaginary parts

$$\langle u_r + j u_i,\ v_r + j v_i \rangle = \int_{\Omega} u_r \cdot v_r \,\mathrm{d}x + \int_{\Omega} u_i \cdot v_i \,\mathrm{d}x + j \int_{\Omega} u_i v_r - u_r v_i \,\mathrm{d}x. \tag{A.19}$$

If the problem converges the last term approaches zero.

The curl-elements can be expressed for a complex vector field $\vec{F} = \vec{F}_{\mathrm{real}} + j\vec{F}_{\mathrm{imag}}$. The φ-part (A.16) does not mix real and imaginary parts. The r- and z-parts however do so (A.15) and (A.17) respectively are reformulated as

$$\Re\left(\operatorname{curl}_k \vec{F}\right)_r = -\frac{k}{r} F_{\mathrm{imag},z} - \frac{\partial F_{\mathrm{real},\varphi}}{\partial z} \tag{A.20}$$

$$\Im\left(\operatorname{curl}_k \vec{F}\right)_r = +\frac{k}{r} F_{\mathrm{real},z} - \frac{\partial F_{\mathrm{imag},\varphi}}{\partial z} \tag{A.21}$$

```
/*  resonator-30ghz.geo: demo geometry file (for gmsh)
 *  Defines cylinder with filling holes and homogeneous air filling.
 *  Defines boundaries and axis of symmetry.
 */

height = 13.86890e-3;
radius = 3.84183e-3;
ext_h  = 2.0e-3;
ext_r  = 0.85e-3/2.0;
fine   = 0.025e-3;
coarse = 0.15e-3;

Point(1) = {0     , height/2+ext_h   , 0, fine};
Point(2) = {ext_r , height/2+ext_h   , 0, fine};
Point(3) = {ext_r , height/2         , 0, fine};
Point(4) = {radius, height/2         , 0, coarse};
Point(5) = {radius, -height/2        , 0, coarse};
Point(6) = {ext_r , -height/2        , 0, fine};
Point(7) = {ext_r , -(height/2+ext_h), 0, fine};
Point(8) = {0     , -(height/2+ext_h), 0, fine};
Point(9) = {0     , 0                , 0, coarse};

Line(1) = {1, 2};
Line(2) = {2, 3};
Line(3) = {3, 4};
Line(4) = {4, 5};
Line(5) = {5, 6};
Line(6) = {6, 7};
Line(7) = {7, 8};
Line(8) = {8, 9};
Line(9) = {9, 1};

Line Loop(10) = {1, 2, 3, 4, 5, 6, 7, 8, 9};
Plane Surface(11) = {10};

// metallic wall - electric boundary
Physical Line(1) = {1, 2, 3, 4, 5, 6, 7};

// central axis - used for symmetry purposes
Physical Line(2) = {8, 9};

// "surface" in rz plane - air filling
Physical Surface(1) = {11};
```

Listing A.7: `gmsh .geo`-file containing the geometry data of the empty 30 GHz resonator

$$\Re\left(\operatorname{curl}{}_k\vec{F}\right)_z = \frac{1}{r}\left(F_{\mathrm{real},\varphi} + r\frac{\partial\left(F_{\mathrm{real},\varphi}\right)}{\partial r} + kF_{\mathrm{imag},r}\right) \tag{A.22}$$

$$\Im\left(\operatorname{curl}{}_k\vec{F}\right)_z = \frac{1}{r}\left(F_{\mathrm{imag},\varphi} + r\frac{\partial\left(F_{\mathrm{imag},\varphi}\right)}{\partial r} - kF_{\mathrm{real},r}\right) \tag{A.23}$$

So, the main work has to be done on the l.h.s. of (A.8).

A.2. Finite Element Calculation of Waveguide Modes in Inhomogeneous, Anisotropic Media

The reference frame is cartesian, which makes the formulation a lot more straightforward. A mathematically comprehensive derivation can be found in [Ott+12] and [LMW12, Ch. 34]. This section mainly focusses on applying the anisotropy in the equations and presents a slightly updated software implementation with respect to the aforementioned references.

A.2.1. Helmholtz Equation in Anisotropic Media

The Helmholtz equation is adapted for calculation on a waveguide cross-section, in the xy-plane and assuming sufficently long elongation along the z-direction such that a harmonic dependency of $e^{\gamma z}$ is justified. The $\varepsilon\ \varepsilon_r$ is treated as a tensor of the form

$$\varepsilon_r = \begin{pmatrix} \varepsilon_{r,xx} & \varepsilon_{r,xy} & 0 \\ \varepsilon_{r,yx} & \varepsilon_{r,yy} & 0 \\ 0 & 0 & \varepsilon_{r,zz} \end{pmatrix}, \quad \text{with } \varepsilon_{r,zz} = \varepsilon_\perp, \tag{A.24}$$

which models the in general assuming the director field is entirely transversal (i. e. the z-component of $\vec{n}$ is zero everywhere). Then, the upper-left 2×2 subtensor is defined by

$$\tilde{\varepsilon}_{r,2\times 2} = \begin{pmatrix} \varepsilon_{r,xx} & \varepsilon_{r,xy} \\ \varepsilon_{r,yx} & \varepsilon_{r,yy} \end{pmatrix} = \varepsilon_\perp \cdot \mathbf{I} + \left(\varepsilon_\parallel - \varepsilon_\perp\right) \cdot \left(\vec{n} \otimes \vec{n}\right). \tag{A.25}$$

Using these assumptions, the problem can be treated much like in [LMW12, Ch. 34].

The weak form

$$\int_\Omega \left(\operatorname{curl}\vec{E}\right)\left(\operatorname{curl}\vec{\mathcal{E}}\right)\mathrm{d}x - k_0^2 \int_\Omega \varepsilon_r(x)\vec{E}\vec{\mathcal{E}}\,\mathrm{d}x = 0 \tag{A.26}$$

is reformulated. The curl operator is treated as the sub of a transversal (xy) and a longitudinal (z) operator such that

$$\nabla = \nabla_{xy} + \nabla_z = \begin{pmatrix} \partial_x \\ \partial_y \\ 0 \end{pmatrix} + \begin{pmatrix} 0 \\ 0 \\ \partial_z \end{pmatrix}. \tag{A.27}$$

Similar to the cylinder, the electric field is partitioned in a transversal (xy) and a longitudinal (z) part as well, with an assumed harmonic space dependency in z, such that

$$\vec{E}(x,y)\cdot e^{-\gamma z} = \left(\vec{E}_{xy}(x,y) + \vec{e}_z E_z(x,y)\right) e^{-\gamma z}. \tag{A.28}$$

The curl $\vec{E}$, removing the $e^{-\gamma z}$ term, therefore decomposes into

$$\operatorname{curl}\vec{E} = \nabla_{xy}\times\vec{E}_{xy} + \nabla_{xy}\times\vec{E}_z + \gamma\mathbf{i}\vec{E}_{xy}, \quad \text{with } \mathbf{i} = \operatorname{diag}(1,-1,0), \tag{A.29}$$

where it should be noted that $\mathbf{i}\vec{F}\cdot\mathbf{i}\vec{G} = \vec{F}\cdot\vec{G}$, a notation that is used in a similar fashion in [Sch03].

This is important for the final form of the weak form, which reads

$$\begin{aligned}\int_\Omega \left(\nabla_{xy}\times\vec{E}_{xy}\right)\cdot\left(\nabla_{xy}\times\vec{\mathcal{E}}_{xy}\right)\mathrm{d}x \\ + \int_\Omega \left(\nabla_{xy}\times\vec{E}_z + \gamma\vec{E}_{xy}\right)\cdot\left(\nabla_{xy}\times\vec{\mathcal{E}}_z + \gamma\vec{\mathcal{E}}_{xy}\right)\mathrm{d}x \\ - k_0^2\left(\int_\Omega \varepsilon_{r,zz}(x)\vec{E}_z\vec{\mathcal{E}}_z\,\mathrm{d}x + \int_\Omega \tilde{\varepsilon}_{r,2\times2}(x)\vec{E}_{xy}\vec{\mathcal{E}}_{xy}\,\mathrm{d}x\right) = 0.\end{aligned} \tag{A.30}$$

A.2.2. Determining the Cut-Off Frequency

At cut-off, $\gamma \equiv 0$ and therefore $k_0 = k_{co}$, and $E_z = 0$ such that (A.30) simplifies to

$$\int_\Omega \left(\nabla_{xy}\times\vec{E}_{xy}\right)\cdot\left(\nabla_{xy}\times\vec{\mathcal{E}}_{xy}\right)\mathrm{d}x - k_{co}^2\int_\Omega \tilde{\varepsilon}_{r,2\times2}(x)\vec{E}_{xy}\vec{\mathcal{E}}_{xy}\,\mathrm{d}x = 0, \tag{A.31}$$

which can be solved as a general EVP with $\lambda = k_{co}^2$.

A.2.3. Determining the Propagation Constant

At any other given wavenumber k_0, using the substitution $\gamma\vec{E}_{xy} = \vec{E}_{xy,\gamma}$, the EVP is solved with $\lambda = -\gamma^2$ from the system

$$\int_\Omega \left(\nabla_{xy} \times \vec{E}_{xy,\gamma}\right) \cdot \left(\nabla_{xy} \times \vec{\mathcal{E}}_{xy,\gamma}\right) \mathrm{d}x - k_0^2 \int_\Omega \tilde{\varepsilon}_{r,2\times2}(x)\vec{E}_{xy,\gamma}\vec{\mathcal{E}}_{xy,\gamma}\,\mathrm{d}x + \gamma^2 \left(\int_\Omega \left(\nabla_{xy} \times \vec{E}_z + \vec{E}_{xy,\gamma}\right) \cdot \left(\nabla_{xy} \times \vec{\mathcal{E}}_z + \vec{\mathcal{E}}_{xy,\gamma}\right) \mathrm{d}x - k_0^2 \int_\Omega \varepsilon_{r,zz}(x)\vec{E}_z\vec{\mathcal{E}}_z\,\mathrm{d}x \right) = 0. \quad \text{(A.32)}$$

A.3. Useful Equations and Relations

Energy Stored in Electromagnetic Field

$$W_{\mathrm{el}} = \frac{\varepsilon_0}{4} \int_\Omega \varepsilon_r'(x) \left|\vec{E}\right|^2 \mathrm{d}V \quad \text{(A.33)}$$

$$W_{\mathrm{mag}} = \frac{\mu_0}{4} \int_\Omega \mu_r'(x) \left|\vec{H}\right|^2 \mathrm{d}V \quad \text{(A.34)}$$

At resonance: $W_{\mathrm{el}} = W_{\mathrm{mag}}$.

Power dissipated in Dielectric

$$P_{\mathrm{el}} = \frac{\omega}{2} \int_\Omega \varepsilon_r''(x) \left|\vec{E}\right|^2 \mathrm{d}V \quad \text{(A.35)}$$

Power dissipated on Metal Wall

$$P_{\mathrm{wall}} = \frac{R_s}{2} \int_{\partial\Omega} \left|\vec{H}_t\right|^2 \mathrm{d}S \quad \text{(A.36)}$$

where

$$R_s = \sqrt{\frac{\omega\mu}{2\sigma}} \qquad \text{and} \qquad \vec{H}_t = \vec{n} \times \vec{n} \times \vec{H} \text{ on } \partial\Omega$$

Resonator Quality Factor at Resonance

$$Q = \omega \frac{W_{\mathrm{mag}} + W_{\mathrm{el}}}{P_{\mathrm{loss}}} = 2\omega_0 \frac{W_{\mathrm{el}}}{P_{\mathrm{loss}}} \quad \text{(A.37)}$$

where P_{loss} is the sum of all dissipated power.

A.4. Derived Expressions for Characterisation

Empty Resonator Only loss mechanism is ohmic loss in wall:

$$W_{\mathrm{el}} = \frac{\varepsilon_0}{4} \iiint_{\Omega} |E|^2 \,\mathrm{d}V \tag{A.38}$$

$$P_{\mathrm{loss}} = P_{\mathrm{metal}} = 2\omega_{\mathrm{empty}} \frac{W_{\mathrm{el}}}{Q_{\mathrm{empty}}} \tag{A.39}$$

$$\sqrt{\sigma^{(e)}} = \frac{1}{P_{\mathrm{metal}}} \sqrt{\frac{\omega_0 \mu}{8}} \oiint_{\partial\Omega} |H_t|^2 \,\mathrm{d}S \tag{A.40}$$

Quartz Loaded Resonator Obtained from measurement: ω, Q. Obtained by parameter extraction: $\varepsilon'_{r,\mathrm{quartz}}$. Obtained from earlier step: $\sqrt{\sigma^{(e)}}, P_{\mathrm{metal}}$ If field perturbation is small, $P'_{\mathrm{metal}} = P_{\mathrm{metal}}$ from empty resonator. Otherwise $\sqrt{\sigma^{(e)}}$ must be used.

$$W_{\mathrm{el}} = \frac{\varepsilon_0}{4} \iiint_{\Omega_{\mathrm{air,\ diel}}} |E|^2 \,\mathrm{d}V + \frac{\varepsilon_0}{4} \varepsilon'_{r,\mathrm{quartz}} \iiint_{\Omega_{\mathrm{quartz}}} |E|^2 \,\mathrm{d}V \tag{A.41}$$

$$P_{\mathrm{loss}} = 2\omega W_{\mathrm{el}} / Q \tag{A.42}$$

$$P'_{\mathrm{metal}} = \sqrt{\frac{\omega_0 \mu}{8\sigma^{(e)}}} \oiint_{\partial\Omega} |H_t|^2 \,\mathrm{d}S \tag{A.43}$$

$$P_{\mathrm{loss}} = P'_{\mathrm{metal}} + \frac{\omega \varepsilon_0}{2} \varepsilon''_{r,\mathrm{quartz}} \iiint_{\Omega_{\mathrm{quartz}}} |E|^2 \,\mathrm{d}V \tag{A.44}$$

$$\varepsilon''_{r,\mathrm{quartz}} = \frac{P_{\mathrm{loss}} - P'_{\mathrm{metal}}}{\frac{\omega\varepsilon_0}{2} \iiint_{\Omega_{\mathrm{quartz}}} |E|^2 \,\mathrm{d}V} \tag{A.45}$$

$$\tan\delta_{\mathrm{quartz}} = \frac{\varepsilon''_{r,\mathrm{quartz}}}{\varepsilon'_{r,\mathrm{quartz}}} \tag{A.46}$$

Dielectric Loaded Resonator with Quartz Obtained from measurement: ω, Q. Obtained by parameter extraction: $\varepsilon'_{r,\mathrm{diel}}$. Obtained from earlier steps: $\sqrt{\sigma^{(e)}}, \varepsilon'_{r,\mathrm{quartz}}, \varepsilon''_{r,\mathrm{quartz}}$

$$W_{\mathrm{quartz}} = \frac{\varepsilon_0}{4}\varepsilon'_{r,\mathrm{quartz}} \iiint\limits_{\Omega_{\mathrm{quartz}}} |E|^2 \,\mathrm{d}V \tag{A.47}$$

$$W_{\mathrm{diel}} = \frac{\varepsilon_0}{4}\varepsilon'_{r,\mathrm{diel}} \iiint\limits_{\Omega_{\mathrm{diel}}} |E|^2 \,\mathrm{d}V \tag{A.48}$$

$$W_{\mathrm{el}} = \frac{\varepsilon_0}{4} \iiint\limits_{\Omega_{\mathrm{air}}} |E|^2 \,\mathrm{d}V + W_{\mathrm{quartz}} + W_{\mathrm{diel}} \tag{A.49}$$

$$P'_{\mathrm{metal}} = \sqrt{\frac{\omega_0 \mu}{8\sigma^{(e)}}} \oiint\limits_{\partial\Omega} |H_t|^2 \,\mathrm{d}S \tag{A.50}$$

$$P_{\mathrm{quartz}} = \frac{\omega\varepsilon_0}{2}\varepsilon''_{r,\mathrm{quartz}} \iiint\limits_{\Omega_{\mathrm{quartz}}} |E|^2 \,\mathrm{d}V \tag{A.51}$$

$$P_{\mathrm{loss}} = 2\omega W_{\mathrm{el}}/Q = P_{\mathrm{wall}} + P_{\mathrm{quartz}} + P_{\mathrm{diel}} \tag{A.52}$$

$$\varepsilon''_{r,\mathrm{diel}} = \frac{P_{\mathrm{loss}} - P'_{\mathrm{metal}} - P_{\mathrm{quartz}}}{\frac{\omega\varepsilon_0}{2} \iiint_{\Omega_{\mathrm{diel}}} |E|^2 \,\mathrm{d}V} \tag{A.53}$$

$$\tan\delta_{\mathrm{diel}} = \frac{\varepsilon''_{r,\mathrm{diel}}}{\varepsilon'_{r,\mathrm{diel}}} \tag{A.54}$$

Analytic fields in cylindrical cavities The **TE** modes are described by (derived from [Poz11, Table 3.5, p. 128]):

$$E_r = -jH_0 \frac{\omega\mu n}{k_c^2 r} \left(A\cos n\varphi - B\sin n\varphi\right) J_n\left(k_c r\right) \sin\frac{l\pi z}{H}, \tag{A.55a}$$

$$E_\varphi = jH_0 \frac{\omega\mu}{k_c} \left(A\sin n\varphi + B\cos n\varphi\right) J'_n\left(k_c r\right) \sin\frac{l\pi z}{H}, \tag{A.55b}$$

$$E_z = 0, \tag{A.55c}$$

$$H_r = H_0 \frac{\beta}{k_c} \left(A\sin n\varphi + B\cos n\varphi\right) J'_n\left(k_c r\right) \cos\frac{l\pi z}{H}, \tag{A.55d}$$

$$H_\varphi = -H_0 \frac{\beta n}{k_c^2 r} \left(A\cos n\varphi - B\sin n\varphi\right) J_n\left(k_c r\right) \cos\frac{l\pi z}{H}, \tag{A.55e}$$

$$H_z = H_0 \left(A\sin n\varphi + B\cos n\varphi\right) J_n\left(k_c r\right) \sin\frac{l\pi z}{H}, \tag{A.55f}$$

where $k_c = p'_{nm}/R$, with p'_{nm} the m^{th} zero of the first derivative of Bessel function of first kind and n^{th} order. H_0 is the H-field amplitude of unit $\mathrm{A\,m^{-1}}$.

The **TM** modes are described by (ibidem):

$$E_r = -jE_0 \frac{\beta}{k_c} \left(A \sin n\varphi + B \cos n\varphi\right) J_n'\left(k_c r\right) \sin \frac{l\pi z}{H}, \tag{A.56a}$$

$$E_\varphi = -jE_0 \frac{\beta n}{k_c^2 r} \left(A \cos n\varphi - B \sin n\varphi\right) J_n\left(k_c r\right) \sin \frac{l\pi z}{H}, \tag{A.56b}$$

$$E_z = E_0 \left(A \sin n\varphi + B \cos n\varphi\right) J_n\left(k_c r\right) \cos \frac{l\pi z}{H}, \tag{A.56c}$$

$$H_r = E_0 \frac{\omega\varepsilon n}{k_c^2 r} \left(A \cos n\varphi - B \sin n\varphi\right) J_n\left(k_c r\right) \cos \frac{l\pi z}{H}, \tag{A.56d}$$

$$H_\varphi = -E_0 \frac{\omega\varepsilon}{k_c} \left(A \sin n\varphi + B \cos n\varphi\right) J_n'\left(k_c r\right) \cos \frac{l\pi z}{H}, \tag{A.56e}$$

$$H_z = 0, \tag{A.56f}$$

where $k_c = p_{nm}/R$, with p_{nm} the m^{th} zero of the Bessel function of first kind and n^{th} order. A and B are of unit 1. For the energy terms, it is advantageous to choose $A = 0$ and $B = 1$. E_0 is the E-field amplitude of unit $\mathrm{V\,m^{-1}}$.

For both cases we have: $\beta = \omega/c_0$, $J_n(x)$ the Bessel functions of first kind and n^{th} order, $J_n'(x) = \frac{d}{dx} J_n(x)$ the first derivative of the Bessel function of first kind and n^{th} order, R and H the cylinder radius and height respectively, and (n, m, l) the mode orders.

Curl of $\vec{E}$ in rz-φ notation The curl can be elegantly decomposed compatible with the notation used in Chapter 3 with $\tilde{E}_\varphi = rE_\varphi$:

$$\begin{aligned} \operatorname{curl} \vec{E} = \quad & \vec{e}_r \cdot \frac{1}{r} \left(\partial_\varphi E_z - \partial_z \tilde{E}_\varphi\right) \\ & + \vec{e}_\varphi \cdot \left(\partial_z E_r - \partial_r E_z\right) \\ & + \vec{e}_z \cdot \frac{1}{r} \left(\partial_r \tilde{E}_\varphi - \partial_\varphi E_r\right). \end{aligned}$$

φ-periodicity dictates that all fields $\propto e^{jm\varphi}$, i.e. $\partial_\varphi \to jm$, that is

$$\begin{aligned} \operatorname{curl} \vec{E} = \quad & \vec{e}_r \cdot \frac{1}{r} \left(jmE_z - \partial_z \tilde{E}_\varphi\right) \\ & + \vec{e}_\varphi \cdot \left(\partial_z E_r - \partial_r E_z\right) \\ & + \vec{e}_z \cdot \frac{1}{r} \left(\partial_r \tilde{E}_\varphi - jmE_r\right). \end{aligned}$$

H_{rz} and H_φ from $\vec{E}$ From Maxwell's equations

$$\vec{H} = \frac{j}{\mu_0 \omega} \operatorname{curl} \vec{E}, \tag{A.57}$$

such that

$$\vec{H}_{rz} = \frac{j}{\mu_0 \omega} \frac{1}{r} \left\{ \vec{e}_r \left(jmE_z - \partial_z \tilde{E}_\varphi \right) + \vec{e}_z \left(\partial_r \tilde{E}_\varphi - jmE_r \right) \right\} \tag{A.58}$$

$$H_\varphi = \partial_z E_r - \partial_r E_z \tag{A.59}$$

Analytic field energies in cylindrical cavities The total energy in a **TE** mode is given by

$$W_{\mathrm{el}} = \frac{\varepsilon_0 \pi H}{16} \left(H_0 \frac{\omega \mu p'_{nm}}{k_c^2} \right)^2 \left(1 - \frac{n^2}{{p'_{nm}}^2} \right) J_n^2 \left(p'_{nm} \right) \tag{A.60a}$$

$$W_{\mathrm{mag}} = \frac{\mu_0 \pi H}{16} \left(H_0 \frac{p'_{nm}}{k_c} \right)^2 \left(1 + \left(\frac{\beta}{k_c} \right)^2 \right) \left(1 - \frac{n^2}{{p'_{nm}}^2} \right) J_n^2 \left(p'_{nm} \right) \tag{A.60b}$$

and for **TM** modes by

$$W_{\mathrm{el}} = \frac{\varepsilon_0 \pi H}{16} \left(E_0 \frac{p_{nm}}{k_c} \right)^2 \left(1 + \left(\frac{\beta}{k_c} \right)^2 \right)^2 {J'_n}^2 \left(p_{nm} \right) \tag{A.61a}$$

$$W_{\mathrm{mag}} = \frac{\mu_0 \pi H}{16} \left(E_0 \frac{\omega \varepsilon p_{nm}}{k_c^2} \right)^2 {J'_n}^2 \left(p_{nm} \right) \tag{A.61b}$$

using (A.33) and (A.34), $W_{\mathrm{total}} = W_{\mathrm{el}} + W_{\mathrm{mag}}$, $k_c = p'_{nm}/R$ (TE) and $k_c = p_{nm}/R$ (TM) respectively and $\beta = \sqrt{(\omega/c_0)^2 - k_c^2}$.

Influence of small wall perturbations on resonance frequencies Based on Slate's perturbation theory, Gao [Gao92] determines the detuning of a cavity due to a perturbation by a small circular iris in the wall using

$$\omega^2 = \omega_0^2 \left(1 + \frac{2 \left(\Delta W_{\mathrm{mag}} - \Delta W_{\mathrm{el}} \right)}{W_{\mathrm{total}}} \right), \tag{A.62}$$

where ω_0 is the resonance frequency without the perturbation, W_{total} the total stored field energy and $\Delta W_{\mathrm{mag,el}}$ are the energies of the perturbing effective dipole given by

$$\Delta W_{\mathrm{el}} = -\frac{\varepsilon_0}{12} r_{\mathrm{iris}}^3 \left(\frac{|E_0|}{2} \right)^2 \tag{A.63}$$

$$\Delta W_{\mathrm{mag}} = -\frac{\mu_0}{6} r_{\mathrm{iris}}^3 \left(\left(\frac{|H_1|}{2} \right)^2 + \left(\frac{|H_2|}{2} \right)^2 \right), \tag{A.64}$$

where E_0 is the unperturbed e-field component normal and $H_{1,2}$ are the unperturbed h-field components tangential to the wall at the position of the iris (without the iris perturbation) and r_{iris} is the iris radius.

Thus if the perturbed frequency ω corresponds to the measured frequency ω_{meas}, the effect is compensated for by

$$\omega_0 = \frac{\omega_{\text{meas}}}{\sqrt{1 + \frac{2(\Delta W_{\text{mag}} - \Delta W_{\text{el}})}{W_{\text{total}}}}} \tag{A.65}$$

For example the TE_{112} shows that this method only validly models the perturbation when the field is constant over the iris. It should, however, rather be approximated by a second order polynomial that accounts for asymmetries which can occur for instance at the field node/null of TE_{112}.

Remark on sensitivity of Q factor estimation Assume, the unknown Q b is to be determined based on a known, unloaded Q a and a loaded Q c which is the result of a measurement. The figures are related by

$$\frac{1}{c} = \frac{1}{a} + \frac{1}{b} \quad \Leftrightarrow \quad c = \frac{ab}{a+b} \tag{A.66}$$

The sensitivity of the second measurement, i. e. the change of c with respect to a change in the determinant b, is given by

$$\frac{\partial c}{\partial b} = \frac{a^2}{(a+b)^2}.$$

Hence, generally the sensitivity is the higher, the larger the unloaded Q a. If b is small, this dependency is negligible and $\frac{\partial c}{\partial b} \to 1$. This corresponds to lossy (low Q). If b is large (low-loss), a must be all the higher in order to come close to the upper limit of the function. Otherwise the sensitivity strives towards 0 at a rate of 2 decades per decade in a/b.

A.5. Derived Expressions for Fourier-Transform Interferometry

Derivation for (3.23): Let the electric field spectrum of the source $E(\omega)$ be split in half, one arm delated by an offset d and finally both arms superimposed. The resulting beam's intensity be measured as a function of the offset d, such that

$$\begin{aligned} I(d) &= \int_0^\infty \left| \frac{1}{2} E(\omega) \cdot \left(1 + e^{j\frac{\omega}{c_0}d}\right) \right|^2 \mathrm{d}\omega \\ &= \int_0^\infty \frac{1}{4} \left|E(\omega)\right|^2 \cdot \left|1 + e^{j\frac{\omega}{c_0}d}\right|^2 \mathrm{d}\omega \end{aligned}$$

$$
\begin{aligned}
&= \int_0^\infty \frac{1}{4} \left|E(\omega)\right|^2 \cdot \left(1 + e^{j\frac{\omega}{c_0}d}\right) \cdot \left(1 + e^{-j\frac{\omega}{c_0}d}\right) \mathrm{d}\omega \\
&= \int_0^\infty \frac{1}{4} \left|E(\omega)\right|^2 \cdot \left(1 + e^{j\frac{\omega}{c_0}d} e^{-j\frac{\omega}{c_0}d} + e^{j\frac{\omega}{c_0}d} + e^{-j\frac{\omega}{c_0}d}\right) \mathrm{d}\omega \\
&= \int_0^\infty \frac{1}{4} \left|E(\omega)\right|^2 \cdot \left(2 + 2\cos\frac{\omega}{c_0}d\right) \mathrm{d}\omega \\
&= \frac{1}{2} \int_0^\infty \left|E(\omega)\right|^2 \cdot \left(1 + \cos\frac{\omega}{c_0}d\right) \mathrm{d}\omega
\end{aligned}
$$

Acknowledgements

A lot of people were directly or indirectly involved in making this thesis work.

I would like to thank Prof. Rolf Jakoby for providing the environment for this work. Furthermore, my thanks go to Prof. Arne Jacob and Prof. Harald Klingbeil for giving very accurate feedback and corrections.

Now to the people who did the actual work: The $\mathrm{LISA}_{\mathrm{ES}}$ project team, in particular Alex Höhn, Norbert Nathrat, Matthias Tebbe and Stephan Endler. I learned a lot during those five years. My colleagues, of whom should be named at least: Alex Gäbler, Matthias Maasch, Matthias Jost, Matthias Nickel, Erick González Rodríguez and David Lämmle. They provided a lot of input, feedback and/or consolation.

Furthermore, I thank the colleagues at Merck, in particular Carsten Fritzsch and Michael Wittek.

I owe greatly to Roger A. Lewis, Evan Constable, Andrew Squires, Jarrod Colla and Julian Steele for two great trips to Australia (yup, went there, now get over it!) and *heaps o' stuff*[1] I learned there. Also, Kangaroos.

I enjoyed the interaction with my students, who worked tirelessly on projects even I was not sure would work — and of which some did not work. In particular I would like to thank Martin Rickes, Sönke Schmidt, Muhammad Ali Khalid and Mathias Marscholl.

At last, there is a group of people who let the devices treated in this work be made of more than tank tape, rubble and some old cables: Peter Kießlich, Andreas Semrad, Silke Schober, and Karin Boye at IMP, Walter Albrecht, Corinna Harsche, Viktor Fröse, and Tom Schildknecht at EMK and none the least Martin Morillas at University of Wollongong.

This work was funded by Deutsches Zentrum für Luft- und Raumfahrt (BMWi/DLR) grant 50YB1113, Deutsche Forschungsgemeinschaft (DFG) grants JA 921/29-1 and -2 and State of Hesse LOEWE Sensors Towards Terahertz.

And then there are those who keep *you* going: Viola, my family and my friends.

[1] This, I assume, is Australian.

Glossary

7.30 × 3.35 mm² Custom waveguide cross-section between WR28 and WR34 developed for $\mathrm{LISA_{ES}}$. 60, 68–70

DC Direct current, technically a frequency of 0 Hz. In this work, low frequency current or voltages (up to some kHz) are laxly considered "DC". 11

eigendecomposition Factorisation of a matrix or tensor whereby the matrix is represented by its eigenvalues and eigenvectors. 6

Fresnel ellipsoid Ellipsoid that relates eigenpermittivities with its radii to visualise anisotropic material. 6, 8

FTIR Initially "Fourier Transform Infrared Spectroscopy" (hence -IR) due to its origin in the optical range. The principle is nowadays applied in a wide range of frequencies, hence the term "interferometry" is chosen in this work. i, 21, 41–47, 49, 50

GEO Geostationary orbit (also: geosynchronos equatorial orbit). Orbit radius such that its period is one day precisely, $r = 42\,241\,\mathrm{km}$, i. e. average altitude of 35 870 km above sea level. 2, 57–59

GT3-23001 High tunability, low loss Merck Liquid Crystal blend. 64, 67

GT5-26001 High tunability, low loss Merck Liquid Crystal blend. 64, 66, 67, 83, 92

GT5-28004 Merck Liquid Crystal blend optimised for extremely low loss and high anisotropy, introducing high viscosity. 67

K15 Trade name of 5CB. 40

LCPS Liquid Crystal Phase Shifter. 61, 63, 64, 66, 76, 78, 95, 99

LEO Low orbits for satellites, orbit radii typically in the range of $r = 6600\,\mathrm{km} to 8400\,\mathrm{km}$, i. e. average altitudes of $230\,\mathrm{km} to 2030\,\mathrm{km}$ above sea level. 1, 2, 57–59, 97

Mylar Polyester film produced by DuPont. 63

Polymer Resistor RS 12116 Resistive Paste for screen printing and low temperature ($< 200\,^\circ\mathrm{C}$) curing. 72

Pyralux AP Polyimide sheets of various thickness, usually provided with copper cladding. Types used in this work: Pyralux AP 7164 and AP 7125 [DuP09]. 66, 69, 71, 82

Rexolite Cross-linked polystyrene produced by C-Lec Plastics Inc. In this work the grade Rexolite-1422 is used. 38, 63, 65, 66, 76, 81, 82, 85

RF device Sub-summation of devices for the microwave, millimetre-wave and terahertz range, defined for this work to stretch from 10 GHz to 10 THz. 5, 16

SimLCwg Simulation package for 2D RF simulation involving LC director dynamics developed by A. Gäbler [Gäb+08b]. 68

SPICE Versatile circuit simulator. The Gnu Circuit Analysis Package (Gnucap) Version 2009.12.07 RCS 26.136. 72

Zeiss Glue 56 Two component Epoxy Glue 56, Carl Zeiss Jena GmbH. 30, 32, 66, 76, 85

Acronyms

5G 5^{th} generation mobile networks. 2

6CB 4-Cyano-4'-pentylbiphenyl. 40

Airbus DS Airbus Defence and Space. 92

Artemis Advanced Data Relay and Technology Mission. 57, 58

boPET biaxially-oriented polyethylene terephthalate. 69

Cicor Cicor Reinhardt Microtech GmbH, Ulm, Germany. 71

CPM cavity perturbation method. 19, 67

CST CST Studio Suite. 24, 25, 27, 28, 35, 61, 65, 68, 99

CW continuous-wave. 89, 90, 95

DEOS "Deutsche Orbitale Servicing Mission". 57, 58, 61

DFB distributed feedback. 20

DI de-ionised. 78

DLR Deutsches Zentrum für Luft- und Raumfahrt, German Aerospace Center. 1

EMK Institute of Electromechanical Design / Institut für Elektromechanische Konstruktion. 99

EO Earth-observation. 57

ERS European Remote Sensing Satellite. 57

ESA European Space Agency. 57

EVP eigenvalue problem. 21, 23, 24, 29, 33, 106, 111, 112

FEM Finite Element Method. i, 20, 22, 23, 25, 34, 38, 39, 49, 97

FEniCS the FEniCS Project. i, iii, 20, 22–29, 33, 38, 39, 67, 74

FFT Fast Fourier-Transform. 45

FIR far infrared. 40, 97

Galvano-T Galvano-T GmbH, Windeck/Rosbach, Germany. 77, 78

GEWO GEWO Feinmechanik GmbH, Wörth/Hörlkofen, Germany. 76

HDPE high-density polyethylene. 99

Heinrich-Hertz Heinrich Hertz mission. 58

IMST GmbH IMST GmbH, Kamp-Lintfort, Germany. 69, 71, 83, 87

IR infrared. 40, 42, 43

Klobe Otto Klobe & Sohn GmbH, Kaufbeuren, Germany. 76, 77

LC Liquid Crystal. i, 2, 3, 5–8, 11, 13–17, 19, 21, 22, 24, 29, 32, 33, 39–42, 44, 45, 47–49, 58, 61–66, 68, 72, 74, 76, 78, 81–83, 85, 89, 92, 94, 96–101, 110

l.h.s. left-hand side. 24

LISA Light-weight Intersatellite Antenna. 63, 69, 70

LISA$_{ES}$ Light-weight Intersatellite Antenna – Electronical Steering. i, iii, 2, 3, 24, 29, 30, 57, 58, 60, 61, 63, 66, 67, 69, 71, 79, 87, 96–98, 121

LISA$_{MS}$ Light-weight Intersatellite Antenna – Mechanical Steering. 60

LNA Low-Noise Amplifier. 98

LRT Chair of Astronautics (Lehrstuhl für Raumfahrttechnik, LRT). 76, 77

MBBA N-(4-Methoxybenzylidene)-4-butylaniline. 8

Merck Merck KGaA, Darmstadt. i, 16, 17, 32, 41, 67

MIMO multiple in multiple out. 2

MUT material under test. 19, 24–27, 34, 36, 39, 44, 45, 47, 117

NASA National Aeronautics and Space Administration. 57

NTP NTP-Ingenieure GmbH & Co. KG, Neubiberg, Germany. 61, 69

OOS on-orbit servicing. 57

PC polycabonate. 99

PCB printed circuit board. 82, 98, 101

PNA-X Keysight PNA-X N5247A. 83, 86

PP polypropylene. 44, 45, 47, 48

PS polystyrene. 99

PTFE Polytetrafluoroethylene. 64, 65

RF Radio Frequency. 21, 63, 78, 80, 92, 97, 100, 101

r.h.s. right-hand side. 23, 24

SLEPc Scalable Library for Eigenvalue Problem Computations. 106

TDRSS Tracking and Data Relay Satellite System. 57, 61

TDS Time-Domain Spectroscopy. i, 21, 41–49, 52

TPX polymethylpentene. 44, 45, 47, 48

TUM Technische Universität München. 1, 61, 65, 68, 69

UoW University of Wollongong, New South Wales, Australia. 41–44

VAC Vacuumschmelze GmbH & Co. KG, Hanau, Germany. 78

VNA Vector Network Analyser. 83

WiFi Wireless LAN. 2, 3

Bibliography

[YDN06] K. Yoshida, D. Dimitrov and H. Nakanishi. 'On the Capture of Tumbling Satellite by a Space Robot'. In: *IEEE/RSJ International Conference on Intelligent Robots and Systems*. 2006, pp. 4127–4132. DOI: 10.1109/IROS.2006.281900.

[Rek+07] I. Rekleitis, E. Martin, G. Rouleau, R. L'Archevêque, K. Parsa and E. Dupuis. 'Autonomous capture of a tumbling satellite'. In: *Journal of Field Robotics* 24.4 (2007), pp. 275–296. ISSN: 1556-4967. DOI: 10.1002/rob.20194. URL: http://dx.doi.org/10.1002/rob.20194.

[Lan+06] K. Landzettel, C. Preusche, A. Albu-Schaffer, D. Reintsema, B. Rebele and G. Hirzinger. 'Robotic On-Orbit Servicing - DLR's Experience and Perspective'. In: *IEEE/RSJ International Conference on Intelligent Robots and Systems*. 2006, pp. 4587–4594. DOI: 10.1109/IROS.2006.282164.

[Sto+09] E. Stoll, U. Walter, J. Artigas, C. Preusche, P. Kremer, G. Hirzinger, J. Letschnik and H. Pongrac. 'Ground verification of the feasibility of telepresent on-orbit servicing'. In: *Journal of Field Robotics* 26 (3 2009), pp. 287–307. ISSN: 1556-4967. DOI: 10.1002/rob.20286. URL: http://dx.doi.org/10.1002/rob.20286.

[Hir+05] G. Hirzinger, K. Landzettel, D. Reintsema, C. Preusche, A. Albu-Schäffer, B. Rebele and M. Turk. 'ROKVISS - Robotics Component Verification on ISS'. In: *Proc. of the 8th Int. Symposium on Artifical Intelligence, Robotics and Automation in Space (iSAIRAS)*. 2005.

[Rei+10] D. Reintsema, J. Thaeter, A. Rathke, W. Naumann, P. Rank and J. Sommer. 'DEOS – the German robotics approach to secure and de-orbit malfunctioned satellites from low earth orbits'. In: *Proceedings of the i-SAIRAS*. 2010, pp. 244–251. URL: http://robotics.estec.esa.int/i-SAIRAS/isairas2010/PAPERS/047-2827-p.pdf.

[Wei+13a] C. Weickhmann, N. Nathrath, R. Gehring, A. Gaebler, M. Jost and R. Jakoby. 'A Light-Weight Tunable Liquid Crystal Phase Shifter for an Efficient Phased Array Antenna'. In: *European Microwave Conference*. 2013.

[RD15] Y. Rahmat-Samii and A. C. Densmore. 'Technology Trends and Challenges of Antennas for Satellite Communication Systems'. In: *IEEE Transactions on Antennas and Propagation* 63.4 (2015), pp. 1191–1204. ISSN: 0018-926X. DOI: 10.1109/TAP.2014.2366784.

[Vat+99] F. Vatalaro, A. Ephremides, F. Gargione and F. Marconicchio. 'Guest Editorial Direct-to-user Satellite Systems And Technologies At Ka Band And Beyond'. In: *IEEE Journal on Selected Areas in Communications* 17.2 (1999), pp. 129–132. ISSN: 0733-8716. DOI: 10.1109/JSAC.1999.748776.

[Guo+07] N. Guo, R. C. Qiu, S. S. Mo and K. Takahashi. '60 GHz Millimeter-wave Radio: Principle, Technology, and New Results'. In: *EURASIP J. Wirel. Commun. Netw.* 1 (2007), pp. 48–48. ISSN: 1687-1472. DOI: 10.1155/2007/68253. URL: http://dx.doi.org/10.1155/2007/68253.

[VFC13] L. Verma, M. Fakharzadeh and S. Choi. 'Wifi on steroids: 802.11ac and 802.11ad'. In: *IEEE Wireless Communications* 20.6 (2013), pp. 30–35. ISSN: 1536-1284. DOI: 10.1109/MWC.2013.6704471.

[Rei88] F. Reinitzer. 'Beiträge zur Kenntniss des Cholesterins'. German. In: *Monatshefte für Chemie und verwandte Teile anderer Wissenschaften* 9.1 (1888), pp. 421–441. ISSN: 0343-7329. DOI: 10.1007/BF01516710.

[dP95] P.-G. de Gennes and J. Prost. *The Physics of Liquid Crystals*. 2nd. Oxford University Press, 1995.

[Mül+08] S. Müller, M. Köberle, F. Gölden, A. Penirschke, A. Gäbler, A. Lapanik, W. Haase and R. Jakoby. 'W-Band Characterization of Anisotropic Liquid Crystals at Room Temperature'. In: *European Microwave Conference*. 2008, pp. 119–122. DOI: 10.1109/EUMC.2008.4751402.

[Gäb15] A. Gäbler. 'Synthese steuerbarer Hochfrequenzschaltungen und Analyse Flüssigkristall-basierter Leitungsphasenschieber in Gruppenantennen für Satellitenanwendungen im Ka-Band'. German. PhD thesis. Fachbereich Elektrotechnik und Informationstechnik, Technische Universität Darmstadt, 2015.

[Mül06] S. Müller. 'Grundlegende Untersuchungen steuerbarer passiver Flüssigkristall-Komponenten für die Mikrowellentechnik'. German. PhD thesis. Fachbereich Elektrotechnik und Informationstechnik der TU Darmstadt, 2006.

[GM73] H. Gruler and G. Meier. 'Investigations on the Elastic Constants of the Nematic Homologous Series of 4,4'-Di(n-Alkoxy) Azoxybenzene'. In: *Molecular Crystals and Liquid Crystals* 23.3-4 (1973), pp. 261–270. DOI: 10.1080/15421407308083376. eprint: http://dx.doi.org/10.1080/15421407308083376. URL: http://dx.doi.org/10.1080/15421407308083376.

[Gru73] H. Gruler. 'Elastic Constants of Nematic Liquid Crystals'. In: *Z Naturforsch* 28a (1973), pp. 474–483. URL: http://www.znaturforsch.com/aa/v28a/c28a.htm.

[YW06] D.-K. Yang and S.-T. Wu. *Fundamentals of Liquid Crystal Devices*. Ed. by D.-K. Yang and S.-T. Wu. John Wiley & Sons, Ltd., 2006.

[Gäb+08a] A. Gäbler, F. Gölden, S. Müller and R. Jakoby. 'Triple-Mode Cavity Perturbation Method for the Characterization of Anisotropic Media'. In: *European Microwave Conference*. 2008, pp. 909–912. DOI: 10.1109/EUMC.2008.4751601.

[Kar+10] O. Karabey, F. Goelden, A. Gaebler and R. Jakoby. 'Precise broadband microwave material characterization of liquids'. In: *European Microwave Conference*. 2010, pp. 1591–1594.

[Gäb+10] A. Gäbler, F. Goelden, O. Karabey and R. Jakoby. 'A FDFD based eigen-dielectric formulation of the Maxwell equations for material characterization in arbitrary waveguide structures'. In: *IEEE MTT-S International Microwave Symposium Digest (MTT)*. 2010, pp. 1656–1659. DOI: 10.1109/MWSYM.2010.5514671.

[KK99] V. Kalesinskas and A. Konstantinov. 'An Approach to Permittivity Determination at Microwave Frequencies Through the Eigenvalue Problem'. In: *International Journal of Infrared and Millimeter Waves* 20.9 (1999), pp. 1709–1719. ISSN: 0195-9271. DOI: 10.1023/A:1021755108369.

[LMW12] A. Logg, K.-A. Mardal and G. Wells, eds. *Automated Solution of Differential Equations by the Finite Element Method – The FEniCS Book*. 1st ed. Lecture Notes in Computational Science and Engineering 84. Springer-Verlag Berlin Heidelberg, 2012. DOI: 10.1007/978-3-642-23099-8.

[Vie11] N. Vieweg. 'Eigenschaften und Anwendungen von Flüssigkristallen im Terahertz-Frequenzbereich'. German. PhD thesis. Göttingen: Zugl.: Braunschweig, Techn. Univ., Diss., 2011, 2011.

[VSK11] N. Vieweg, M. Shakfa and M. Koch. 'BL037: A nematic mixture with high terahertz birefringence'. In: *Optics Communications* 284.7 (2011), pp. 1887–1889. ISSN: 0030-4018. DOI: 10.1016/j.optcom.2010.12.061. URL: http://www.sciencedirect.com/science/article/pii/S0030401810014136.

[Vie+12] N. Vieweg, B. M. Fischer, M. Reuter, P. Kula, R. Dabrowski, M. A. Celik, G. Frenking, M. Koch and P. U. Jepsen. 'Ultrabroadband terahertz spectroscopy of a liquid crystal'. In: *Optics Express* 20.27 (2012), pp. 28249–28256. DOI: 10.1364/OE.20.028249. URL: http://www.opticsexpress.org/abstract.cfm?URI=oe-20-27-28249.

[Poz11] D. M. Pozar. *Microwave Engineering*. 4th edition. John Wiley & Sons, Inc. New York, 2011.

[Gäb+09a] A. Gäbler, F. Gölden, S. Müller, A. Penirschke and R. Jakoby. 'Direct simulation of material permittivities by using an eigen-susceptibility formulation of the vector variational approach'. In: *IEEE Instrumentation and Measurement Technology Conference (I2MTC)*. 2009, pp. 463–467. DOI: 10.1109/IMTC.2009.5168493.

[HRV05] V. Hernandez, J. E. Roman and V. Vidal. 'SLEPc: A Scalable and Flexible Toolkit for the Solution of Eigenvalue Problems'. In: *ACM Transactions on Mathematical Software* 31.3 (2005), pp. 351–362. ISSN: 0098-3500. DOI: 10.1145/1089014.1089019.

[Nel93] E. M. Nelson. 'High Accuracy Electromagnetic Field Solvers for Cylindrical Waveguides and Axisymmetric Structures Using the Finite Element Method'. PhD thesis. Stanford Linear Accelerator Center, Stanford University, 1993. URL: http://slac.stanford.edu/pubs/slacreports/reports07/slac-r-431.pdf.

[Col66] R. E. Collin. *Foundations for Microwave Engineering*. Physical and Quantum Electronic Series. McGraw-Hill, New York, 1966.

[Gao92] J. Gao. 'Analytical formulas for the resonant frequency changes due to opening apertures on cavity walls'. In: *Nuclear Instruments and Methods in Physics Research Section A: Accelerators, Spectrometers, Detectors and Associated Equipment* 311.3 (1992), pp. 437–443. ISSN: 0168-9002. DOI: http://dx.doi.org/10.1016/0168-9002(92)90638-K.

[Bet44] H. A. Bethe. 'Theory of Diffraction by Small Holes'. In: *Physical Review* 66 (7-8 1944), pp. 163–182. DOI: 10.1103/PhysRev.66.163.

[Sch15] S. Schmidt. 'Analysis of Higher Order Mode Cavity Perturbation Method for 60 GHz Characterization of Liquid Crystals'. Master's thesis. Technische Universität Darmstadt, Fachbereich Elektrotechnik und Informationstechnik, Institut für Mikrowellentechnik und Photonik, 2015.

[Pan+03] R.-P. Pan, T.-R. Tsai, C.-Y. Chen and C.-L. Pan. 'Optical Constants of Two Typical Liquid Crystals 5CB and PCH5 in the THz Frequency Range'. In: *Journal of Biological Physics* 29.2 (2003), pp. 335–338. ISSN: 1573-0689. DOI: 10.1023/A:1024485918938.

[Eni+07] V. A. Enikeeva, V. A. Makarov, I. A. Ozheredov and A. P. Shkurinov. 'Terahertz time-domain spectroscopy of liquid crystal materials'. In: *Joint International Conference on Infrared and Millimeter Waves and International Conference on Terahertz Electronics*. 2007, pp. 480–481. DOI: 10.1109/ICIMW.2007.4516591.

[Wil+09] R. Wilk, N. Vieweg, O. Kopschinski, T. Hasek and M. Koch. 'THz Spectroscopy of Liquid Crystals from the CB Family'. In: *Journal of Infrared, Millimeter, and Terahertz Waves* 30.11 (2009), pp. 1139–1147. ISSN: 1572-9559. DOI: 10.1007/s10762-009-9537-z.

[ACS84] D. H. Auston, K. P. Cheung and P. R. Smith. 'Picosecond photoconducting Hertzian dipoles'. In: *Applied Physics Letters* 45.3 (1984), pp. 284–286. DOI: 10.1063/1.95174.

[ZOm] ZOmega Terahertz Corp. *Z-3 (TM) Terahertz Time Domain Spectrometer*. URL: http://dl.z-thz.com/brochures/Z3.pdf.

[Vie+14] N. Vieweg, F. Rettich, A. Deninger, H. Roehle, R. Dietz, T. Göbel and M. Schell. 'Terahertz-time domain spectrometer with 90 dB peak dynamic range'. In: *J Infrared Milli Terahz Waves* 35.10 (2014), pp. 823–832. ISSN: 1866-6906. DOI: 10.1007/s10762-014-0085-9.

[CGG69] J. Chamberlain, J. Gibbs and H. Gebbie. 'The determination of refractive index spectra by fourier spectrometry'. In: *Infrared Physics* 9.4 (1969), pp. 185–209. ISSN: 0020-0891. DOI: 10.1016/0020-0891(69)90023-2. URL: http://www.sciencedirect.com/science/article/pii/0020089169900232.

[DGC96] L. Duvillaret, F. Garet and J.-L. Coutaz. 'A reliable method for extraction of material parameters in terahertz time-domain spectroscopy'. In: *IEEE Journal of Selected Topics in Quantum Electronics* 2.3 (1996), pp. 739–746. ISSN: 1077-260X. DOI: 10.1109/2944.571775.

[BDL81] J. Birch, J. Dromey and J. Lesurf. 'The optical constants of some common low-loss polymers between 4 and 40 cm⁻1'. In: *Infrared Physics* 21.4 (1981), pp. 225–228. ISSN: 0020-0891. DOI: 10.1016/0020-0891(81)90053-1. URL: http://www.sciencedirect.com/science/article/pii/0020089181900531.

[Tyd] Tydex J.S.Co. *THz Materials*. URL: http://www.tydexoptics.com/pdf/THz_Materials.pdf.

[Wei+13b] C. Weickhmann, R. Jakoby, E. Constable and R. Lewis. 'Time-domain spectroscopy of novel nematic liquid crystals in the terahertz range'. In: *International Conference on Infrared, Millimeter, and Terahertz Waves (IRMMW-THz)*. 2013. DOI: 10.1109/IRMMW-THz.2013.6665423.

[Wil+15] M. Wilde, J. T. Harder, J. Ventura, J. Hörmann and U. Walter. 'Impact of Space-to-Ground Video Transmission Constraints on Teleoperated Final Approach and Docking'. In: *Journal of Aerospace Information Systems* 12 (7 2015). DOI: 10.2514/1.I010288. URL: http://dx.doi.org/10.2514/1.I010288.

[Har+09] J. Harder, E. Stoll, M. Schiffner, M. Pfeiffer and U. Walter. 'A compact, light-weight high data-rate antenna system for remote-sensing orbiters and space exploration'. In: *Acta Astronautica* 65 (11–12 2009), pp. 1738–1744. ISSN: 0094-5765. DOI: http://dx.doi.org/10.1016/j.actaastro.2009.05.001. URL: http://www.sciencedirect.com/science/article/pii/S0094576509002823.

[Lun+07] R. Lundin, N. Nathrath, D. Fasold, M. Trumper, J. Letschnik and U. Walter. 'A Compact and Lightweight Inter-Satellite Antenna for S-Band'. In: *European Conference on Antennas and Propagation (EuCAP)*. 2007. DOI: 10.1049/ic.2007.0903.

[Ros+12] B. Rosich, N. Miranda, P. Potin, C. Putignano, G. Sabella and D. Geudtner. 'Sentinel-1 Ground Segment'. In: *IEEE International Geoscience and Remote Sensing Symposium*. 2012, pp. 1726–1729. DOI: 10.1109/IGARSS.2012.6351189.

[Pot+12] P. Potin, P. Bargellini, H. Laur, B. Rosich and S. Schmuck. 'Sentinel-1 mission operations concept'. In: *IEEE International Geoscience and Remote Sensing Symposium*. 2012, pp. 1745–1748. DOI: 10.1109/IGARSS.2012.6351183.

[NAS01] NASA. *NASA Facts – Three Newly DesignedTracking and Data Relay Satellites To Help Replenish Existing On-Orbit Fleet*. Goddard Space Flight Center. 2001. URL: http://www.nasa-usa.de/sites/default/files/97440main_TDRS_fs_9.18.pdf (visited on 2015).

[ESA12] ESA. *ARTEMIS Announcement of Opportunity*. 2012. URL: http://telecom.esa.int/telecom/media/document/ARTEMIS%20A0%20-%20Issue%201.0.pdf.

[SFO11] M. Schallner, B. Friedrichs and F. Ortwein. 'Verification of new technologies as main task of the communication payload of the Heinrich-Hertz mission'. In: *CEAS Space Journal* 2.1 (2011), pp. 67–73. ISSN: 1868-2510. DOI: 10.1007/s12567-011-0010-1. URL: http://dx.doi.org/10.1007/s12567-011-0010-1.

[Voi10] S. Voigt. 'The German Heinrich Hertz Satellite Mission'. In: *European Conference on Antennas and Propagation (EuCAP)*. 2010, pp. 1–4. URL: http://ieeexplore.ieee.org/xpl/login.jsp?tp=&arnumber=5505537.

[DW12] H. Dodel and R. Wörfel. *Satellitenfrequenzkoordinierung*. German. Springer-Verlag Berlin Heidelberg, 2012. 429 pp. DOI: 10.1007/978-3-642-29203-3. URL: http://www.springer.com/de/book/9783642292026.

[HHH13] A. Hoehn, P. Hager and J. Harder. 'Design characterization of an electronic steerable Ka-band antenna using liquid crystal phase shifters'. In: *IEEE Aerospace Conference*. 2013, pp. 1–14. DOI: 10.1109/AERO.2013.6496965.

[Hoe+15] A. Hoehn, M. Tebbe, U. Walter, S. Endler, H. Baier, J. Letschnik, C. Weickhmann, R. Jakoby, N. Nathrath, M. Trümper, R. Gehring, H. Wolf, D. Fasold, G. Strauss and M. Wleklinski. 'LISA Strahlschwenk-Technologien im Ka-Band'. In: *4. Nationale Konferenz Satellitenkommunikation in Deutschland*. 2015.

[NIS10] NIST. *CODATA Internationally Recommended 2010 values of the Fundamental Physical Constants*. Tech. rep. National Institute of Standards and Technology, 2010. URL: http://physics.nist.gov/cuu/Constants/index.html.

[NASa] NASA. *NASA Solar System Exploration Homepage*. Tech. rep. NASA. URL: http://solarsystem.nasa.gov.

[PHW09] M. Pfeiffer, J. Harder and U. Walter. 'Development of a compact Ka-band antenna poipoint mechanism for intersatellite links on small satellites'. In: *European Space Mechanisms and Tribology Symposium*. 13th European Space Mechanisms and Tribology Symposium – ESMATS 2009. Vienna, Austria, 2009. URL: http://www.esmats.eu/esmatspapers/pastpapers/pdfs/2009/pfeiffer.pdf.

[Wei+13c] C. Weickhmann, N. Nathrath, R. Gehring, A. Gaebler, M. Jost and R. Jakoby. 'Recent measurements of compact electronically tunable liquid crystal phase shifter in rectangular waveguide topology'. In: *Electronics Letters* 49 (21 2013), pp. 1345–1347. ISSN: 0013-5194. DOI: 10.1049/el.2013.2281.

[Goe+06] F. Goelden, S. Mueller, P. Scheele, M. Wittek and R. Jakoby. 'IP3 Measurements of Liquid Crystals at Microwave Frequencies'. In: *European Microwave Conference*. 2006, pp. 971–974. DOI: 10.1109/EUMC.2006.281084.

[Göl09] F. Gölden. 'Flüssigkristall-basierte Mikrowellenkomponenten mit schnellen Schaltzeiten: Material, Technologie, Leistungsverträglichkeit Liquid Crystal Based Microwave Components with Fast Response Times: Material, Technology, Power Handling Capability'. German. PhD thesis. Fachbrereich Elektrotechnik und Informationstechnik, Technische Universität Darmstadt, 2009.

[Gäb+09b] A. Gäbler, F. Gölden, A. Manabe, M. Göbel, S. Müller and R. Jakoby. 'Investigation of high performance transmission line phase shifters based on liquid crystal'. In: *European Microwave Conference*. 2009, pp. 594–597.

[San13] San Diego Plastics Inc. *Rexolite Datasheet*. as of 2013-02-13. 2013. URL: http://www.sdplastics.com/rexolite.html.

[FB97] G. Friedsam and E. Biebl. 'A broadband free-space dielectric properties measurement system at millimeter wavelengths'. In: *IEEE Transactions on Instrumentation and Measurement* 46.2 (1997), pp. 515–518. ISSN: 0018-9456. DOI: 10.1109/19.571899.

[ESA15] ESA. *European Preferred Parts List*. English. Tech. rep. European Space Components Information Exchange System, 2015. URL: https://escies.org/.

[NASb] NASA. *NASA Parts Selection List (NPSL)*. English. Tech. rep. Goddard Space Flight Center, NEPP. URL: http://nepp.nasa.gov/npsl/.

[Hu11] W. Hu. 'Analysis and design of tunable phase shifters for satellite antenna array under considerations of time domain constrains'. MA thesis. Technische Universität Darmstadt, Fachbereich Elektrotechnik und Informationstechnik, Institut für Mikrowellentechnik und Photonik, 2011.

[Teb+16] M. Tebbe, A. Hoehn, N. Nathrath and C. Weickhmann. 'Simulation of an Electronically Steerable Horn Antenna Array with Liquid Crystal Phase Shifters'. In: *IEEE Aerospace Conference*. 2016. DOI: 10.1109/AERO.2016.7500660.

[DuP09] DuPont. *DuPont(TM) Pyralux(R) AP All-Polyimide Flexible Laminate*. EN. DuPont. 2009. URL: http://www2.dupont.com/Pyralux/en_US/assets/downloads/pdf/APclad_H-73241.pdf.

[Wei13] C. Weickhmann. 'inside view'. In: *Electronics Letters* 49 (21 2013), pp. 1307–1308. ISSN: 0013-5194. DOI: 10.1049/el.2013.3211.

[Nic+17] M. Nickel, O. Karabey, M. Maasch, R. Reese, M. Jost, C. Damm, R. Jakoby and H. Maune. 'Analysis of Hybrid-Passive-Active Phased Array Configurations Based on an SNR Approximation'. In: *European Conference on Antennas and Propagation (EuCAP)*. submitted. 2017.

[Ric15] M. Rickes. 'Design and Fabrication of a LC Hollow Waveguide Phase Shifter for 250 GHz'. Master's Thesis. Technische Universität Darmstadt, Fachbereich Elektrotechnik und Informationstechnik, Institut für Mikrowellentechnik und Photonik, 2015.

[Mar16] M. Marscholl. 'Entwurf und Umsetzung einer elektronischen Ansteuerung für flüssigkristallbasierte Hohlleiter-Phasenschieber bei 250 GHz'. German. 2250-B. Bachelor's Thesis. Technische Universität Darmstadt, Fachbereich Elektrotechnik und Informationstechnik, Institut für Mikrowellentechnik und Photonik, 2016.

[Jin10] J.-M. Jin. 'The Finite Element Method'. In: *Theory and Computation of Electromagnetic Fields*. John Wiley & Sons, Inc., 2010, pp. 342–398. ISBN: 9780470874257. DOI: 10.1002/9780470874257.ch9.

[CL11] P. Ciarlet and S. Labrunie. 'Numerical solution of Maxwell's equations in axisymmetric domains with the Fourier Singular Complement Method'. In: *The Journal of Difference Equations and Applications* 3 (2011). 37 pages, pp. 113–155. URL: https://hal.archives-ouvertes.fr/hal-00365391.

[Ott+12] A. Otto, N. Marais, E. Lezar and D. Davidson. 'Using the FEniCS Package for FEM Solutions in Electromagnetics'. In: *IEEE Antennas and Propagation Magazine* 54.4 (2012), pp. 206–223. ISSN: 1045-9243. DOI: 10.1109/MAP.2012.6309184.

[Sch03] A. Schneebeli. *An $H(curl;\Omega)$-conforming FEM: Nédélec's elements of first type*. Tech. rep. unknown, 2003.

[Gäb+08b] A. Gäbler, F. Gölden, S. Müller and R. Jakoby. 'Modeling of electrically tunable transmission line phase shifter based on liquid crystal'. In: *IEEE Antennas and Propagation Society International Symposium (APS)*. 2008, pp. 1–4. DOI: 10.1109/APS.2008.4619963.

Own Publications

First Author

[Wei+13a] C. Weickhmann, N. Nathrath, R. Gehring, A. Gaebler, M. Jost and R. Jakoby. 'A Light-Weight Tunable Liquid Crystal Phase Shifter for an Efficient Phased Array Antenna'. In: *European Microwave Conference*. 2013.

[Wei+13b] C. Weickhmann, R. Jakoby, E. Constable and R. Lewis. 'Time-domain spectroscopy of novel nematic liquid crystals in the terahertz range'. In: *International Conference on Infrared, Millimeter, and Terahertz Waves (IRMMW-THz)*. 2013. DOI: 10.1109/IRMMW-THz.2013.6665423.

[Wei+13c] C. Weickhmann, N. Nathrath, R. Gehring, A. Gaebler, M. Jost and R. Jakoby. 'Recent measurements of compact electronically tunable liquid crystal phase shifter in rectangular waveguide topology'. In: *Electronics Letters* 49 (21 2013), pp. 1345–1347. ISSN: 0013-5194. DOI: 10.1049/el.2013.2281.

[Wei+14] C. Weickhmann, M. Jost, D. Laemmle and R. Jakoby. 'Design and fabrication considerations for a 250 GHz liquid crystal phase shifter'. In: *International Conference on Infrared, Millimeter, and Terahertz waves (IRMMW-THz)*. (2014). 2014. DOI: 10.1109/IRMMW-THz.2014.6956330.

[Wei+15] C. Weickhmann, S. Schmidt, M. Jost, W. Hu, R. Jakoby, A. Manabe, C. Fritzsch and M. Wittek. 'Measuring Liquid Crystal Permittivity With High Accuracy'. In: *Annual Condensed Matter and Materials Meeting*. (2015). Wagga Wagga, NSW, Australia, 2015. URL: http://www.aip.org.au/info/sites/default/files/cmm/2015/Wagga2015_8_FM5_Weickhmann.pdf.

[WJ16] C. Weickhmann and R. Jakoby. 'Material Characterisation using an Eigen-Permittivity Formulation in FEniCS'. In: *The FEniCS 2016 Workshop*. The FEniCS 2016 Workshop. (Simula Research Centre). Oslo, 2016.

Co-Authorship

[Jos+13] M. Jost, C. Weickhmann, S. Strunck, A. Gaebler, C. Fritzsch, O. Karabey and R. Jakoby. 'Liquid crystal based low-loss phase shifter for W-band frequencies'. In: *Electronics Letters* 49 (23 2013), pp. 1460–1462. ISSN: 0013-5194. DOI: 10.1049/el.2013.2830.

[Sob+13] N. Sobornytskyy, A. Lisauskas, C. Weickhmann, R. Jakoby, A. Semenov, H. Hubers, R. Muller, A. Hoehl and O. Cojocari. 'Quasi optical Schottky diode detectors for fast ultra-wideband detection'. In: *International Conference on Infrared, Millimeter, and Terahertz Waves (IRMMW-THz). (2013)*. 2013. DOI: 10.1109/IRMMW-THz.2013.6665618.

[Str+13] S. Strunck, O. H. Karabey, C. Weickhmann, A. Gaebler and R. Jakoby. 'Continuously tunable phase shifters for phased arrays based on liquid crystal technology'. In: *IEEE International Symposium on Phased Array Systems Technology*. 2013, pp. 82–88. DOI: 10.1109/ARRAY.2013.6731805.

[Jos+14a] M. Jost, A. Gaebler, C. Weickhmann, S. Strunck, W. Hu, O. H. Karabey and R. Jakoby. 'Evolution of microwave nematic liquid crystal mixtures and development of continuously tunable micro- and millimetre wave components'. In: *International Liquid Crystal Conference. (2014)*. 2014.

[Jos+14b] M. Jost, C. Weickhmann, S. Strunck, A. Gaebler, W. Hu, T. Franke, A. E. Prasetiadi, O. H. Karabey and R. Jakoby. 'Electrically biased W-band phase shifter based in liquid crystal'. In: *International Conference on Infrared, Millimeter, and Terahertz waves (IRMMW-THz). (2014)*. 2014.

[Jos+15a] M. Jost, S. Strunck, A. Heunisch, A. Wiens, A. Prasetiadi, C. Weickhmann, B. Schulz, M. Quibeldey, O. Karabey, T. Rabe, R. Follmann, D. Koether and R. Jakoby. 'Continuously tuneable liquid crystal based stripline phase shifter realised in LTCC technology'. In: *European Microwave Conference. (2015)*. 2015. DOI: 10.1109/EuMC.2015.7345999.

[Pra+15] A. Prasetiadi, O. Karabey, C. Weickhmann, T. Franke, W. Hu, M. Jost, M. Nickel and R. Jakoby. 'Continuously tunable substrate integrated waveguide bandpass filter in liquid crystal technology with magnetic biasing'. In: *Electronics Letters* 51.20 (2015), pp. 1584–1585. ISSN: 0013-5194. DOI: 10.1049/el.2015.2494.

[Jos+15b] M. Jost, C. Weickhmann, T. Franke, A. Prasetiadi, W. Hu, M. Nickel, O. Karabey and R. Jakoby. 'Tuneable hollow waveguide devices for space applications based on liquid crystal'. In: *SBMO/IEEE MTT-S International Microwave and Optoelectronics Conference (IMOC). (2015)*. 2015. DOI: 10.1109/IMOC.2015.7369046.

[Läm+16] D. Lämmle, H. F. Schlaak, C. Weickhmann and R. Jakoby. 'Proof of Concept for a WR-2.2 MEMS Waveguide Switch'. In: *International Conference on Infrared, Millimeter, and Terahertz Waves (IRMMW-THz)*. 2016.

[Teb+16] M. Tebbe, A. Hoehn, N. Nathrath and C. Weickhmann. 'Simulation of an Electronically Steerable Horn Antenna Array with Liquid Crystal Phase Shifters'. In: *IEEE Aerospace Conference*. 2016. DOI: 10.1109/AERO.2016.7500660.

[Mau+17] H. Maune, C. Weickhmann, M. Jost, R. Reese, M. Nickel, C. Fritzsch and R. Jakoby. 'Liquid Crystal Technology for Reconfigurable SatCom Applications'. In: *Proceedings of the Radio and Wireless Week*. 2017.

Contributions to Books

[Dam+15] C. Damm, H. G. L. Schwefel, F. Sedlmeir, H. Hartnagel, S. Preu and C. Weickhmann. 'Selected Emerging THz Technologies'. In: *Semiconductor Terahertz Technology*. John Wiley & Sons, Ltd, 2015. Chap. 8, pp. 340–382. ISBN: 9781118920411. DOI: 10.1002/9781118920411.ch8.

Other Publications

[Wei13] C. Weickhmann. 'inside view'. In: *Electronics Letters* 49 (21 2013), pp. 1307–1308. ISSN: 0013-5194. DOI: 10.1049/el.2013.3211.

Supervised Theses

Ilieva, Milena Marinova Master's Thesis D2208-M, Darmstadt 2014
German Title: *Direkte Phasenmessung eines Ka-Band LC-Phasenschiebers zur Bestimmung einer Regelgröße*
English Title: *Real Time Relative Phase Measurement for Passive Variable Delay*

Rickes, Martin Master's Thesis D2223-M, Darmstadt 2015
Design and Fabrication of a LC Hollow Waveguide Phase Shifter for 250 GHz

Schmidt, Sönke Master's Thesis D2234-M, Darmstadt 2015
Analysis of Higher Order Mode Cavity Perturbation Method for 60 GHz Characterisation of Liquid Crystals

Marscholl, Mathias Bachelor's Thesis 2250-B, Darmstadt 2016
German Title: *Entwurf und Umsetzung einer elektronischen Ansteuerung für flüssigkristallbasierte Hohlleiter-Phasenschieber bei 250 GHz*
English Title: *Design and Implementation of an Electronic Biasing Scheme for Liquid Crystal Based Phase-Shifter at 250 GHz*

Siddiqui, Muhammad Usman Master's Thesis (Hochschule Darmstadt), 2016
Analysis of Dynamic Properties of Steerable Liquid Crystal Antenna Arrays

Curriculum Vitae

Personal Details

Name	Christian Joachim Michael Weickhmann
Date of Birth	14 January 1985
Place of Birth	Bad Homburg v. d. H., Germany

Education

1991-1995	Grundschule Ober-Rosbach, Germany
1995-2004	Augustinerschule Friedberg, Gymnasium, Germany
2004-2010	Electrical Engineering and Information Technology at Technische Universität Darmstadt, Germany
2008-2010	Double Degree Diplôme d'Ingénieur Physique-Nanosciences at Grenoble INP, École de Physique, Électronique et Matériaux (PHELMA), Grenoble, France

Professional Career

2010-2016	Research Assistant, Institute of Microwave Engineering and Photonics, Technische Universität Darmstadt, Germany
2015-2016	Project Manager LOEWE Programme "Sensors Towards Terahertz", Institute of Microwave Engineering and Photonics, Technische Universität Darmstadt, Germany

Birmingham, 27 October 2016